ABSTRACT

Title of Document: EXPERIMENTAL INVESTIGATION OF THE MECHANICAL PROPERTIES AND AUXETIC BEHAVIOR OF IRON-GALLIUM ALLOYS

Holly Marie Schurter
Master of Science, 2009

Directed By: Professor Alison Flatau
Department of Aerospace Engineering

Iron-gallium alloys (known as Galfenol) are a unique material that have shown great potential for numerous applications. They exhibit a strong magneto-mechanical coupling, otherwise known as magnetostriction, which lends itself very well to transducer applications, from the nano-scale to macro scale. In addition, Galfenol is one of only a few metal alloys known to exhibit large auxetic or negative Poisson's ratio behavior. In order to develop any Galfenol-based applications, it will be necessary to understand its mechanical behavior. The goal of the research presented in this thesis therefore is to measure the elastic properties of Galfenol for a range of compositions in order to create a database, as well as present trends in the elastic properties. This is achieved through tensile testing of single-crystal Galfenol dogbone-shaped specimens and through Resonant Ultrasound Spectroscopy (RUS) of small parallelepiped samples.

EXPERIMENTAL INVESTIGATION OF THE MECHANICAL PROPERTIES AND AUXETIC BEHAVIOR OF IRON-GALLIUM ALLOYS

By

Holly Marie Schurter

Thesis submitted to the Faculty of the Graduate School of the
University of Maryland, College Park, in partial fulfillment
of the requirements for the degree of
Master of Science
2009

Advisory Committee:
Professor Alison Flatau, Chair
Professor Norman Wereley
Professor Abhijit Dasgupta

Dedication

To my family.

Acknowledgements

First, I would like to express my gratitude to my advisor Dr. Alison Flatau for her guidance and support of my research. I am particularly grateful for her unwavering dedication and confidence in this project.

I wish to acknowledge the financial support of NSF grant 0706503 and ONR MURI Grant No. N000140610530.

I would also like to thank my mentor at NSWC Carderock, Dr. Gabriela Petculescu, for her patience and guidance, and for providing the RUS equipment used in this study. I also wish to thank Ms. Marilyn Wun-Fogle, Dr. James Restorff and Dr. Arthur Clark from NSWC for their support and for sharing their wide areas of expertise with me. I wish to acknowledge the ASEE/ONR NREIP program for supporting my research at NSWC.

At the University of Maryland, I would like to acknowledge the support of Dr. Jin-Hyeong Yoo for the initial design of the tensile testing equipment and procedure. I would also like to acknowledge Dr. Phil Piccoli for the composition analysis of the samples, and Dr. Suok-Min Na for the heat treatment of some of the samples. I also wish to thank Supratik Datta and the rest of the graduate students in the magnetostrictive materials group for all their assistance with this research.

I also wish to acknowledge the support of Dr. Tom Lograsso and the USDOE Materials Preparation Center at Ames Laboratory for preparing the samples used in this study.

Finally, I wish to thank all of my professors, my classmates, and the staff of the aerospace engineering department for making my graduate and undergraduate experience so positive.

Table of Contents

List of Tables

List of Figures

Chapter 1: Introduction

The goal of the research presented in this thesis is to characterize the mechanical behavior of iron-gallium alloys (known as Galfenol) with an emphasis on understanding the negative Poisson's ratio behavior of these alloys. Experimental results obtained for a comprehensive set of alloys through various testing methods, primarily tensile testing and resonant ultrasound spectroscopy are presented and discussed. In addition, comparisons between the testing methods, and between the experimental data and a theoretical model are presented.

1.1 Motivation

Iron-gallium alloys, $Fe_{100-x}Ga_x$, $0<x\leq 35$, are a unique material that have shown great potential for numerous applications. Much of the interest in this alloy has been centered on its strong magneto-mechanical coupling, otherwise known as magnetostriction. Consequentially, significant research has been done in understanding and quantifying the magnetostriction of this alloy (see for example [1,2]). This capability lends itself very well to transducer applications, from the nano-scale to macro scale. Development of any application, however, will require knowledge of the engineering elastic properties. Although some research [3] has begun to examine the elastic properties, it was only for a few compositions and was not specifically intended to aid engineers. One of the goals of this research, therefore, was to generate a more comprehensive database of the elastic properties of Galfenol

for the full range of compositions, with the intent of using the database for engineering applications.

In addition to exhibiting magnetostriction, Galfenol also possesses the unusual attribute of demonstrating in-plane auxetic behavior. This is a term for materials that possess a negative Poisson's ratio. Although auxetic behavior is observed in other materials, Galfenol exhibits a unique combination of high auxeticity and high strength. This makes Galfenol an ideal candidate for a variety of novel applications for which no other materials are suitable. Consequently, an additional focus of this research has been on understanding and quantifying the auxetic behavior of Galfenol.

1.2 Crystallography

Galfenol's auxetic behavior and the magnetostriction are both maximized in single crystal samples. In single crystal Galfenol, the mechanical and magnetic properties change with respect to the crystal lattice. Therefore, a brief overview of crystal structure and the Miller indices nomenclature will aid in discussion of the properties examined in this work.

A single crystal material is a material in which the periodic and repeated atomic pattern extends throughout its entirety without interruption [4]. The Galfenol samples studied here all possess a body centered cubic (BCC) crystal lattice, shown schematically in Figure 1.1. The lattice is assumed to be comprised of iron atoms with randomly distributed gallium atoms taking the place of iron atoms.

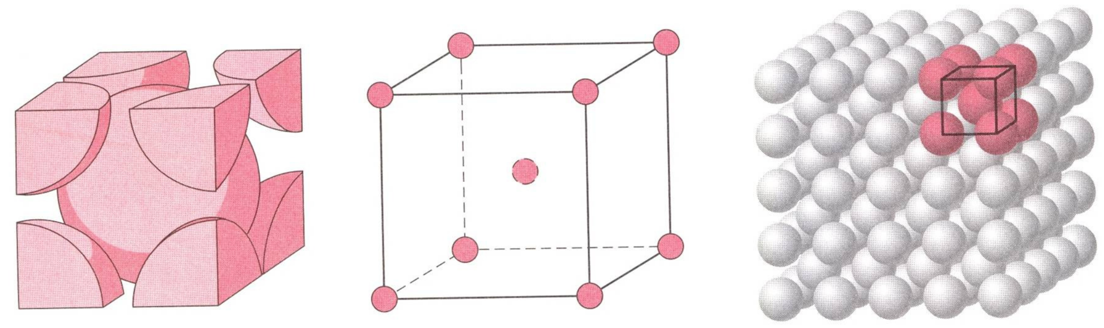

(a.) (b.) (c.)

Figure 1.1: Body centered cubic lattice: (a.) hard sphere unit cell representation, (b.) reduced-sphere unit cell, (c.) aggregate of many atoms. [4]

Grouped Miller indices are traditionally used to describe the vector for a particular direction [u v w] or a plane (u v w) of a lattice. Figure 1.2 shows a BCC cell with the [100], [010], [001] and [110] directions marked, as well as the (001) plane. In this cell, the back left atom on the bottom surface is taken as the origin.

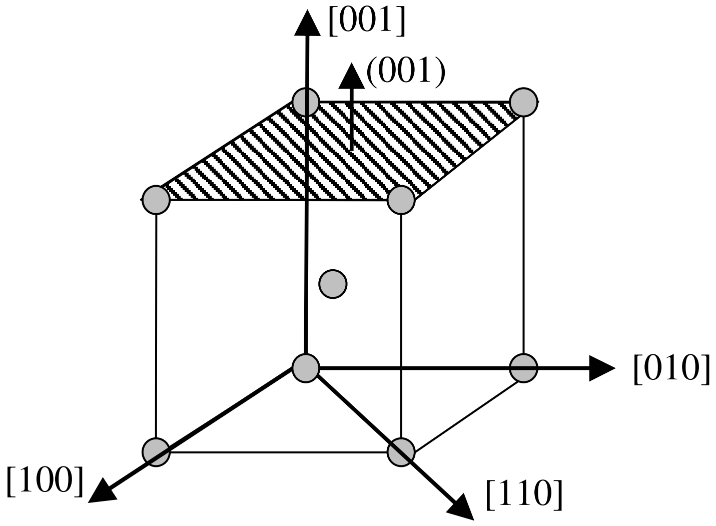

Figure 1.2: BCC cell with Miller index notation for the [100], [010], [001] and [110] directions and the (001) plane.

The maximum magnetostriction is observed along the [100] direction when a magnetic field is applied along that same direction. A negative Poisson's ratio is observed in the (001) planes along the $[1\bar{1}0]$ direction when a tensile load is applied along the [110] direction. A simultaneous large contraction occurs along the [001] direction, thus volume is approximately conserved. Consequently, these are the directions and planes focused on in this research. The corresponding Poisson's ratios are written as $\nu_{(100,\ 010)}$ and $\nu_{(110,\ 1\bar{1}0)}$, where the first subscript represents the load direction and the second identifies the direction transverse to the load. Generally, the first subscript will be left off in the remainder of this thesis.

1.3 Negative Poisson's Ratio

1.3.1 Origins and causes of auxetic behavior

Galfenol is one of only a few known materials to possess a very low negative Poisson's ratio, with measured values of as low as -0.7 [2]. Auxetic behavior is present in single crystal specimens of a large variety of metals, such as nickel, copper and gold, however, it is much smaller in these materials, typically on the order of -0.1 [5]. Theoretical research has suggested that it may be possible to achieve a Poisson's ratio of less than -1 in a hypothetical cubic material [6]. Table 1.1 shows a list of some of the various materials that exhibit a negative Poisson's ratio.

Table 1.1: Some sample auxetic materials [5,6].

Material	**Crystal structure**	$\nu_{[1\,\bar{1}0]}$
Lithium	bcc	-0.5498
Iron	bcc	-0.0587
Nickel	fcc	-0.0676
Copper	fcc	-0.1358
Galfenol	fcc	≥ -0.75
Hypothetical cubic material		≤ -1

An atomic basis for the phenomenon of auxetic behavior is shown in Figure 1.3. When atoms 2 and 4 are pulled apart, atoms 1 and 3 move closer to the center, thus pushing atoms 5 and 6 outwards.

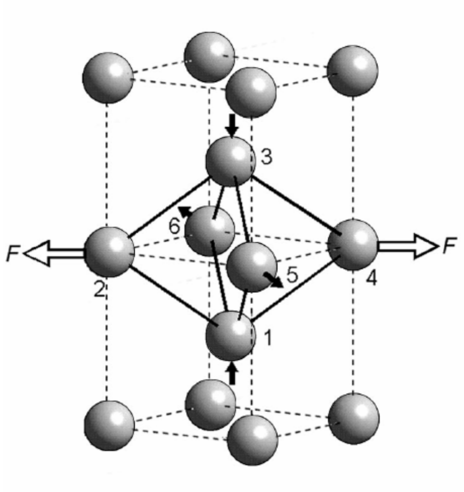

Figure 1.3: Atomic basis for auxetic behavior [7].

More significant auxetic behavior can be achieved using geometry changes in manmade materials, such as foams and honeycomb structures, but these materials are usually not high strength. These materials have been around since the 1950s and have shown potential for a variety of applications, ranging from mattress cushions to use in nuclear reactor cores [8]. Figure 1.4a shows a schematic of an auxetic honeycomb structure, and Figure 1.4b shows an auxetic keyed-brick structure.

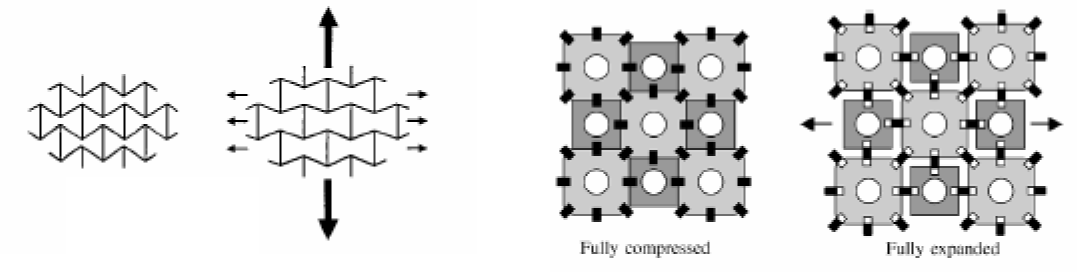

Figure 1.4(a): Auxetic honeycomb structure [8], **(b):** Auxetic keyed-brick structure [8].

1.3.2 Applications for Galfenol's auxetic behavior

The combination of large negative Poisson's ratio, high strength (~530 MPa yield strength [9]) and magneto-mechanical coupling make Galfenol a very promising material for novel devices. There are a number of applications that could utilize the auxetic behavior and high strength. One example would be a press-fit fastening device. Figure 1.5 shows an exaggerated schematic of how this might work. If an auxetic fastener is compressed, its width will get narrower, allowing insertion into a holder. When the compressive load is removed, the fastener will widen and thus be stuck in place. Any applied tensile load would cause the fastener to widen even more, making it nearly impossible to remove.

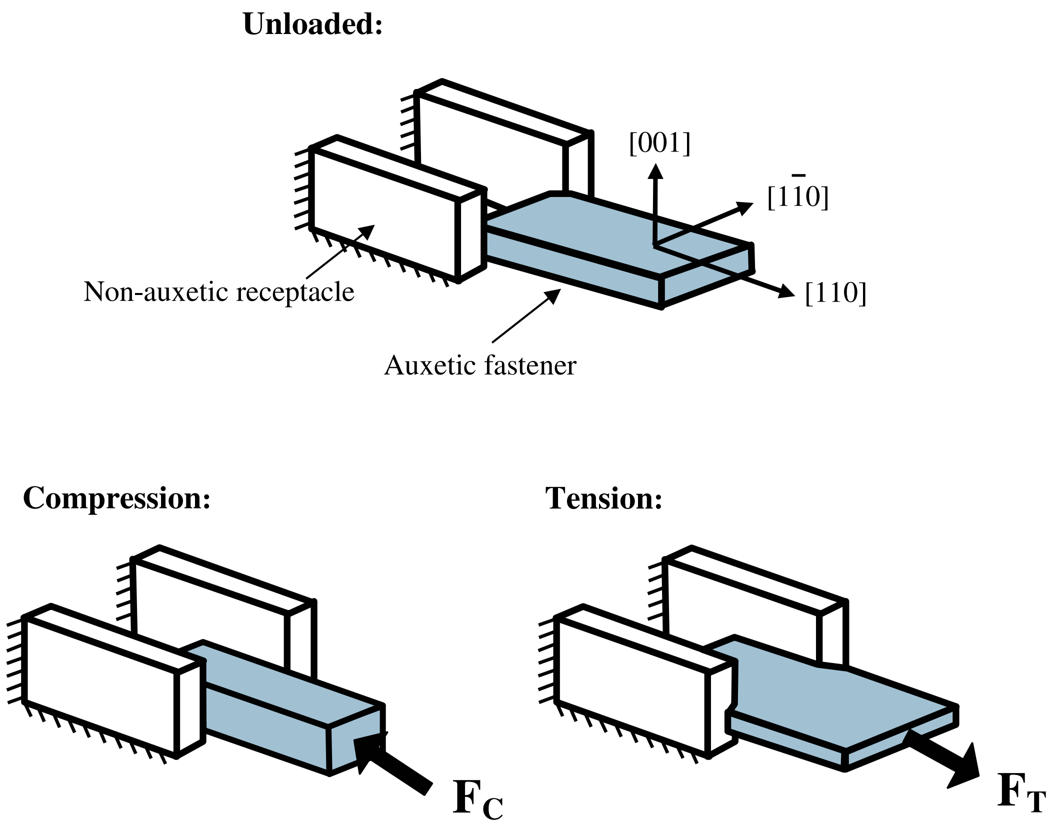

Figure 1.5: Press-fit fastening device utilizing auxetic behavior [9].

Another application would be something that made use of the high indentation resistance of an auxetic metal alloy like Galfenol. A material with a highly negative Poisson’s ratio will have better indentation resistance than a typical metal alloy, because of the increased hardness along the [110] direction. This is illustrated in Figure 1.6.

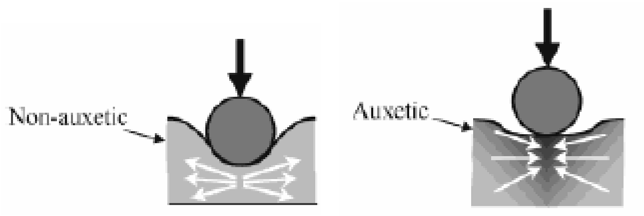

Figure 1.6: Indentation resistance of a non-auxetic and auxetic material [8].

1.4 Magnetostriction

Since one goal of this study is to aid researchers studying the magnetostrictive capabilities of Galfenol, a brief introduction to that phenomenon will be presented. Magnetic materials generally exhibit a coupling between the magnetization and the strain in them. Hence, the dimension of these materials can be changed by applying a magnetic field. Conversely, the magnetization of a sample can be altered by applying a stress. This behavior is known as magnetostriction. Galfenol has been shown to exhibit moderate magnetostriction, ~200 to 400 $\mu\varepsilon$, under low magnetic fields, ~200 to 400 Oe [1]. This combined with its low hysteresis and desirable mechanical properties (i.e. ductility, high yield strength) make it an ideal candidate for transducer applications [9].

Under no applied magnetic field and no applied stress, a magnetostrictive material is comprised of randomly oriented magnetic moments. If a magnetic field is applied along the longitudinal axis of a magnetostrictive rod, the moments will rotate such that their longitudinal axes are aligned with the magnetic field. If a compressive stress is applied along the longitudinal axis of the rod, the moments will orient themselves so they are perpendicular to the applied stress. The strain resulting from the total length change as the moments rotate from all perpendicular to all parallel is defined as the saturation magnetostriction. This is the phenomenon responsible for Galfenol's actuation behavior, and it is shown schematically in Figure 1.7.

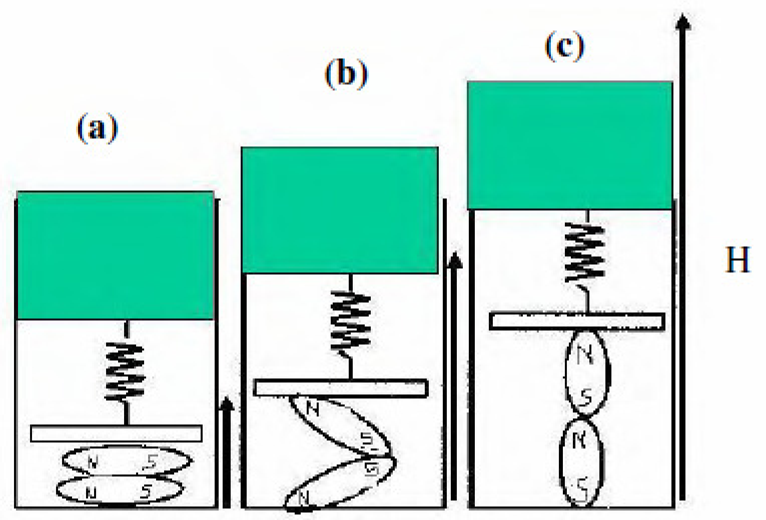

Figure 1.7: Schematic of Galfenol's actuation behavior [10]. The green block represents a constant applied stress. The applied field H increases from (a) to (c).

This process can be reversed to produce a sensing effect. A saturating field initially causes all the moments to align parallel to the rod axis. Increasing the applied compressive stress will cause the moments to rotate such that they are perpendicular to the rod axis. This causes a change in magnetization of the sample, which can be measured. This phenomenon is shown schematically in Figure 1.8.

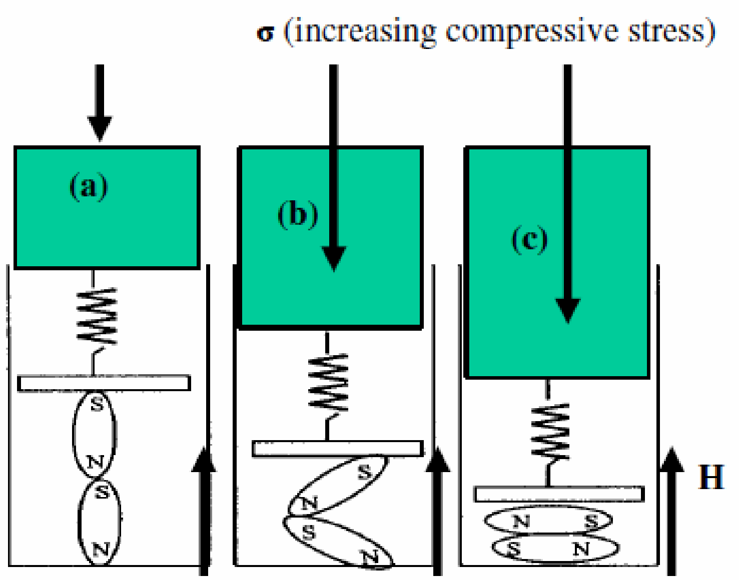

Figure 1.8: Schematic of Galfenol's sensing behavior [10]. The applied stress σ increases from (a) to (c).

Prior studies [2] on the effect of composition have identified Galfenol alloys with up to 30 atomic % gallium as the useable region of compositions. As shown in Figure 1.9, magnetostriction peaks are observed in samples having 18 and 27.5 atomic % Ga. Below 17 atomic % Ga, Fe-Ga alloys exhibit the disordered A2 phase, as seen in Figure 1.10. Above 17%, ordered structures such as B2 and D03 begin to be observed, which hinder the magnetostriction [11]. The second magnetostriction peak at 27.5 atomic % Ga is attributed to the extraordinary lattice softening of the alloy [2]. Since it is desired to use the high magnetostriction as well as good mechanical properties of the alloy in most applications, most transducer characterization studies have focused on the Galfenol alloys near the first peak.

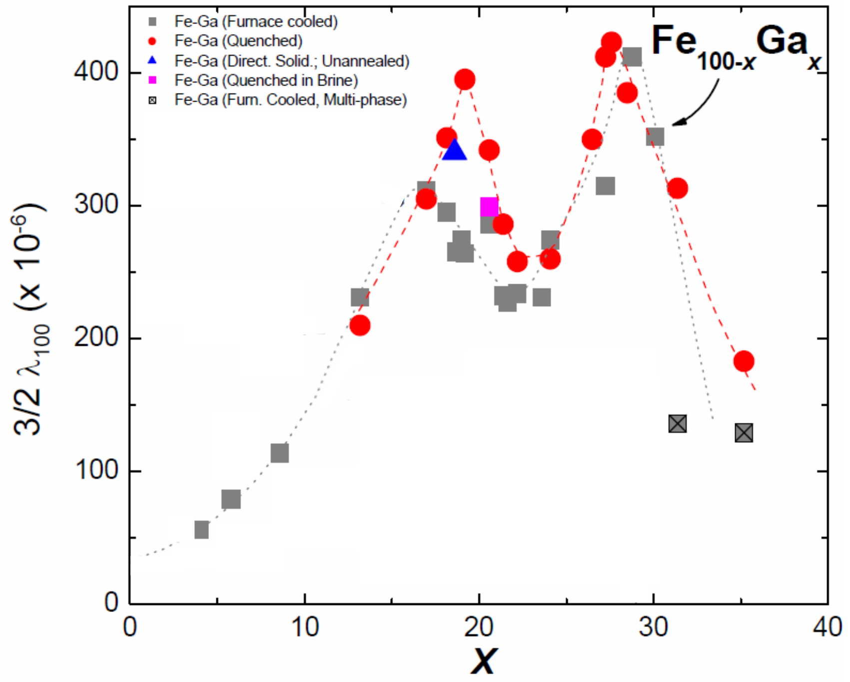

Figure 1.9: Magnetostriction as a function of alloy composition for Galfenol [12].

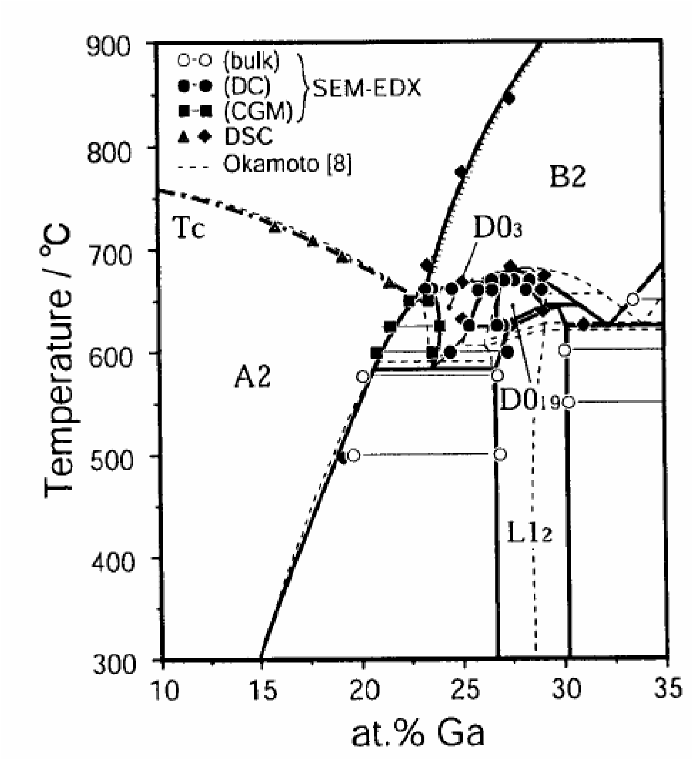

Figure 1.10: Fe-Ga phase diagram [13].

1.5 Cubic Crystal Elasticity

As discussed in Section 1.3, Galfenol possesses cubic crystal symmetry. An overview of the elastic properties for a cubic material is presented here. A generalized form of Hooke's law gives the relationship between stress and strain for an arbitrary material in terms of 6 elastic constants [14]:

$$\begin{bmatrix} \sigma_{11} \\ \sigma_{22} \\ \sigma_{33} \\ \tau_{23} \\ \tau_{13} \\ \tau_{12} \end{bmatrix} = \begin{bmatrix} c_{11} & c_{12} & c_{13} & c_{14} & c_{15} & c_{16} \\ c_{12} & c_{22} & c_{23} & c_{24} & c_{25} & c_{26} \\ c_{13} & c_{23} & c_{33} & c_{34} & c_{35} & c_{36} \\ c_{14} & c_{24} & c_{34} & c_{44} & c_{45} & c_{46} \\ c_{15} & c_{25} & c_{35} & c_{45} & c_{55} & c_{56} \\ c_{16} & c_{26} & c_{36} & c_{46} & c_{56} & c_{66} \end{bmatrix} \begin{bmatrix} \varepsilon_{11} \\ \varepsilon_{22} \\ \varepsilon_{33} \\ \gamma_{23} \\ \gamma_{13} \\ \gamma_{12} \end{bmatrix} \tag{1.1}$$

Equation 1.1 can also be written as:

$$[\sigma] = [c][\varepsilon] \tag{1.2}$$

or

$$[\varepsilon] = [S][\sigma] \tag{1.3}$$

where the [S] matrix (known as the compliance matrix) is the inverse of the [C] matrix (the stiffness matrix) written out in Equation 1.1.

Symmetry inherent in a material with a cubic structure allows Equation 1.1 to be simplified so it can be written in terms of only 3 independent elastic constants:

$$\begin{bmatrix} \sigma_{11} \\ \sigma_{22} \\ \sigma_{33} \\ \tau_{23} \\ \tau_{13} \\ \tau_{12} \end{bmatrix} = \begin{bmatrix} c_{11} & c_{12} & c_{12} & 0 & 0 & 0 \\ c_{12} & c_{11} & c_{12} & 0 & 0 & 0 \\ c_{12} & c_{12} & c_{11} & 0 & 0 & 0 \\ 0 & 0 & 0 & c_{44} & 0 & 0 \\ 0 & 0 & 0 & 0 & c_{44} & 0 \\ 0 & 0 & 0 & 0 & 0 & c_{44} \end{bmatrix} \begin{bmatrix} \varepsilon_{11} \\ \varepsilon_{22} \\ \varepsilon_{33} \\ \gamma_{23} \\ \gamma_{13} \\ \gamma_{12} \end{bmatrix} \tag{1.4}$$

This equation can also be written in the form of Equation 1.3, with three independent compliance terms in the [S] matrix. Therefore, to fully understand the elastic response of single crystal Galfenol, it is only necessary to know c_{11}, c_{12}, and c_{44}. From an engineering standpoint, however, it is often more useful to convert these properties into the Young's modulus and Poisson's ratio in the direction of interest.

The Young's modulus in an arbitrary direction [hkl] can be calculated using the following equation [15]:

$$\frac{1}{E_{[hkl]}} = S_{11} - 2\left(S_{11} - S_{12} - \frac{1}{2}S_{44}\right)\left(\alpha^2\beta^2 + \alpha^2\gamma^2 + \beta^2\gamma^2\right) \tag{1.5}$$

where α,β,γ are the direction cosines of the [hkl] direction with respect to [100], [010] and [001]. S_{11}, S_{12}, and S_{44} are the elastic compliances and they are related to the elastic stiffness constants for a cubic system as follows [15]:

$$S_{11} = \frac{c_{11} + c_{12}}{(c_{11} - c_{12})(c_{11} + 2c_{12})} \tag{1.6}$$

$$S_{12} = \frac{-c_{12}}{(c_{11} - c_{12})(c_{11} + 2c_{12})} \tag{1.7}$$

$$S_{44} = \frac{1}{c_{44}} \tag{1.8}$$

Similar concepts can be used to derive the directionally dependent Poisson's ratio equations (see Section 4.1.2).

From combining Equations 1.5 through 1.8, the elastic properties of interest in this study can be calculated. The following equations correlate the elastic properties to the individual elastic stiffness constants (c_{ij}) for a cubic system [9]:

$$E_{[100]} = \frac{c_{11} R}{c_{11} + c_{12}} \tag{1.9}$$

$$E_{[110]} = \frac{4 c_{44} R}{R + 2 c_{44}} \tag{1.10}$$

$$\nu_{[010]} = \frac{c_{12}}{c_{11} + c_{12}} \tag{1.11}$$

$$\nu_{[1\bar{1}0]} = \frac{R - 2 c_{44}}{R + 2 c_{44}} \tag{1.12}$$

$$\text{where } R = \frac{1}{c_{11}} (c_{11} - c_{12})(c_{11} + 2 c_{12}) \tag{1.13}$$

Applying a load along the [110] direction will cause auxetic behavior in the $[1\,\bar{1}0]$ direction, however it will also induce strain in the [001] direction. The combination of the strains in three directions results in approximate volume conservation. $\nu_{[001]}$ can also be calculated:

$$\nu_{[001]} = \frac{4 c_{12} c_{44}}{c_{11} (R + 2 c_{44})} \tag{1.14}$$

The set of Equations 1.9-1.13 can also be inverted to obtain the elastic stiffness constants as a function of the engineering elastic properties:

$$c_{11} = \frac{(1 - \nu_{[010]}) E_{[100]}}{(1 + \nu_{[010]})(1 - 2\nu_{[010]})} \tag{1.15}$$

$$c_{12} = \frac{\nu_{[010]} E_{[100]}}{(1 + \nu_{[010]})(1 - 2\nu_{[010]})} \tag{1.16}$$

$$c_{44} = \frac{RE_{[110]}}{2(2R - E_{[110]})} \tag{1.17}$$

$$c_{44} = \frac{R\nu_{[1\bar{1}0]} - R}{-2 - 2\nu_{[1\bar{1}0]}} \tag{1.18}$$

These relationships enable a thorough understanding of the elastic behavior of the Galfenol samples studied here.

1.6 Theoretical Approach

A theoretical model for predicting the elastic behavior of Galfenol was developed by Zhang and Wu at the University of California, Irvine [16]. To examine the effectiveness of this model, three Galfenol samples were chosen such that the results obtained experimentally in this thesis could be directly compared with results obtained by Zhang and Wu using their model. The comparison of the results of the two approaches is presented in Chapter 4. This section will provide an overview of the theoretical model.

The Vienna *ab initio* simulation package (VASP) [17,18] was used to investigate the mechanical behavior of Galfenol. As sketched in Figure 1.11, supercell models with 16 atoms were created for $Fe_{100-x}Ga_x$ ($x = 6.25 \sim 25$) alloys, in which 1, 2, 3 or 4 (6.25, 12.5, 18.75 or 25% respectively) of the 16 atoms in the supercell were Ga. Fe and Ga atoms were arranged in the bcc lattice, without Ga-Ga first neighborhood. The lattice sizes and atomic positions of these structures were optimized according to the energy minimization procedures guided by atomic forces.

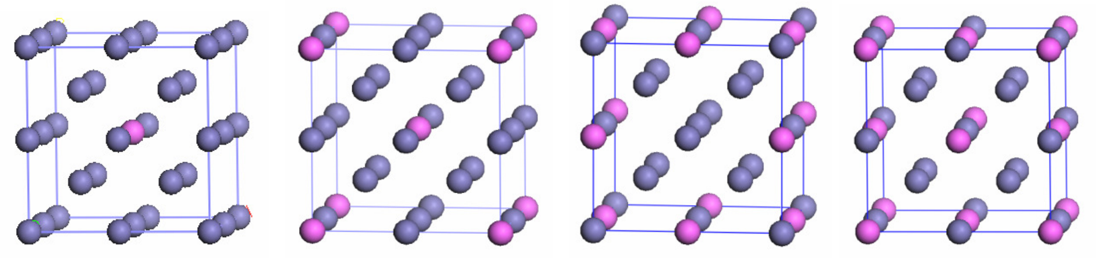

Figure 1.11: Atomic configurations for the cubic structures of $Fe_{100-x}Ga_x$ alloys with x=6.25, 12.5, 18.75 and 25. Blue and pink balls are for Fe and Ga atoms, respectively. [16]

The 16-atom supercell was employed in an attempt to balance the need for higher compositional resolution accuracy with constraints on computational time/processing capabilities. From test calculations with a 128-atom cell, it was observed that the elastic constants are rather insensitive to the cell size and change of distribution of Ga atoms.

For determining the elastic stiffness constants, c_{11}, c_{12} and c_{44}, different lattice strains were applied and the strain dependence of total energies was analyzed [19,20]. For example, c_{44} can be determined through the energy change, ΔE, under the tri-axial shear strain $e = (0, 0, 0, \delta, \delta, \delta)$ as:

$$\frac{\Delta E}{V} = \frac{3}{2} C_{44} \delta^2 \tag{1.19}$$

Similarly, the tetragonal shear modulus $C' = 1/2(C_{11} - C_{12})$ can be calculated from the volume-conserving orthorhombic strain $e = (\delta, \delta, (1+\delta)^{-2}-1, 0, 0, 0)$ by using:

$$\frac{\Delta E}{V} = 6C'\delta^2 + O(\delta^3) \tag{1.20}$$

1.7 Experimental Investigation Overview

The experimental investigation was undertaken in two parts. The first stage was tensile testing. For these experiments, single crystal samples of Galfenol were cut into the shape of dogbone tensile specimens, and were elastically loaded at a constant strain rate. From this, the Young's modulus and Poisson's ratio were calculated. The second stage was resonant ultrasound spectroscopy (RUS), which is a technique that predicts the elastic behavior of a material by measuring its resonant frequencies. For these experiments, single crystal parallelepipeds of Galfenol were used. The two sets of results were then compared. In addition, the tensile testing and RUS results were compared with the theoretical model discussed in Section 1.6.

Chapter 2: Tensile Testing

This section describes the tensile testing done in this study. It begins with the preparation and analysis of the samples used, including the results of composition analysis of the test specimens. It next reviews the test equipment, data acquisition and reduction, and the overall test procedure. It then discusses the finite element analysis study of the tensile samples. It concludes with the results of the tensile testing and a discussion section.

2.1 Sample Preparation

Since the elastic properties of single-crystal Galfenol are dependent on composition, crystal orientation and heat treatment, a discussion of the samples used in this study is presented here.

2.1.1 Material preparation

The samples were prepared at the DOE Ames Laboratory as follows. A single crystal of $Fe_{100-x}Ga_x$ was grown in an alumina crucible by the modified Bridgman technique. The starting ingot for single crystal growth was prepared by arc-melting appropriate quantities of Fe (99.99% purity) and Ga (99.999% purity) metal several times under an argon atmosphere. The button was then re-melted, and the alloy was drop-cast into a copper chill cast-mold to ensure compositional homogeneity throughout the ingot. The alloy was heated in a vacuum of 1.3×10^{-4} Pa up to 1075 K to degas the crucible and charge. The chamber was then backfilled to a pressure of 275 kPa with high purity argon. The ingot was then further heated to the growth temperature and held for 1 hour to allow thorough mixing before withdrawing the sample from the heat zone at a rate of 4 mm/h. Following growth, the ingot was annealed at 1000 ºC for 168 hours. Several samples were additionally annealed later at 800 ºC for 1 hour under flowing argon and then water quenched.

2.1.2 Specimen preparation

The crystal orientation was determined within 0.25º using Laue X-ray back reflection and then cut into tensile specimens (Figures 2.1 and 2.2) by electro-discharge machining. After machining, the orientation of each specimen was again checked by Laue X-ray back reflection.

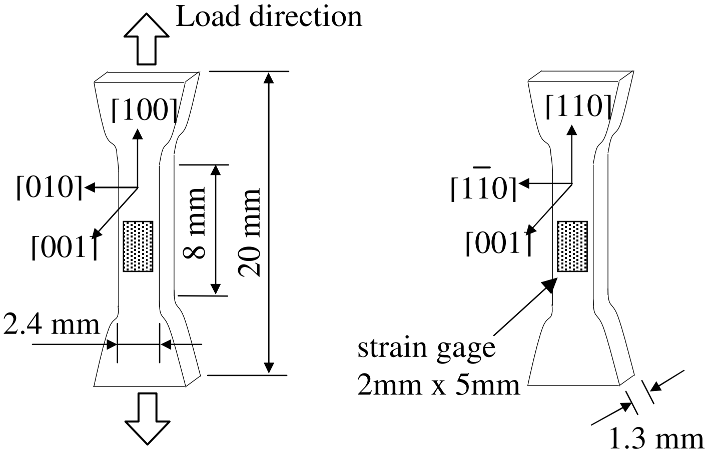

Figure 2.1: Schematic of the [100] and [110] Fe-Ga dogbone tensile samples used in this study.

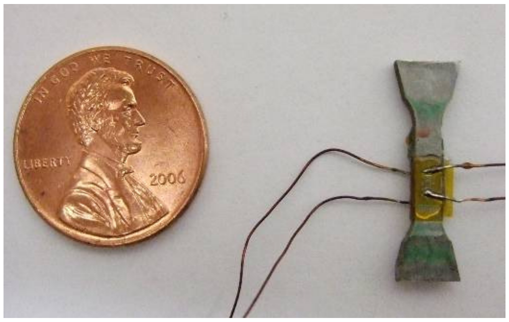

Figure 2.2: Photo of a typical Fe-Ga dogbone tensile sample.

2.2 Specimen Analysis

Energy dispersive X-ray spectroscopy (EDS) and wavelength dispersive X-ray spectroscopy (WDS) were used to determine the composition of each specimen. A sample of known composition of $Fe_{35}Ga_{65}$ was used with each specimen as a calibration standard. Three points were chosen along the surface of each sample, and the composition at each point was measured to an accuracy of 0.21 percent or better. The composition of each sample was given by Ames Laboratory when the samples were first manufactured, however, no specific information about precision or accuracy was provided. In addition, most of the samples were produced about four years ago, and re-measuring the composition was an opportunity to ensure that the gallium had not depleted over time. Most of the samples were close to their specified nominal values. Table 2.1 summarizes the results.

Table 2.1: Composition analysis of the Fe-Ga dogbones.

Orientation	**Nominal Ga content (at%)**	**Measured Ga content (at%)**	**Change**	**Relative change**
[100]	12.5	11.9 ± 0.1	- 0.6	- 4.8%
[110]	12.5	12.0 ± 0.2	- 0.5	- 4.0%
[100]	17	17.5 ± 0.3	+ 0.5	+ 2.9%
[110]	17	17.3 ± 0.3	+ 0.3	+ 1.8%
[100]	19	19.1 ± 0.2	+ 0.1	+ 0.53%
[110]	19	19.1 ± 0.5	+ 0.1	+ 0.53%
[110]	18.7	19.5 ± 0.2	+ 0.8	+ 4.3%
[100]	21	21.1 ± 0.1	+ 0.1	+ 0.48%
[110]	21	21.1 ± 0.2	+ 0.1	+ 0.48%
[100]	25	25.4 ± 0.1	+ 0.4	+ 1.6%
[110]	25	25.3 ± 0.3	+0.3	+ 1.2%

Six of the tensile samples underwent a heat treatment at 800° C for one hour. As a result of this, the samples all showed gallium depletion, which is commonly observed. The compositions of those six samples were measured using WDS before and after heat treatment. Those results are presented in Table 2.2.

Table 2.2: Composition analysis of the Fe-Ga samples before and after a heat treatment of 800° C for one hour.

Orientation	**Original Ga content (at%)**	**Final Ga content (at %)**	**Change**	**Relative change**
[100]	17.5	14.6 ± 0.6	- 2.9	-16%
[110]	17.3	15.8 ± 1.3	-1.5	- 8.7%
[100]	19.1	18.2 ± 0.3	-0.9	- 4.7%
[110]	19.1	17.9 ± 0.5	-1.2	- 6.3%
[100]	21.1	20.4 ± 0.2	-0.7	- 3.3%
[110]	21.1	20.4 ± 0.3	-0.7	- 3.3%

2.3 Experiment Procedure and Equipment

2.3.1 Test procedure

Each specimen was subjected to tensile testing using a hydraulic MTS machine operating at constant cross-arm velocity of either 0.5 μm/s or 1 μm/s, which applied a maximum load corresponding to approximately 150 MPa. This was below the predicted yield strength for all the samples (~500 MPa [9]). Because of slight differences in cross-sectional area, the stress varied slightly for each sample. The tests were done at room temperature and without an applied magnetic field. Special fixtures were used to accommodate the small size of the specimens and to ensure that the load was applied along the desired axis.

2.3.2 Experiment equipment

During testing, the specimen was housed in a gripper, which is shown in Figure 2.3. The gripper was fabricated from 1018 steel, a high strength material. The gripper had a self-aligning groove to center the specimen. To ensure that the specimen was under pure tension, the gripper was attached to the MTS machine via a universal joint at the top and a ball bearing rod eye connected to a clevis at the bottom. These connections prevented the specimen from bending or slipping during loading. The overall test configuration is shown in Figure 2.4.

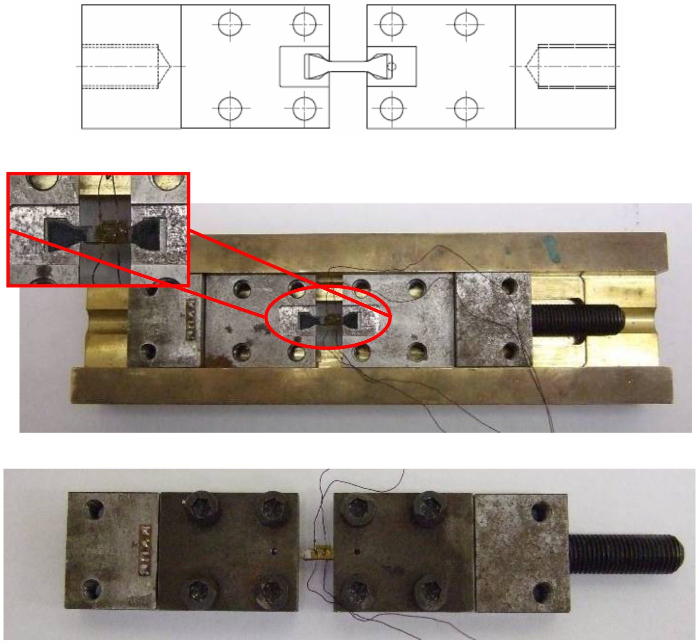

Figure 2.3: The Fe-Ga dogbone tensile test specimen being installed in the gripper.

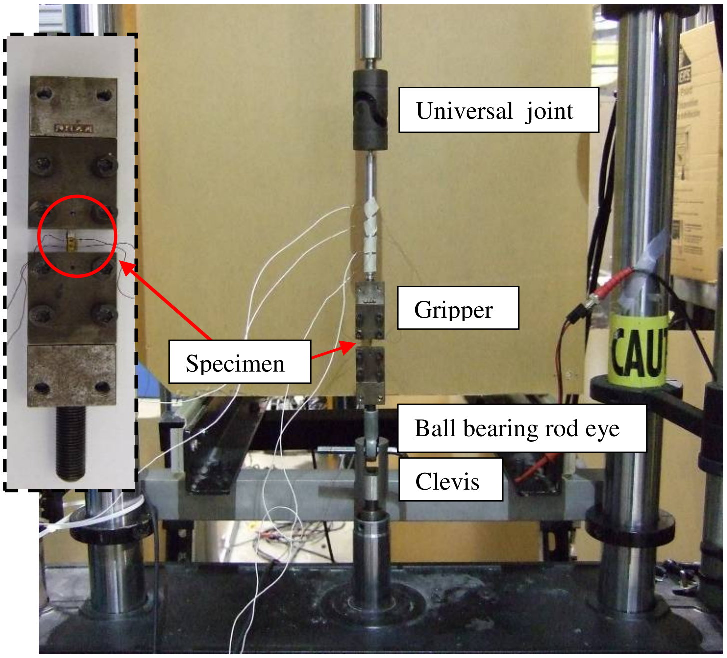

Figure 2.4: Fe-Ga tensile test set-up.

In this setup, the dogbone is connected to a fixed load cell at the top and the moving head at the bottom. As the head first begins to move downwards, the universal joint at the top will rotate if necessary to ensure the load is applied directly along the axis of the dogbone. Once that occurs, stress begins to accumulate in the sample. The gripper is designed to transfer the load through the sides of the dogbone (as opposed to the faces). This is illustrated in Figure 2.5. It can be assumed that once the sample is aligned, the top portion of the dogbone is fixed in place. The load is applied to the gripper, and then transferred to the dogbone through the contact areas between the gripper and the sides of the lower half of the dogbone (the red areas in Figure 2.5). This results in constant stress in the middle section of the dogbone. This is verified in Section 2.4.

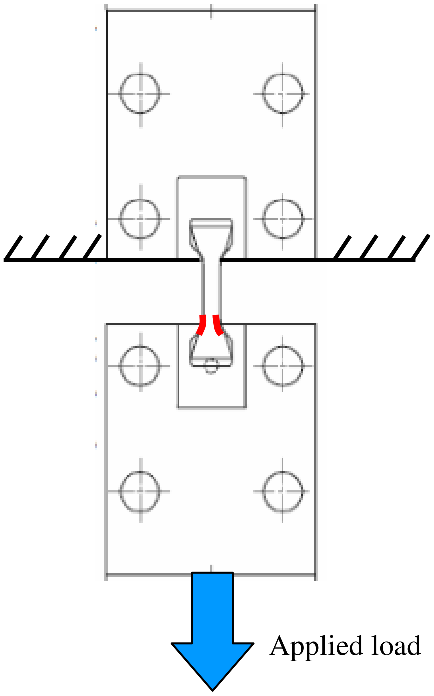

Figure 2.5: The application of load and generation of strain in the dogbones.

2.3.3 Data acquisition

Each specimen had two strain gages attached to it. One strain gage measured the strain in the longitudinal direction (Vishay MicroMeasurements EA-06-015DJ 120) and the other measured the strain in the transverse direction (EA-06-015EH 120). Because of the small size of the specimens, there was only space for one strain gage on each side. Each strain gage was connected to a strain indicator (Vishay 3800), which were connected to a PC-based data acquisition system. The load data were measured by the force cell in the MTS machine, which was also connected to the PC-based data acquisition system.

2.3.4 Error reduction

To check for avoidable errors and to compensate for unavoidable errors, each of the elastic properties reported in this study were measured numerous times. Each specimen was tested with one set of strain gages, and then retested with a different set of strain gages. The [110] samples were each tested with three different sets of strain gages because they showed more variation. In addition, each specimen's response to the loading process was recorded and analyzed several times for each set of strain gages. The variation in these tests was minimal, suggesting that most of the variation arose from misalignment of the gages.

2.3.5 Data reduction

A Matlab script was used to analyze the data from each test. The raw data consisted of the applied load, the longitudinal strain and the transverse strain. The load was converted to stress for each sample. From this, a stress vs. strain plot was created for each sample. Many of the samples showed a slight curvature in the stress-strain plot at low stress values (generally the first 5% of the data) before the dependence became linear. This slight curvature arises from the delta-E effect, which occurs in ferromagnetic materials from the relationship between applied stress and local magnetization in the sample [21,22]. In an unstressed sample under no magnetic field, the internal magnetic moments are randomly oriented. As stress is applied, the moments rotate to align themselves with the direction of the load. This is the cause of the nonlinearity in the stress-strain plots for this material. Since it generally requires under 10 MPa for the moments to align, the stress-strain plot becomes linear after that point.

From the collected data, the elastic properties of interest can be calculated. The Young's modulus was calculated as the average ratio of stress to strain from the linear portion of the stress-strain curve, which was typically taken to be the last 40% of the data. This corresponds to approximately 3000 data points. The Poisson's ratio was calculated as the average of the negative ratio of transverse strain to longitudinal strain, also from the linear portion of the stress-strain curve.

$$E = \frac{1}{n}\sum_{n}\frac{\sigma_n}{\varepsilon_{long,n}} \tag{2.1}$$

$$\nu = \frac{1}{n}\sum_{n}\frac{-\varepsilon_{tran,n}}{\varepsilon_{long,n}} \tag{2.2}$$

where *n* represents the number of data points.

The low-load modulus and Poisson's ratio are also presented. These are calculated from the slope of the data as the load decreases from 10 MPa to zero, which is the range of the delta-E effect. These values will be presented in Section 2.6, and will be included in the comparison of the results obtained from tensile testing and RUS in Chapter 4.

Figures 2.6 and 2.7 show a typical set of stress-strain curves. Figure 2.6 is for the 21.1% [100] sample and Figure 2.7 is for the 21.1% [110] sample. The delta-E effect is visible in the start of the data in Figure 2.6. The negative Poisson's ratio is apparent in Figure 2.7 as the slopes of both strain curves are always positive.

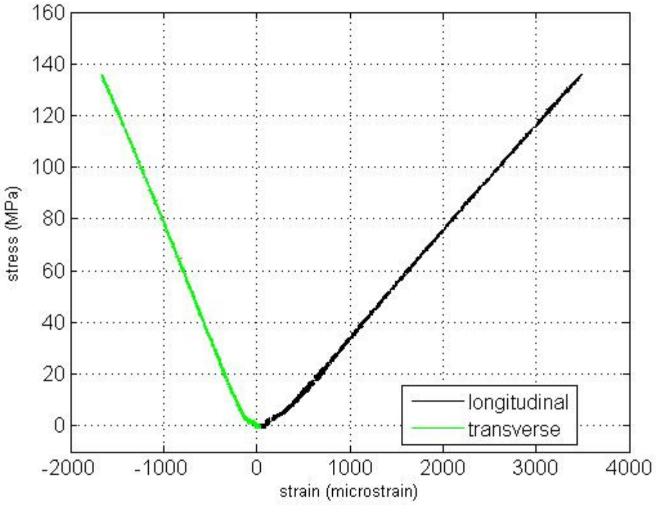

Figure 2.6: Stress-strain plot for 21.1% sample aligned along the [100] direction.

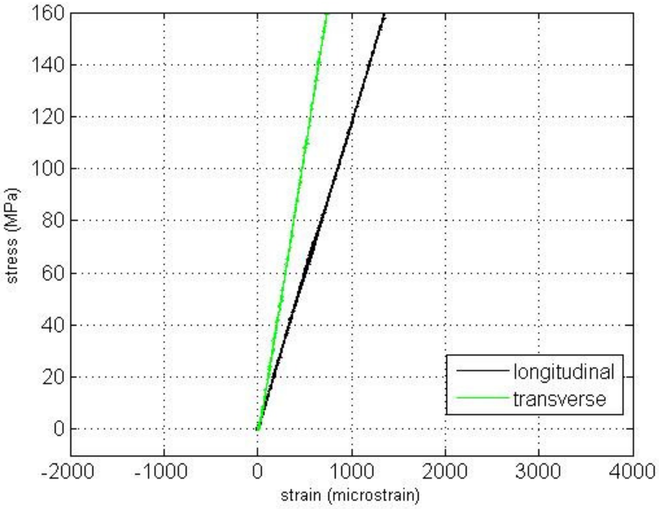

Figure 2.7: Stress-strain plot for 21.1% sample aligned along the [110] direction.

2.4 FEM Analysis

Having to apply the tensile testing method to single crystal samples necessitated that the dogbones be smaller than ASTM standard size. A finite element model of the dogbone tensile sample was generated using ANSYS to examine the stress distribution. The element used in the dogbone model was a solid tetrahedron with 10 nodes, shown in Figure 2.8.

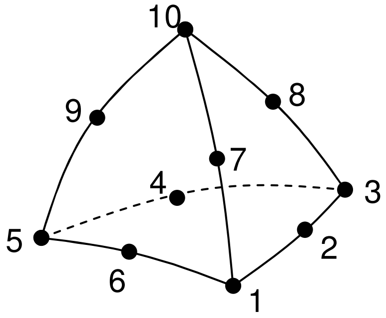

Figure 2.8: Element used in the FEM of dogbone specimen.

The model was comprised of 2390 elements and 4574 nodes, which was the finest mesh allowable. The dogbone with the mesh is shown in Figure 2.9.

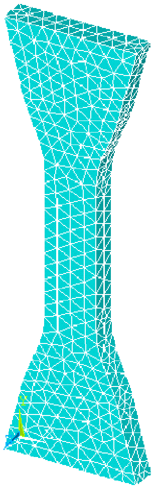

Figure 2.9: ANSYS model of dogbone after meshing.

To simulate the method of tensile testing employed in this study as accurately as possible, the dogbone model's position was constrained at the areas where the gripper holds the specimen. This is represented by the purple sections in Figure 2.10.

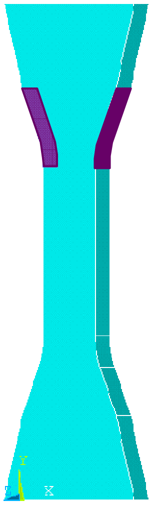

Figure 2.10: The applied constraint on the model. The purple regions represent areas given a fixed displacement of zero.

The strain in the model was produced by applying a fixed displacement at the areas where the load is transferred from the gripper to the specimen. This is represented by the purple sections in Figure 2.11. The amount of applied displacement was taken from measurements made by the displacement sensor in the MTS machine during tensile tests.

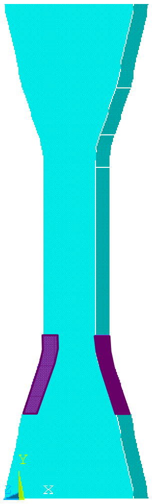

Figure 2.11: The applied load on the model. The purple regions represent areas given an applied displacement.

The analysis showed that the tensile stress is constant throughout the region covered by the strain gage. Figure 2.12 shows the ANSYS model prediction of the tensile stress in the dogbone. It also includes a to-scale schematic of a strain gage showing that it is contained inside the constant stress range.

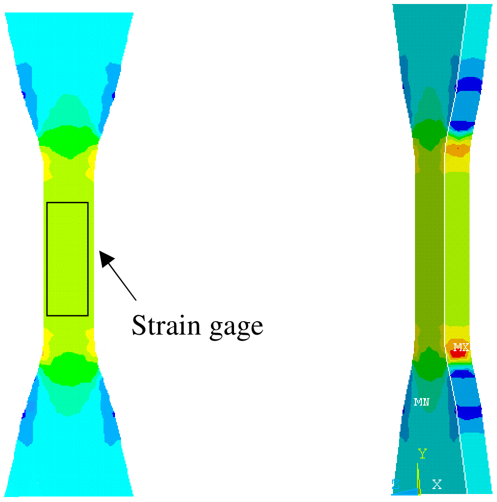

Figure 2.12: Front view and side view of the ANSYS model of tensile stress in the dogbone tensile specimen.

As an additional check, the displacement in the direction of the load was plotted. As expected, the displacement increases linearly along the length of the dogbone. This is shown in Figure 2.13.

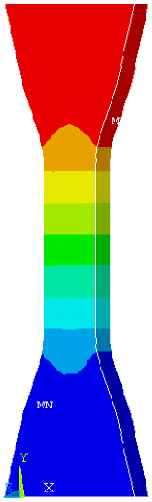

Figure 2.13: Displacement in the direction of the load.

2.5 Results and Discussion

2.5.1 Results

The tensile testing provided direct measurements of $E_{[100]}$, $\nu_{[010]}$, $E_{[110]}$ and $\nu_{[1\bar{1}0]}$ for a variety of compositions. The results from the [100] samples are presented in Table 2.3, and the [110] samples are in Table 2.4. In addition, stress-strain plots for all the samples tested in this study can be found in Appendix A. As mentioned earlier, each sample was tested with at least two sets of strain gages. The deviation provided in the tables is one standard deviation about the mean of the data taken for each composition.

Table 2.3: Elastic properties for single crystal Fe-Ga tensile specimens aligned along the [100] direction.

Ga content (at %)	**$E_{[100]}$ (GPa)**	**$\nu_{[010]}$**
11.9	80.0 ± 1.27	0.47 ± 0.021
14.6	63.2 ± 3.39	0.40 ± 0.0
17.5	60.5 ± 0.707	0.42 ± 0.0071
18.2	63.5 ± 2.12	0.43 ± 0.021
19.1	56.5 ± 2.12	0.47 ± 0.050
20.4	52.9 ± 0.707	0.45 ± 0.014
21.1	39.5 ± 0.707	0.51 ± 0.035
25.4	24.4 ± 1.70	0.49 ± 0.057

Table 2.4: Elastic properties for single crystal Fe-Ga tensile specimens aligned along the [110] direction.

Ga content (at %)	**$E_{[110]}$ (GPa)**	**$\nu_{[1\bar{1}0]}$**
12.0	167 ± 5.00	-0.27 ± 0.080
15.8	156 ± 7.51	-0.44 ± 0.055
17.3	161 ± 8.39	-0.51 ± 0.095
17.9	158 ± 6.66	-0.46 ± 0.104
19.1	164 ± 6.25	-0.61 ± 0.124
19.5	149 ± 7.64	-0.55 ± 0.076
20.4	132 ± 8.08	-0.48 ± 0.035

21.1	112 ± 7.37	-0.54 ± 0.012
25.3	90.5 ± 1.41	-0.66 ± 0.035

From this study, it is possible to examine trends in the elastic properties as a function of composition. This will enable estimation of the mechanical properties of alloys not studied here. Each of the four measured elastic properties is plotted in Figures 2.14 through 2.17. Again, the error bars represent one standard deviation about the mean of the data taken for each composition. The values for single crystal pure iron as measured by McLean [23] are included in the plots (blue circle marker) for reference.

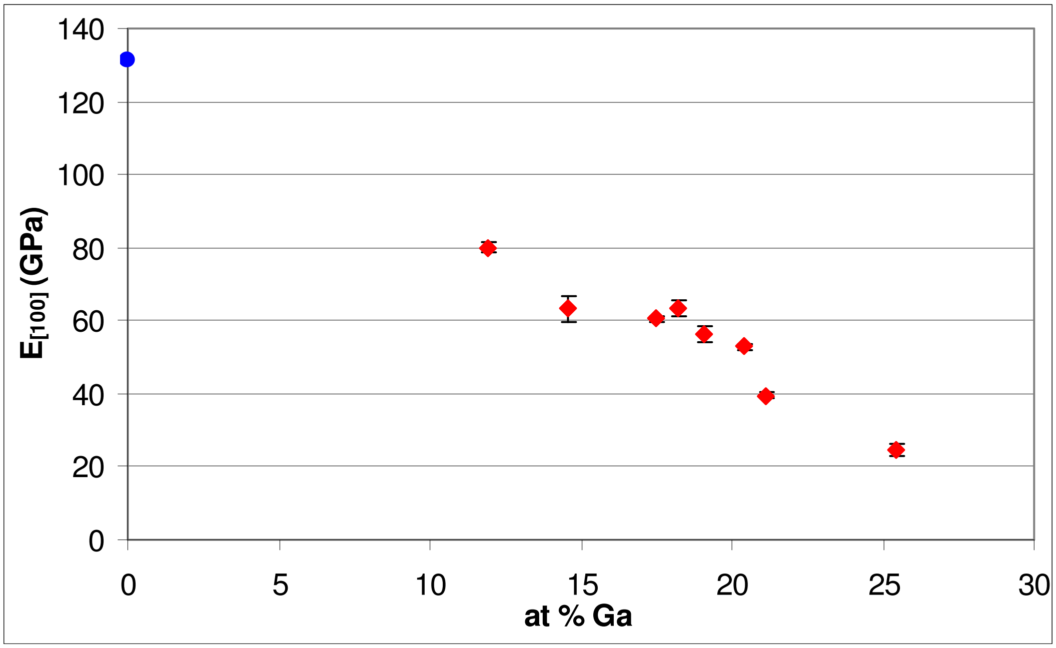

Figure 2.14: $E_{[100]}$ as a function of alloy composition.

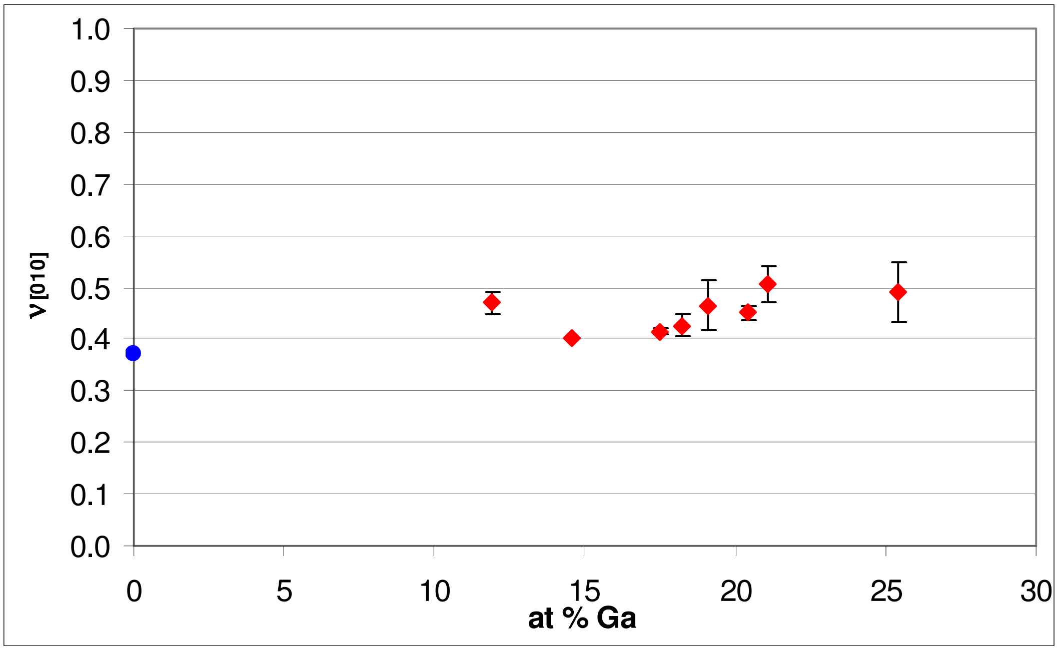

Figure 2.15: $\nu_{[010]}$ as a function of alloy composition.

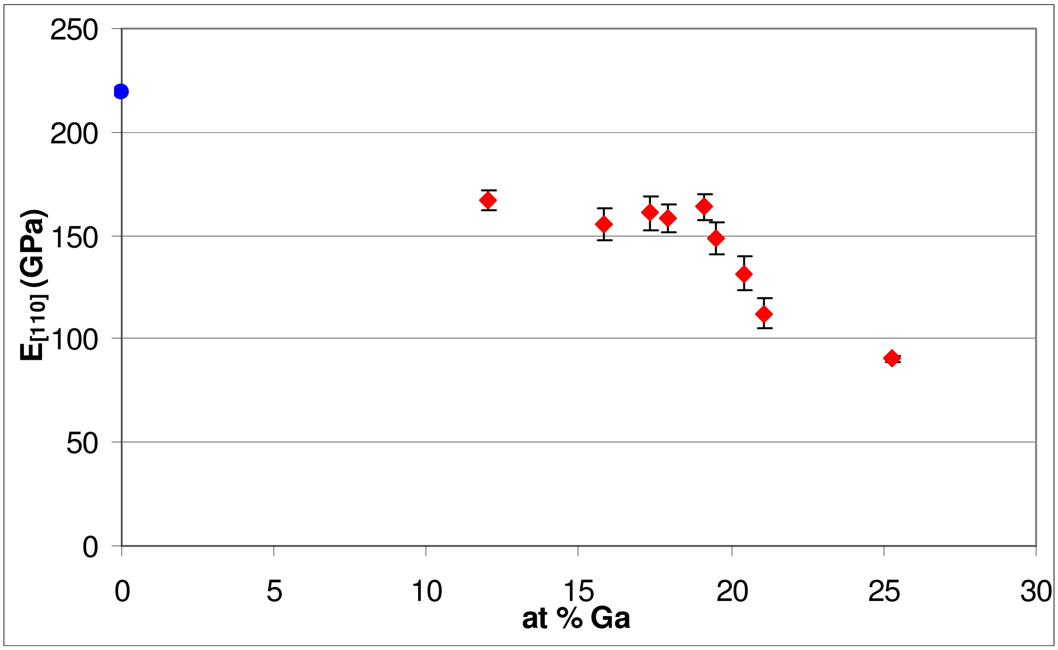

Figure 2.16: $E_{[110]}$ as a function of alloy composition.

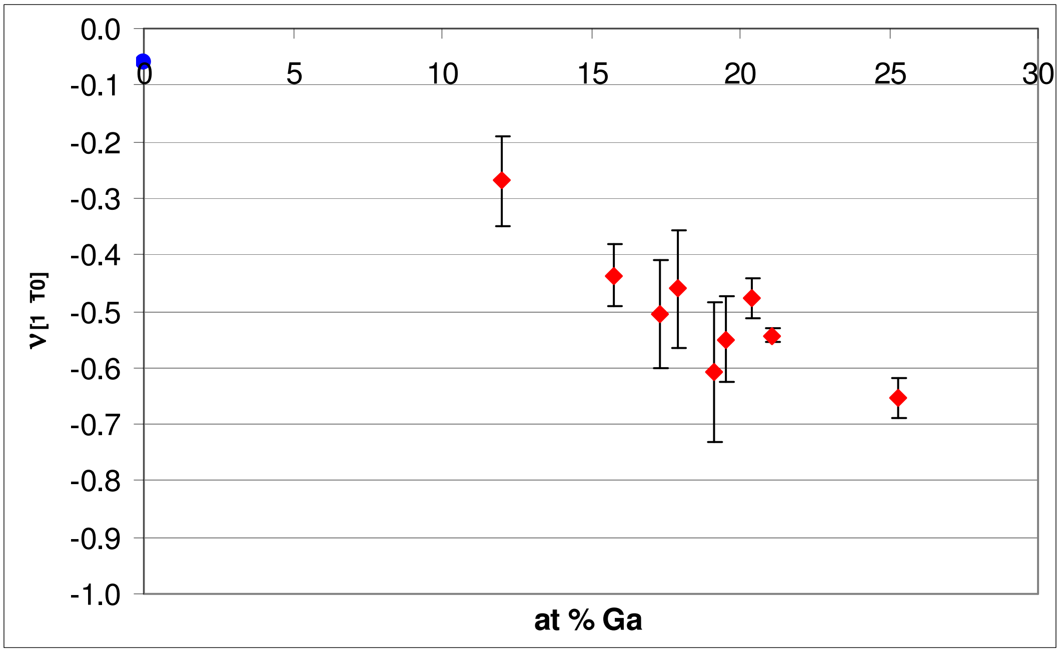

Figure 2.17: $\nu_{[1\ \bar{1}0]}$ as a function of alloy composition.

2.5.2 Discussion

Numerous measures were taken to ensure the accuracy of the results, however, some errors and variance in data was observed. To check the validity of the testing procedure, a steel calibration sample was used. The dimensions of the sample were similar to the typical dimensions of the Galfenol specimens, and the sample was tested using the exact same equipment and procedure. The measured Young's modulus was 217 GPa and the Poisson's ratio was 0.33. The published values for this material are 207 GPa and 0.30 [24].

Errors in the measured strain will propagate into the calculated values of the Young's modulus and Poisson's ratio. Misalignment of the strain gages can lead to slight inaccuracies, since then the measured strain should be scaled by the cosine or sine of the angle between the gage and the load direction for the longitudinal and transverse strains, respectively. For example, a longitudinal strain gage misaligned by 5º would underestimate the longitudinal strain by a factor of 1-cos(5º), or 3.8%. Similarly, a transverse stain gage misaligned by 5º would underestimate the transverse strain by a factor of 1-sin(85º), or 3.8%.

Finally, because of challenges in the manufacturing of the samples, not all of them were the ideal size for the gripper system. Slipping was occasionally observed during runs, however these runs were terminated once slipping started and were not used in the analysis.

The error bars in the measurement of the negative Poisson's ratio are relatively large. This partly comes from the fact that the Young's modulus in the [110] direction is much larger than it is in the [100] direction, meaning the maximum measured strain in the [110] direction is smaller than in the [100] direction. This is illustrated in Figure 2.18 for a 21.1% Ga sample. Since the magnitude of the strain in the [110] direction is so much smaller, the intrinsic errors in the strain measurement will be a larger percent of the total strain. The same is generally true for the strain transverse to the load direction; the transverse strain in the [110] direction is generally smaller than for the [100] direction. Since the Poisson's ratio is a ratio of the two strains, the larger percent error in the strain measurement results in a larger error for the Poisson's ratio. Errors intrinsic in the experiment included uncertainty in the strain indicator box (0.1 $\mu\varepsilon$), uncertainty in the load cell (2.23 lbs), and experiment noise (~10 $\mu\varepsilon$).

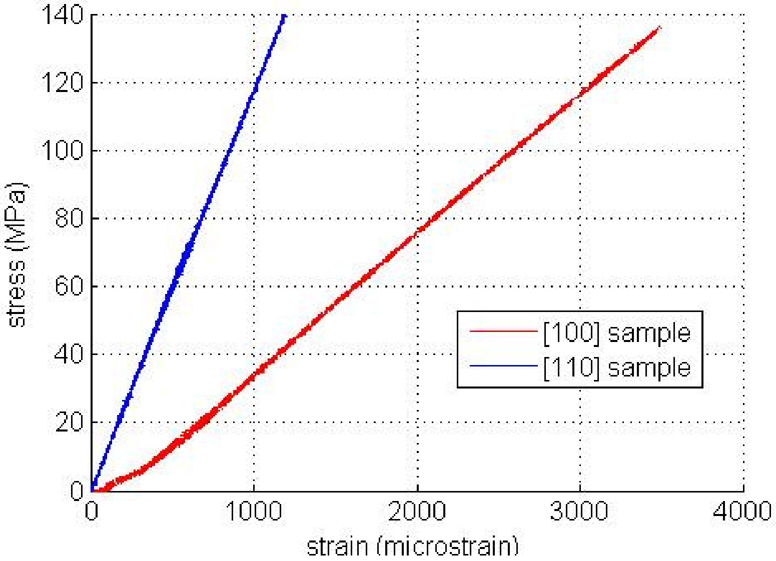

Figure 2.18: Comparison of the longitudinal strain along the [100] and [110] directions for $Fe_{78.9}Ga_{21.1}$.

2.5.3 Comparison with literature data

Other researchers have also examined the elastic properties of Galfenol. Kellogg [25] and Yoo [26] used a tensile testing procedure very similar to the one employed in this study. Clark et al. [2] used resonant ultrasound spectroscopy (see Chapter 3) to measure the elastic stiffness constants and then predict the engineering elastic properties. To compare the results of this study with the results of other studies, and to present a full picture of the known elastic properties, all known engineering elastic properties are plotted in Figures 2.19 through 2.22. The values for pure iron are again included.

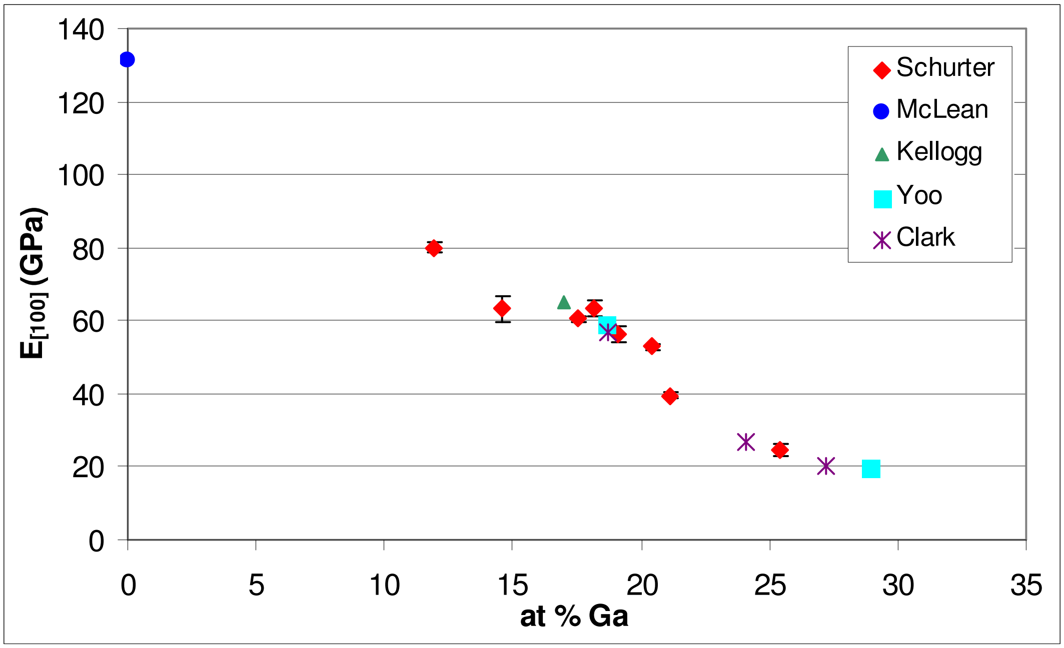

Figure 2.19: $E_{[100]}$ as a function of composition, including the results of this study and published data from other researchers.

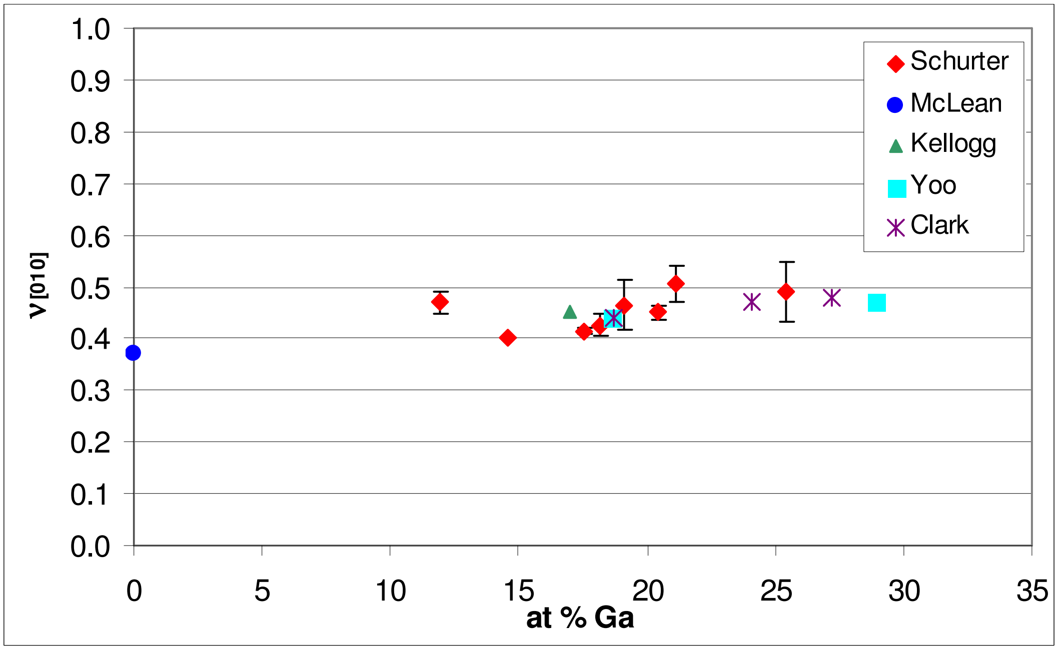

Figure 2.20: $\nu_{[010]}$ as a function of composition, including the results of this study and published data from other researchers.

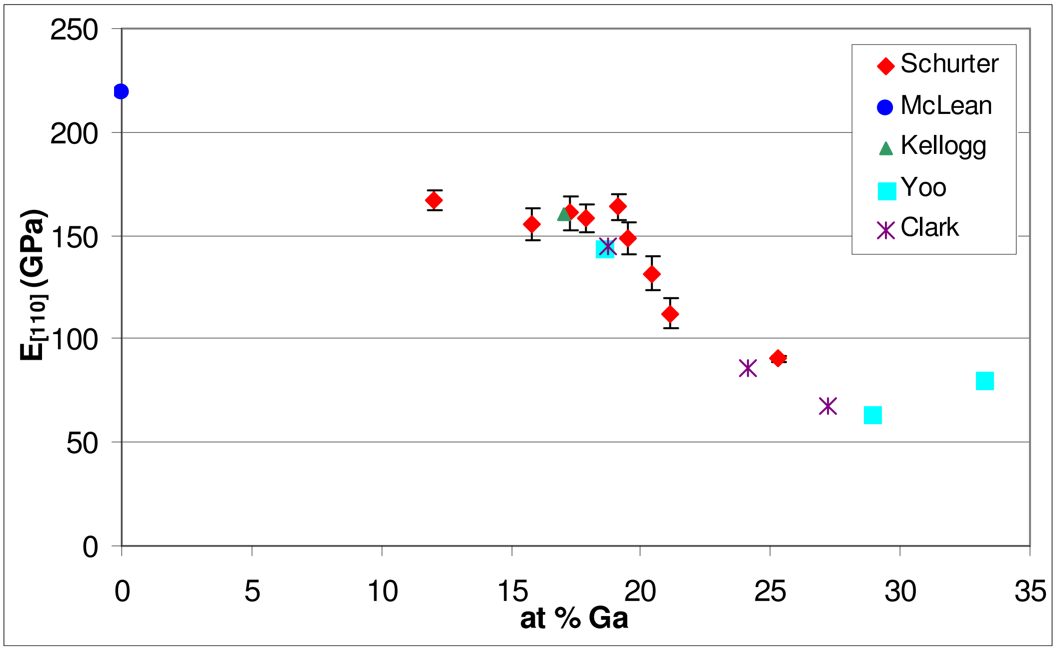

Figure 2.21: $E_{[110]}$ as a function of composition, including the results of this study and published data from other researchers.

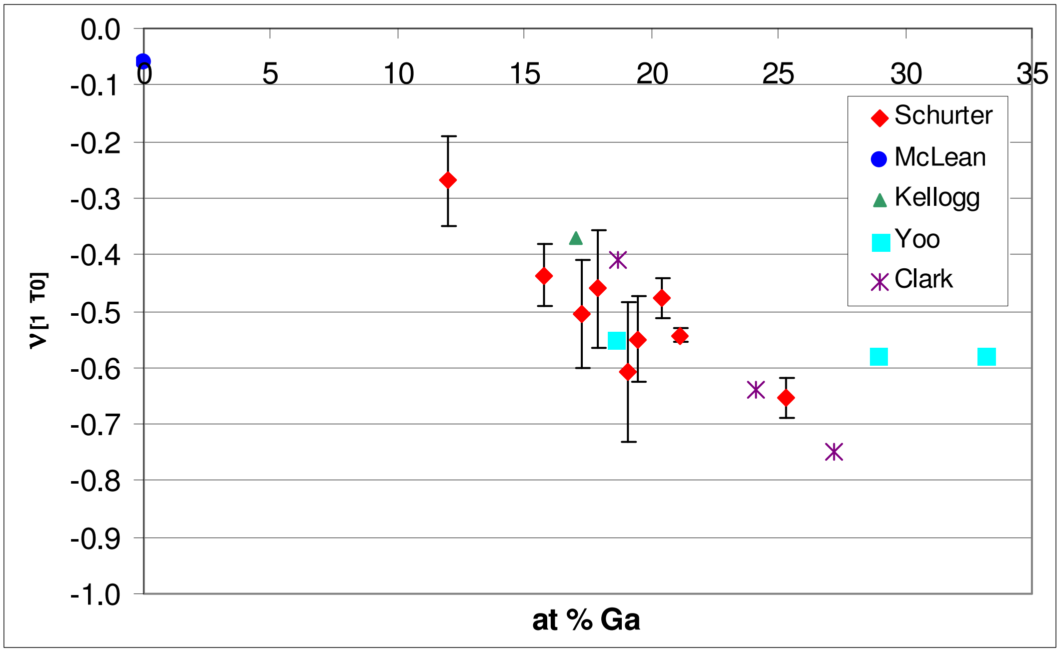

Figure 2.22: $\nu_{[1\ \bar{1}0]}$ as a function of composition, including the results of this study and published data from other researchers.

In general, there is good agreement between the various sets of data. $E_{[100]}$ appears to decrease as the gallium content increases. $\nu_{[010]}$ increases to just below 0.5 (the thermodynamic maximum [6]). $E_{[110]}$ also decreases as the gallium content increases. The trend in $\nu_{[1\bar{1}0]}$ is a little more difficult to identify, but in general it also decreases.

One potential reason for the differences between the sets of data is the lack of either x or y error bars for the other sets of data. As seen in this study, the labeled composition of a sample is not necessarily its actual composition. As much as 0.8 atomic % Ga difference was measured (see Section 2.2). Another source of variation could be the phases present in each sample. Galfenol has a fairly complicated phase diagram, especially in the region between around 17 and 20% Ga (see Figure 1.9) [13]. The magnetostriction of Galfenol has been shown to be dependent not only on the alloy composition, but on the composition of the phases present [2], so it is possible that the elastic constants would also show some dependence.

2.6 Low-Load Elastic Properties

From the stress-strain plots, it is also possible to examine the elastic properties under very low stresses. These were obtained by analyzing the beginning of the stress-strain plots, typically from 0 to 10 MPa. Tables 2.5 and 2.6 present the low-load elastic properties for each sample alongside the conventional elastic properties as first presented in Tables 2.3 and 2.4. The scatter in the low-load results arises from the random orientation of the magnetic moments in the low-load region.

Table 2.5: Low stress and conventional elastic properties for single crystal Fe-Ga tensile specimens aligned along the [100] direction.

	$E_{[100]}$ (GPa)		**$\nu_{[010]}$**	
at % Ga	**Low stress**	**Conventional**	**Low stress**	**Conventional**
11.9	41.0 ± 1.30	80.0 ± 1.27	0.30 ± 0.027	0.47 ± 0.021
14.6	31.6 ± 3.40	63.2 ± 3.39	0.35 ± 0.0	0.40 ± 0.0
17.5	42.0 ± 0.98	60.5 ± 0.707	0.46 ± 0.016	0.42 ± 0.0071
18.2	54.1 ± 3.61	63.5 ± 2.12	0.38 ± 0.037	0.43 ± 0.021
19.1	36.4 ± 2.73	56.5 ± 2.12	0.40 ± 0.084	0.47 ± 0.050
20.4	44.1 ± 1.18	52.9 ± 0.707	0.33 ± 0.021	0.45 ± 0.014
21.1	30.6 ± 1.10	39.5 ± 0.707	0.51 ± 0.071	0.51 ± 0.035
25.4	15.8 ± 2.20	24.4 ± 1.70	0.20 ± 0.046	0.49 ± 0.057

Table 2.6: Low stress and conventional elastic properties for single crystal Fe-Ga tensile specimens aligned along the [110] direction.

	$E_{[110]}$ (GPa)		**$\nu_{[1\bar{1}0]}$**	
at % Ga	**Low stress**	**Conventional**	**Low stress**	**Conventional**
12.0	104 ± 6.24	167 ± 5.00	-0.16 ± 0.093	-0.27 ± 0.080
15.8	98.0 ± 9.45	156 ± 7.51	-0.18 ± 0.045	-0.44 ± 0.055
17.3	105 ± 11.0	161 ± 8.39	-0.43 ± 0.160	-0.51 ± 0.095
17.9	130 ± 10.9	158 ± 6.66	-0.30 ± 0.135	-0.46 ± 0.104
19.1	167 ± 12.7	164 ± 6.25	-0.73 ± 0.300	-0.61 ± 0.124

19.5	121 ± 12.4	149 ± 7.64	-0.58 ± 0.159	-0.55 ± 0.076
20.4	116 ± 14.3	132 ± 8.08	-0.62 ± 0.091	-0.48 ± 0.035
21.1	114 ± 14.9	112 ± 7.37	-0.73 ± 0.031	-0.54 ± 0.012
25.3	85.5 ± 2.66	90.5 ± 1.41	-0.48 ± 0.051	-0.66 ± 0.035

2.7 Conclusions

In summary, the tensile testing provided a large amount of new information, which will potentially be beneficial to future researchers.

1.) The engineering elastic properties of Galfenol were measured for a range of compositions, many of which were previously unstudied.

2.) Highly auxetic behavior was observed throughout the range of tests.

3.) A method for measuring the elastic properties of Galfenol (or other materials only available in small sizes) was developed.

Chapter 3: Resonant Ultrasound Spectroscopy

Resonant ultrasound spectroscopy (RUS) was conducted to examine the elastic properties of Galfenol. The samples used were Fe-Ga samples that directly correlated to samples from the tensile testing experiments. Sections 3.1 and 3.2 provide background information about the RUS analysis. Section 3.3 discusses the samples used and Section 3.4 discusses the experimental equipment and procedure. Section 3.5 provides the results and concludes with a discussion section.

3.1 Introduction to RUS

RUS is a technique that is very useful for measuring the elastic constants of samples that are only available in small sizes, which is typically the case for single crystals. Two piezoelectric transducers excite and measure the resonance frequencies of a sample, which are used to calculate the independent elastic stiffness constants of a material. The output signal shows voltage peaks at each resonance frequency. An algorithm uses the location of the resonance frequencies, as well as the dimensions and mass of the sample, to calculate the elastic constants. This is a nondestructive technique and is easily repeatable.

3.2 Theory of RUS

RUS makes use of the relationship between a sample's resonance frequency and its elastic properties. To illustrate this concept, the simplified case of a long, thin rod undergoing a longitudinal vibration is examined [27].

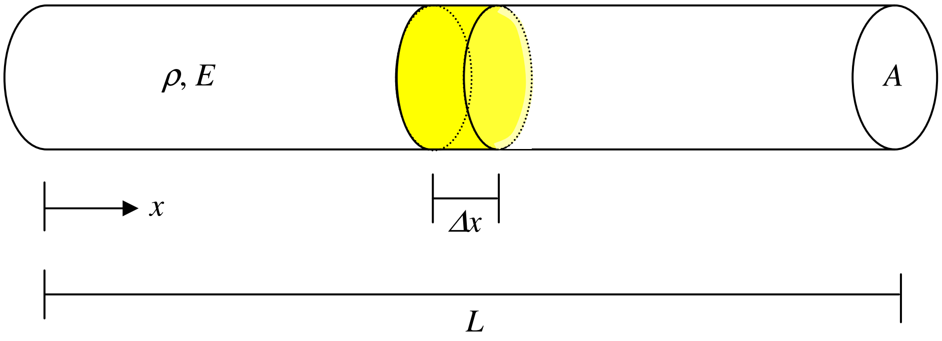

Figure 3.1: Long, thin rod undergoing a longitudinal vibration, with area *A*, length *L*, density *ρ*, and Young's modulus *E*.

The strain can be predicted at the left and right edges of the highlighted area:

$$\varepsilon_{left} = \frac{du(x,t)}{dx} \tag{3.1}$$

$$\varepsilon_{right} = \frac{du(x+\Delta x,t)}{dx} \tag{3.2}$$

where *u* is the displacement along the *x*-axis.

By summing the strain-induced forces, the total force experienced by the shaded area can be calculated:

$$P = AE\left(\frac{du(x+\Delta x,t)}{dx} - \frac{du(x,t)}{dx}\right) \tag{3.3}$$

The term inside the parenthesis can be simplified using the definition of the derivative:

$$\frac{d^2u(x,t)}{dx^2} = \frac{\frac{du(x+\Delta x,t)}{dx} - \frac{du(x,t)}{dx}}{\Delta x} \tag{3.4}$$

Thus, Equation 3.3 can be rewritten as:

$$P = AE\Delta x \frac{d^2u(x,t)}{dx^2} \tag{3.5}$$

To determine the motion of the shaded area, Newton's 2nd law is applied:

$$AE\Delta x \frac{d^2u(x,t)}{dx^2} = \rho \Delta x A \frac{d^2u(x,t)}{dt^2} \tag{3.6}$$

Simplifying reduces Equation 3.6 to:

$$\frac{d^2u}{dt^2} = \frac{E}{\rho}\frac{d^2u}{dx^2} \tag{3.7}$$

This is the wave equation in one dimension, where $\sqrt{E/\rho}$ is known to be the propagation speed of a wave in that material. The solution to the wave equation has the general form of:

$$u(x,t) = U_0 e^{i(kx-\omega t)} \tag{3.8}$$

where k is the wave number and ω is the resonance frequency. Their ratio can be expressed as:

$$\frac{\omega}{k} = \sqrt{\frac{E}{\rho}} \tag{3.9}$$

showing the relationship between elastic properties and resonance.

Unfortunately, when examining a three-dimensional sample the analysis is not as straightforward. The RUS algorithm uses similar concepts as in the 1D case to generate a matrix of equations that describe the energy state of the material. These equations are a function of the elastic constants and the resonance frequencies. The user inputs the sample dimensions and mass, a list of measured resonance frequencies (around 30 frequencies for the samples tested here) and initial guesses for the elastic constants. The algorithm then predicts the frequencies based on the guesses, and then uses those values to calculate the energy. It then slightly modifies the elastic constants and recalculates the frequencies and the energy state. This helps to mitigate the effects of human error in determining the resonance frequencies and the effects of imperfections in the shape and orientation of the sample. The program continues modifying the parameters until the overall energy is minimized. From this, the program can determine the elastic constants, the accuracy of each constant, the accuracy of each frequency and the overall accuracy of the collection of results.

3.3 RUS Samples

One of the primary goals of the RUS testing was to directly compare results obtained from tensile testing with results obtained from ultrasonic testing. To achieve this, several RUS samples were created from the already existing tensile samples.

This section details the process and challenges of creating the Fe-Ga samples for RUS.

3.3.1 Creation of the Fe-Ga samples

Samples to be analyzed using RUS need to be cut in a well-defined shape for the analysis to be possible. For this study, parallelepipeds with the edges aligned along the [100], [010] and [001] directions were selected. The RUS samples were therefore obtained by cutting a small parallelepiped out from the top of each of the [100] dogbones. This enables a direct comparison between the two testing methods employed here. Figure 3.2 shows a schematic of where the RUS samples were cut from the dogbones. Each sample was approximately 1.3 mm x 2.0 mm x 2.7 mm.

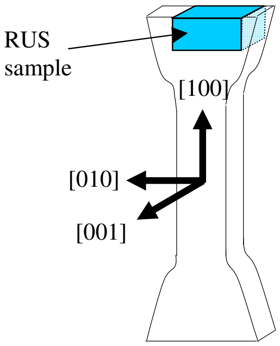

Figure 3.2: Schematic of the RUS sample location within the tensile sample.

Figure 3.3: Photo of a dogbone with RUS sample.

3.3.2 Orientation analysis of the Fe-Ga samples

Having properly aligned samples is crucial for RUS testing. The orientation of the RUS samples was measured by Ames Laboratory using X-ray diffraction (XRD). Each sample used in this study was required to be oriented with the faces parallel to the (100) planes within 2 degrees. Figure 3.4 shows the results of XRD for a sample with good orientation. Figure 3.5 shows the results of XRD for a sample with 3.2 degrees of misalignment. Figure 3.6 is a schematic representing the actual orientation of the sample in Figure 3.5.

Figure 3.4: XRD for a sample with good orientation.

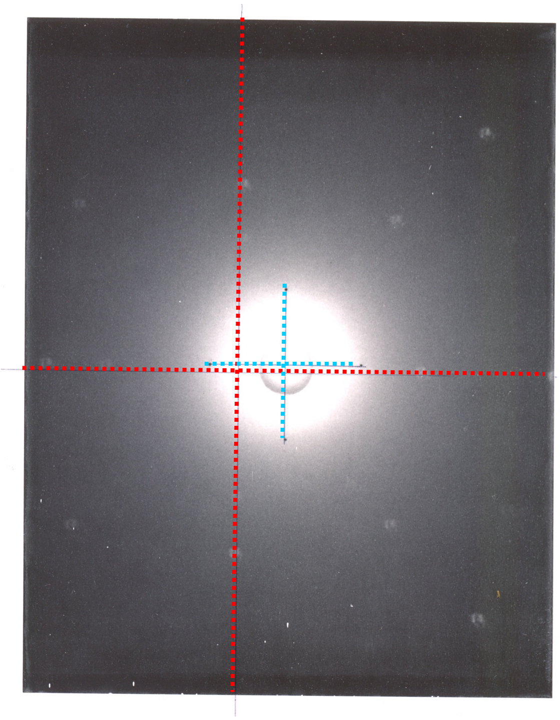

Figure 3.5: XRD for a sample with unacceptable orientation. The red lines are the ideal orientations, the blue lines are the actual orientation.

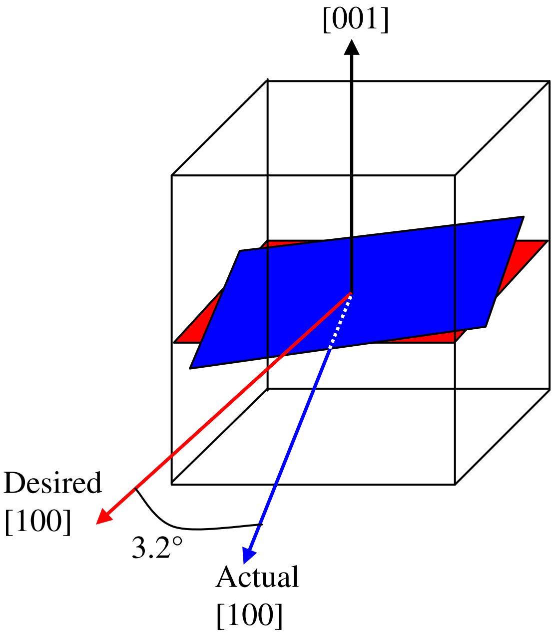

Figure 3.6: Schematic of the orientation of the sample that produced Figure 3.5.

3.3.3 Polishing and reshaping of Fe-Ga samples

Since the RUS samples were not grown specifically for use in RUS, the cut samples required some modifications. The analysis algorithm assumes the sample is a perfect parallelepiped with right angles, therefore the closer the sample shape is to perfect, the lower the error in the final results. To achieve this, the samples were filed and polished slightly. As a result of machining, some of the samples had a slight kink at one corner which needed to be removed. In addition, some of the samples had scratched surfaces. Figure 3.7 shows one of the samples before and after finishing.

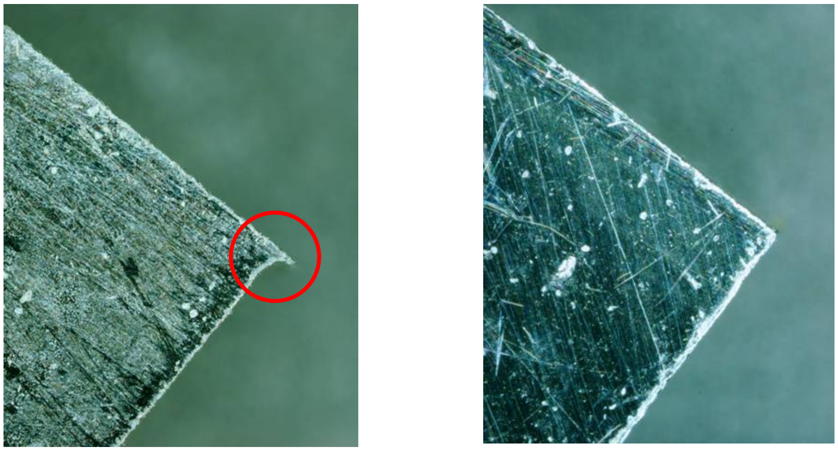

Figure 3.7: RUS sample as cut (left), and after filing and polishing (right).

3.4 RUS Testing Method

3.4.1 RUS equipment and procedure

The RUS apparatus used in this study consisted of two circular piezoelectric transducers placed on opposite faces of a parallelepiped sample. The transducers had a diameter of approximately 2mm and a thickness of approximately 0.5mm. One transducer acted as the actuator and the other as the sensor, however the transducers themselves were identical and both could be used as either an actuator or a sensor. The actuator excited the sample at a range of frequencies, and the sensor measured the response of the sample to each frequency. The response would peak sharply when the sample was excited at a resonance frequency. To minimize error, it is recommended to measure at least the first 24 resonance frequencies [27]. Therefore, in this study waves with frequencies ranging from 250 kHz to 1400 kHz were transmitted to the samples, corresponding to approximately the first 30 resonances.

In general, it is ideal to have the smallest contact area between the transducers and the sample to allow free vibration of the sample. Initially it was attempted to mount the samples standing on their edges or balancing on one corner, however, this resulted in significant scratching on the surface of the transducers which dramatically decreased the signal to noise ratio. Therefore, the samples were mounted on their smallest faces. Figure 3.8 shows a schematic of the different types of sample mounting, and Figure 3.9 shows a close-up photo of a sample mounted in the RUS apparatus. The top transducer was attached to the structure of the RUS apparatus such that it could be raised or lowered until it was just touching the sample. This meant that the sample did not support any of the weight of the top transducer and holder.

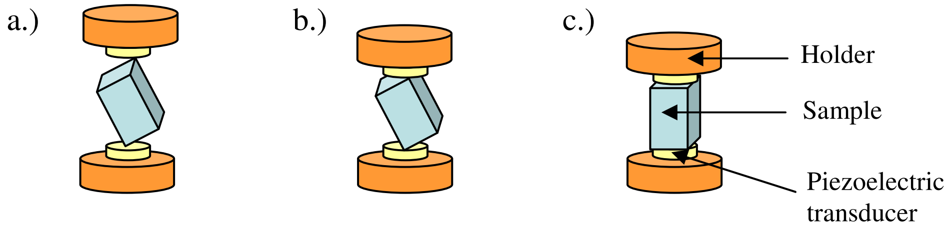

Figure 3.8: a.) Corner mount, b.) edge mount and c.) smallest face mount of the sample in the RUS apparatus. The blue piece is the sample, the yellow pieces are the piezoelectric transducers, and the orange pieces represent the mechanical structure that holds the transducers in place (not to scale).

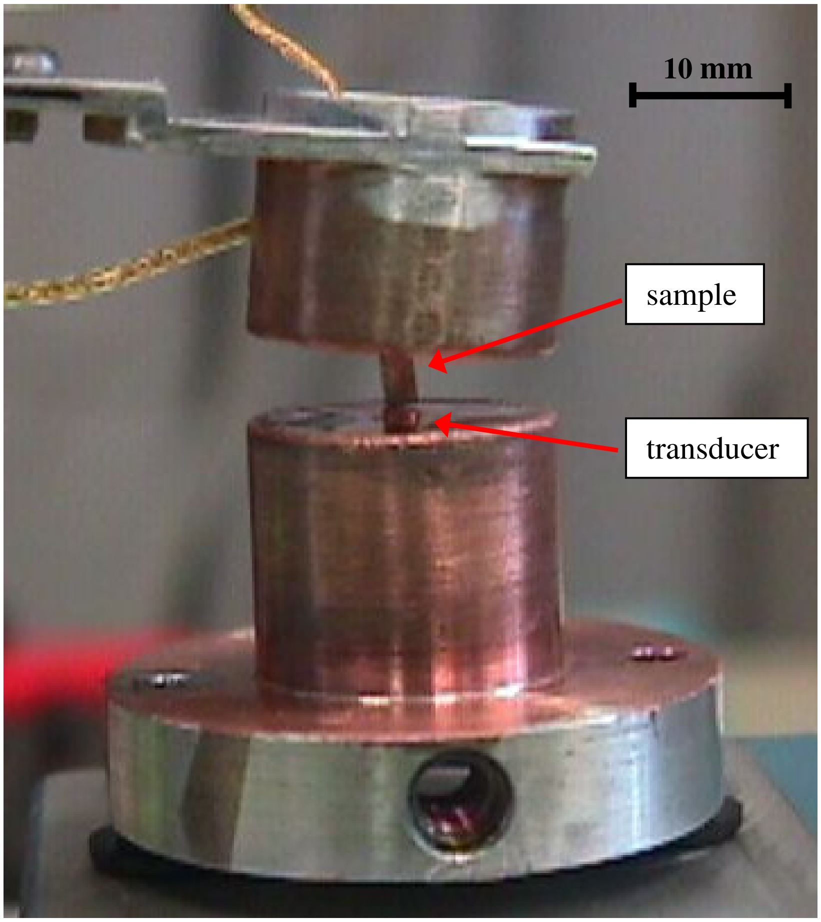

Figure 3.9: Sample mounted in the RUS apparatus.

The RUS apparatus was placed in an electromagnet to enable measurement of the resonance frequencies under a range of magnetic fields. The elastic behavior of Galfenol is known to be related to the orientation of the internal magnetic moments, which are typically randomly oriented under no field and no stress. A high magnetic field or a high, extensional tensile stress will force the magnetic moments to line up with the direction of the field or load [10]. During tensile testing this is observed as the difference in modulus between very low and high stresses (the delta-E effect). For RUS testing, the locations of the resonance frequencies will shift until a saturating field is reached. To track the changes in elastic properties as a function of magnetic field, the field was increased from 0 to 10 kOe, typically in 2 kOe steps. To compare RUS results with tensile results, the measurements that were taken with the saturating field of 10kOe were used.

10 kOe is a higher saturation field than is typically observed for Galfenol samples. This is due to the parallelepiped shape of the RUS samples, which has a high demagnetization factor. An algorithm has been developed by Restorff based on research by Joseph and Schlomann [28] to predict the demagnetization factor using the sample geometry. From this, the demagnetization factor is predicted to be 0.5452.

The demagnetization factor can also be calculated using several measured parameters [10]:

$$N_d = \frac{H_{ext} - H_{eff}}{M_{sat}} \tag{3.10}$$

Here, H_{ext} is the external field which was measured to be 10 kOe, H_{eff} is the effective magnetic field and M_{sat} is the saturation magnetization. Using typical values for Galfenol of H_{eff} = 100 Oe and M_{sat} = 1500 kA/m [10], the demagnetization factor is calculated to be 0.5252. This agreement shows that based on the demagnetization factor, a saturating field of around 10 kOe is to be expected for these samples.

Figure 3.10 shows some sample output figures from the RUS equipment. The x-axis is frequency, and the y-axis is voltage. A peak in voltage occurs at each of the resonance frequencies. Figure 3.10 shows how the output signal changes with the delta-E effect. Figure 3.10a shows a saturating field of 10 kOe, 3.10b is 4 kOe and 3.10c is 0 kOe. As the field decreases, the peaks become less defined and in some cases become completely hidden.

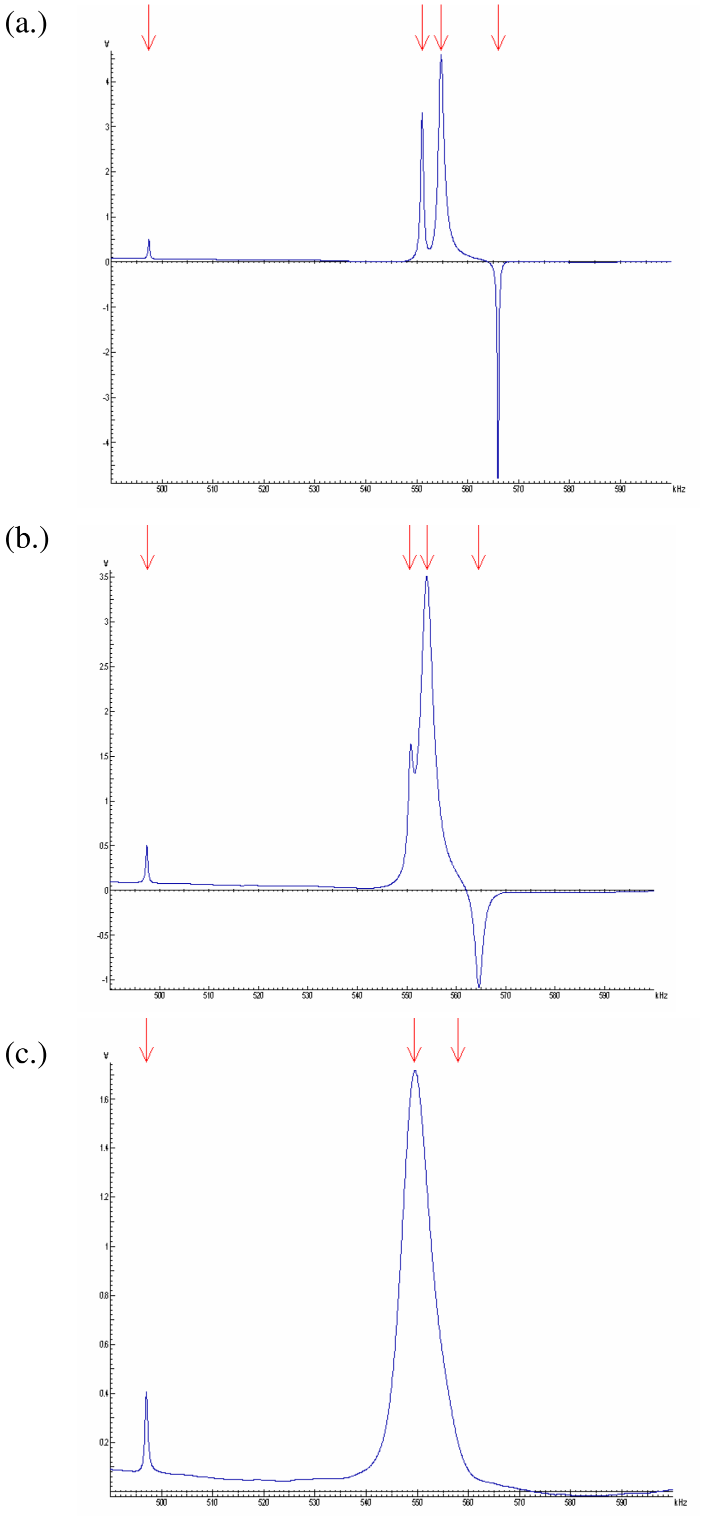

Figure 3.10: Voltage vs. frequency for an $Fe_{82.5}Ga_{17.5}$ sample at (a.) 10 kOe, (b.) 4 kOe and (c.) 0 kOe.

3.4.2 RUS output

The algorithm used to analyze the RUS data takes in the resonance frequencies, sample dimensions and mass, and calculates the three independent elastic constants for single crystal Fe-Ga; c_{11}, c_{12}, and c_{44}. These values can be used to calculate other parameters of interest, such as $c' = ½(c_{11}-c_{12})$, and the anisotropy parameter, $A=c_{44}/c'$. It also provides information on the error in each of the predicted elastic constants.

The anisotropy parameter is of special interest in this study because of its link to the auxetic behavior of a material. Jain and Verma [5] were able to show theoretically that if the anisotropy parameter is above 2 for a material, it may demonstrate auxetic behavior, and if it is above 3 the material will be auxetic. In addition, preliminary examination of published data suggests a trend between increasing anisotropy parameter and increasingly auxetic behavior. Since RUS does not provide a direct measurement of the Poisson's ratio, the anisotropy parameter will be examined in the results of this chapter as a way to predict any auxetic behavior.

3.5 Results and Discussion

Three Fe-Ga samples were obtained with compositions of 17.5, 20.4 and 21.1 atomic % Ga. Each sample was mounted and analyzed three separate times since the positioning of the sample can affect how clearly each resonance frequency is seen. The results of the analysis are presented for each composition under a saturating field. In addition, the elastic properties as a function of the applied field are provided.

3.5.1 Results

The algorithm used to analyze the RUS data calculates the three independent elastic stiffness constants for single crystal Fe-Ga; c_{11}, c_{12}, and c_{44}. These values can be used to calculate other parameters of interest, such as the shear modulus c', and the anisotropy parameter, A. Table 3.1 shows the average values of the elastic constants at a saturating field of 10 kOe. The comparison between these results and the results of the tensile testing is provided in Chapter 4.

Table 3.1: Elastic constants of Fe-Ga samples in a 10kOe saturating field.

at % Ga	**c_{11} (GPa)**	**c_{12} (GPa)**	**c' (GPa)**	**c_{44} (GPa)**	**A**
17.5	192.4	143.6	24.5	121.3	5.0
20.4	182.3	144.8	18.7	120.0	6.4
21.1	150.5	118.9	15.8	123.1	7.8

In general, although there is no apparent trend in the values of c_{12}, c' clearly decreases as the gallium content increases. Also, the anisotropy parameter increases with composition. It is believed that these two trends play a significant role in determining the extent of auxetic behavior exhibited by a material [16].

For each test, the RUS algorithm calculates the error in c_{11}, c_{12}, and c_{44}. In general, taking into account that each sample was tested three times, the typical deviation in c_{11} was 2%, c_{12} was 2%, and c_{44} was under 1% [29]. Error propagation can be used to predict that the error in c' and A is around 1%. The algorithm calculates c' and then uses that to find c_{11} and c_{12}, which is why the error in c' is lower than in c_{11} and c_{12}. The algorithm also calculates an overall RMS error that takes into account the agreement of each set of measured and fitted resonance frequencies. It was typically 0.3% for these samples. Table 3.2 gives the relative errors for each of the parameters and each of the samples.

Table 3.2: Relative error for each of the values in Table 3.1.

at% Ga	**Overall RMS error**	$\mathbf{c_{11}}$	$\mathbf{c_{12}}$	$\mathbf{c'}$	$\mathbf{c_{44}}$	**A**
17.5	0.2561%	1.16%	1.58%	0.72%	0.13%	0.73%
20.4	0.3729%	2.15%	2.73%	1.43%	0.20%	1.44%
21.1	0.3499%	1.90%	2.41%	1.36%	0.20%	1.38%

In addition to examining the elastic constants, the resonance frequencies of each sample were also measured. This can be of use to material scientists seeking a more fundamental-level understanding of the material, since specific frequencies can correspond to specific phenomena. The measured resonance frequencies and the relevant supporting information for all of the Fe-Ga samples is presented in detail in Appendix B.

3.5.2 Relationship of elastic constants and applied field

The values of the elastic constants are dependent on the arrangement of the magnetic moments inside the sample. Therefore, they are dependent on the strength of the applied field. To determine the amount of change in each constant, the RUS analysis was carried out at various magnetic fields, typically starting from 10 kOe and decreasing to 0 kOe in steps of 2 kOe. In general, c_{11} and c_{12} showed a larger dependence on field than c′, c_{44} or *A*. The results for the three Fe-Ga samples are presented in Figures 3.11-3.15. Unfortunately, at 0 kOe not enough resonance frequencies were measurable in the 20.4% sample, so the data is only presented from 2 to 10 kOe.

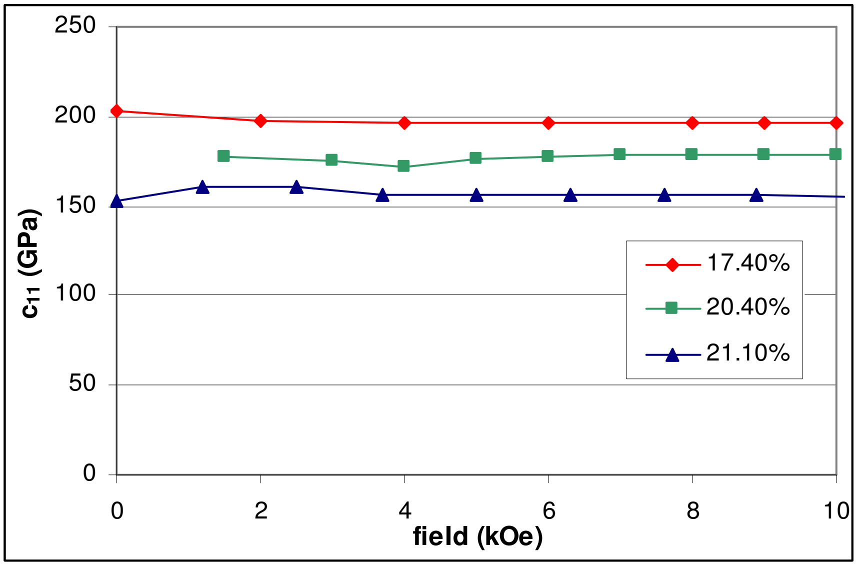

Figure 3.11: Dependence of c_{11} on applied magnetic field.

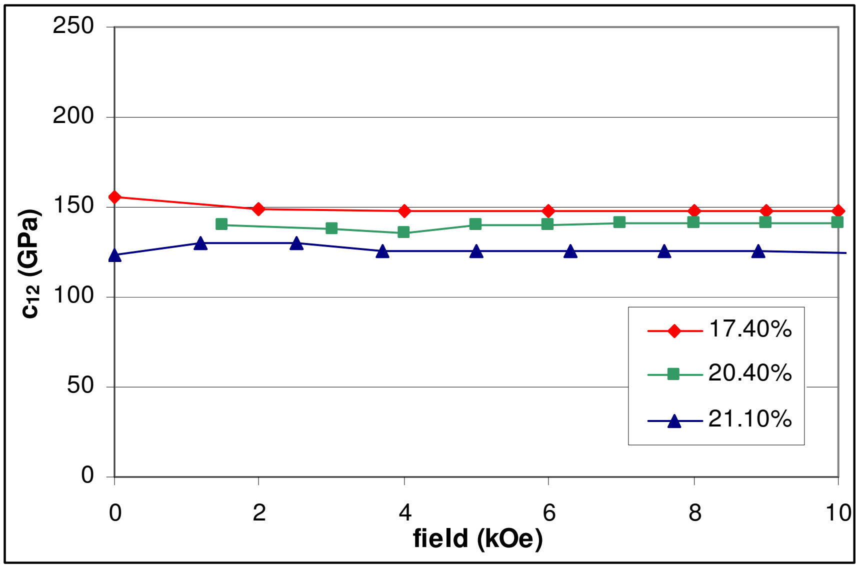

Figure 3.12: Dependence of c_{12} on applied magnetic field.

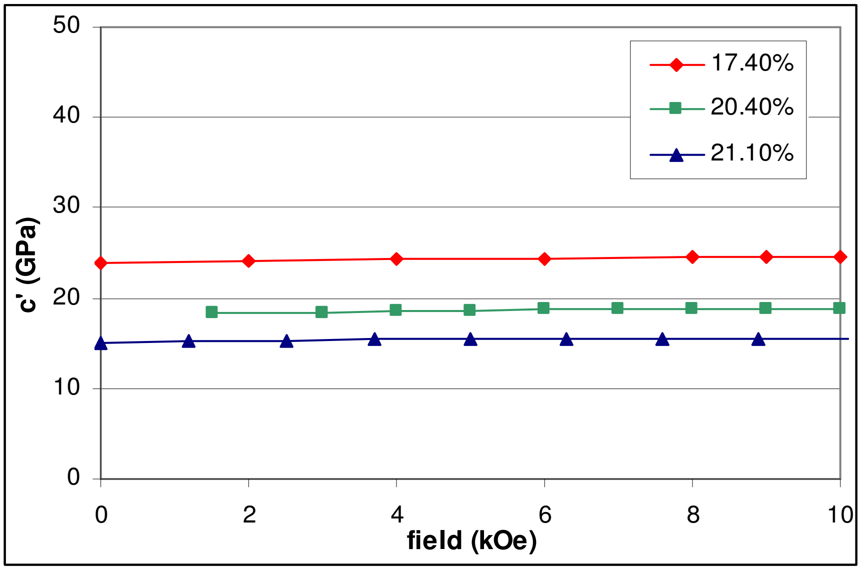

Figure 3.13: Dependence of c′ on applied magnetic field.

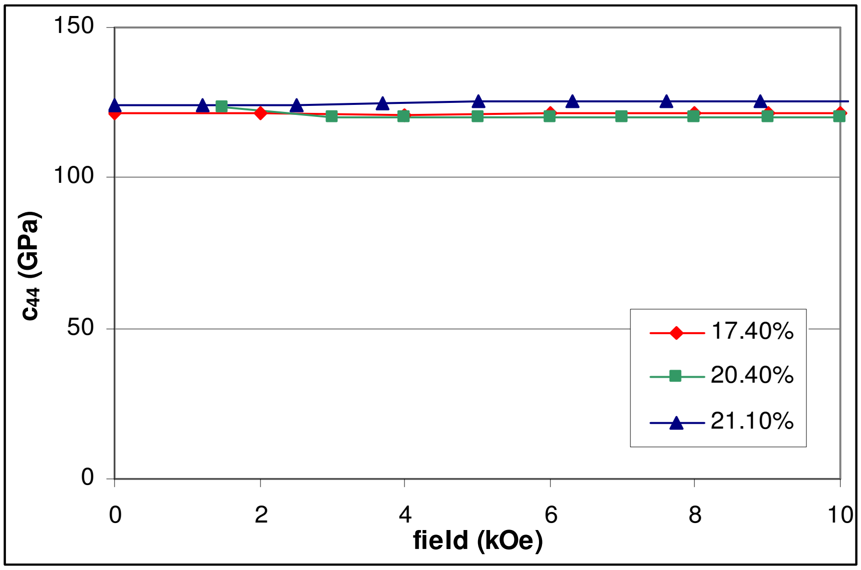

Figure 3.14: Dependence of c_{44} on applied magnetic field.

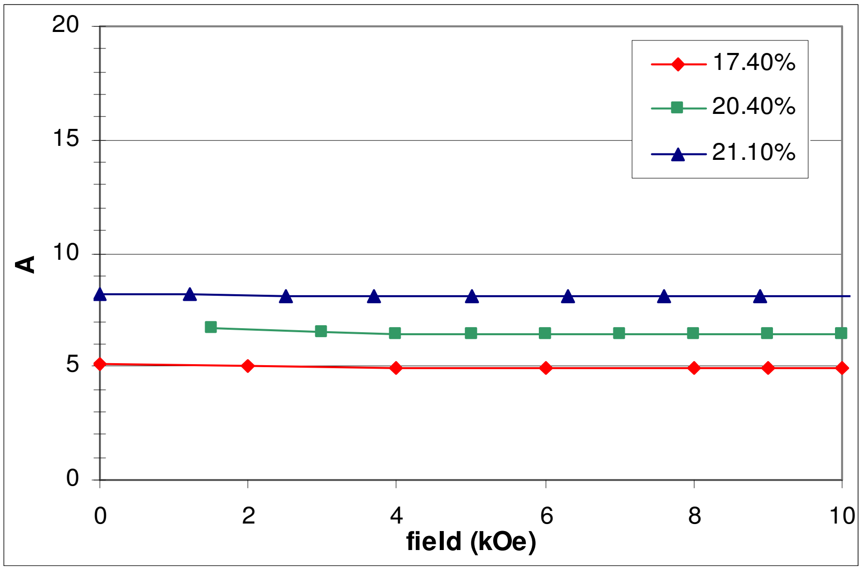

Figure 3.15: Dependence of A on applied magnetic field.

3.5.3 Error analysis

The accuracy of the RUS measurements depends on the quality of the sample. It is important that all the angles of the parallelepiped be as close to 90 degrees as possible. It is also important that the sample sides be aligned along the [100], [010] and [001] directions. The algorithm assumes that the sample is perfect in those respects, so therefore any deviation from that will reduce the accuracy of the results [27]. Since the samples in this study were cut from the tensile samples and were not specifically made for this application, some variation was inevitable. However, care was taken to give the samples right angles and the crystallographic orientations were measured to be under 2 degrees off from the proper directions. The measured errors were small enough to be considered acceptable for this study.

3.6 Conclusions

RUS is a very useful technique for examining the elastic behavior of single crystal Galfenol. It was used here to accurately measure the individual elastic constants, and to track their dependence on field and alloy composition. It showed that c' and A are closely related to the composition. This technique provided a more thorough understanding of the elastic properties.

Chapter 4: Comparison of Tensile Testing, Resonant Ultrasound Spectroscopy and Theoretical Predictions

In this chapter, the results of the tensile testing are compared with the results of the RUS testing and with model predictions. The two experimental investigations directly measured different sets of elastic properties; the tensile testing provided the engineering elastic constants (Young's moduli and Poisson's ratios) and the RUS testing measured the individual elastic stiffness constants (c_{11}, c_{12} and c_{44}). Fortunately, these two sets of information are directly related. This chapter therefore starts with the derivation of the relationships between the two sets of elastic constants. It then provides the direct comparison between the two sets of results, and discusses the comparison including the effects of errors and error propagation. The final section is a comparison of the results that were experimentally obtained through tensile testing and RUS with the results of a theoretical model.

4.1 Relationship Between the Elastic Parameters

As discussed in Chapter 1, Hooke's Law can be used to describe the relationship between stress and strain in a cubic material, where the stress is related to the strain via the stiffness matrix [14]:

$$\begin{bmatrix} \sigma_{11} \\ \sigma_{22} \\ \sigma_{33} \\ \tau_{23} \\ \tau_{13} \\ \tau_{12} \end{bmatrix} = \begin{bmatrix} c_{11} & c_{12} & c_{12} & 0 & 0 & 0 \\ c_{12} & c_{11} & c_{12} & 0 & 0 & 0 \\ c_{12} & c_{12} & c_{11} & 0 & 0 & 0 \\ 0 & 0 & 0 & c_{44} & 0 & 0 \\ 0 & 0 & 0 & 0 & c_{44} & 0 \\ 0 & 0 & 0 & 0 & 0 & c_{44} \end{bmatrix} \begin{bmatrix} \varepsilon_{11} \\ \varepsilon_{22} \\ \varepsilon_{33} \\ \gamma_{23} \\ \gamma_{13} \\ \gamma_{12} \end{bmatrix} \tag{4.1}$$

This relationship can be inverted to write the strain in terms of the stress via the compliance matrix:

$$\begin{bmatrix} \varepsilon_{x} \\ \varepsilon_{y} \\ \varepsilon_{z} \\ \gamma_{yz} \\ \gamma_{xz} \\ \gamma_{xy} \end{bmatrix} = \begin{bmatrix} S_{11} & S_{12} & S_{12} & 0 & 0 & 0 \\ S_{12} & S_{11} & S_{12} & 0 & 0 & 0 \\ S_{12} & S_{12} & S_{11} & 0 & 0 & 0 \\ 0 & 0 & 0 & S_{44} & 0 & 0 \\ 0 & 0 & 0 & 0 & S_{44} & 0 \\ 0 & 0 & 0 & 0 & 0 & S_{44} \end{bmatrix} \begin{bmatrix} \sigma_{x} \\ \sigma_{y} \\ \sigma_{z} \\ \tau_{yz} \\ \tau_{xz} \\ \tau_{xy} \end{bmatrix} \tag{4.2}$$

In this section, x-y-z subscripts will be used on the strain and stress terms to avoid confusion with the numerical subscripts on the compliance and stiffness constants and the Miller index subscripts.

The compliance matrix is the inverse of the stiffness matrix, and its individual terms can be written out in terms of the individual elastic stiffnesses:

$$S_{11} = \frac{c_{11} + c_{12}}{(c_{11} - c_{12})(c_{11} + 2c_{12})} \tag{4.3}$$

$$S_{12} = \frac{-c_{12}}{(c_{11} - c_{12})(c_{11} + 2c_{12})} \tag{4.4}$$

$$S_{44} = \frac{1}{c_{44}} \tag{4.5}$$

Since the main goal of this chapter is to compare the results of the RUS tests to the results of the tensile tests, this section will focus on defining the engineering elastic properties in terms of the individual elastic stiffnesses. This enables calculation of the Young's moduli and Poisson's ratios from the direct measurements of the RUS analysis.

4.1.1 Derivation of Young's modulus

The Young's modulus in an arbitrary direction [hkl] can be calculated using the following equation [15]:

$$\frac{1}{E_{[hkl]}} = S_{11} - 2\left(S_{11} - S_{12} - \frac{1}{2}S_{44}\right)\left(\alpha^2\beta^2 + \alpha^2\gamma^2 + \beta^2\gamma^2\right) \tag{4.6}$$

where α,β,γ are the direction cosines of the [hkl] direction with respect to [100], [010] and [001]. For the Young's modulus in the [100] direction, α is 1 and β and γ are 0, and for the Young's modulus in the [110] direction, α and β are *cos*(45°) and γ is 0, as shown in Figure 4.1.

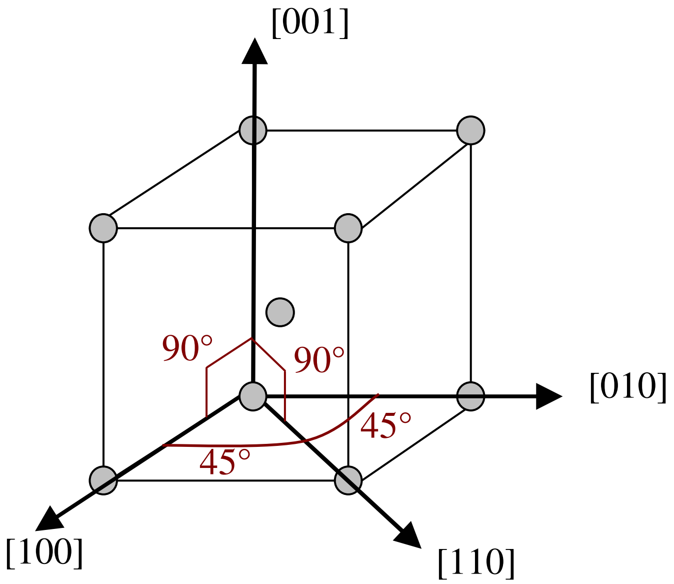

Figure 4.1: Relevant axes and angles for the derivation of $E_{[100]}$ and $E_{[110]}$.

After evaluating Equation 4.6, this gives:

$$E_{[100]} = \frac{c_{11}R}{c_{11} + c_{12}} \tag{4.7}$$

$$E_{[110]} = \frac{4c_{44}R}{R + 2c_{44}} \tag{4.8}$$

$$\text{where } R = \frac{1}{c_{11}}(c_{11} - c_{12})(c_{11} + 2c_{12}) \tag{4.9}$$

4.1.2 Derivation of Poisson's ratio

The Poisson's ratio equations can also be written in terms of the individual elastic stiffness constants. For the derivation of $\nu_{[010]}$, the [100] direction (the direction of the applied load) is defined as the x axis and [010] is defined as the y axis as illustrated in Figure 4.2.

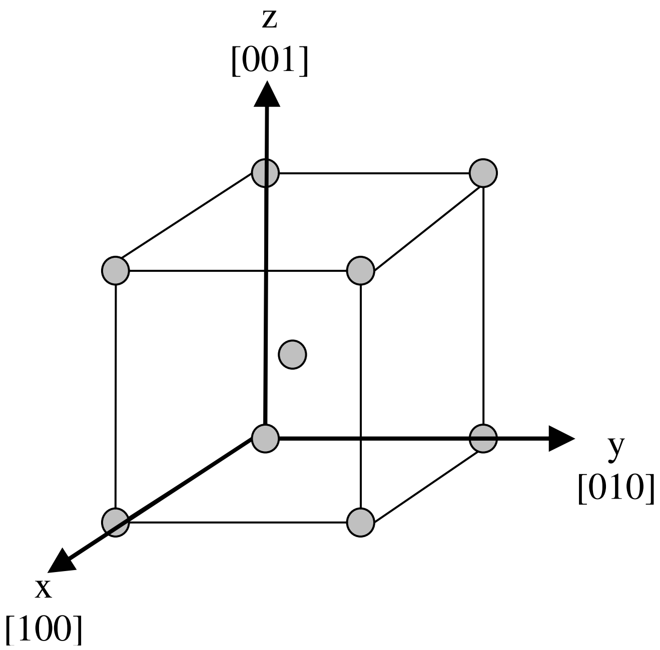

Figure 4.2: Axis definition for the derivation of ν[010]. The x axis is the [100] direction, and the y axis is the [010] direction.

To calculate $\nu_{[010]}$, start from the three dimensional strain-stress relationship as defined in Equation 4.2. In this case, all stresses other than σ_x are defined to be zero. This represents the load that is applied along the [100] direction during tensile testing.

Poisson's ratio for this example is defined as:

$$\nu_{[010]} = \frac{-\varepsilon_y}{\varepsilon_x} \tag{4.10}$$

Both ε_x and ε_y can be written out using Equation 4.2 and then substituted into Equation 4.10:

$$\nu_{[010]} = \frac{-S_{12}\sigma_x}{S_{11}\sigma_x} \tag{4.11}$$

Using Equations 4.3 and 4.4, $\nu_{[010]}$ can be rewritten in terms of c_{11} and c_{12}:

$$\nu_{[010]} = \frac{c_{12}}{c_{11} + c_{12}} \tag{4.12}$$

It is interesting to note that both $E_{[100]}$ and $\nu_{[010]}$ are independent of c_{44}.

Calculating $\nu_{[1\,\bar{1}0]}$ involves a similar process, however now the coordinate system is rotated 45° about the z axis. This is shown in Figure 4.3.

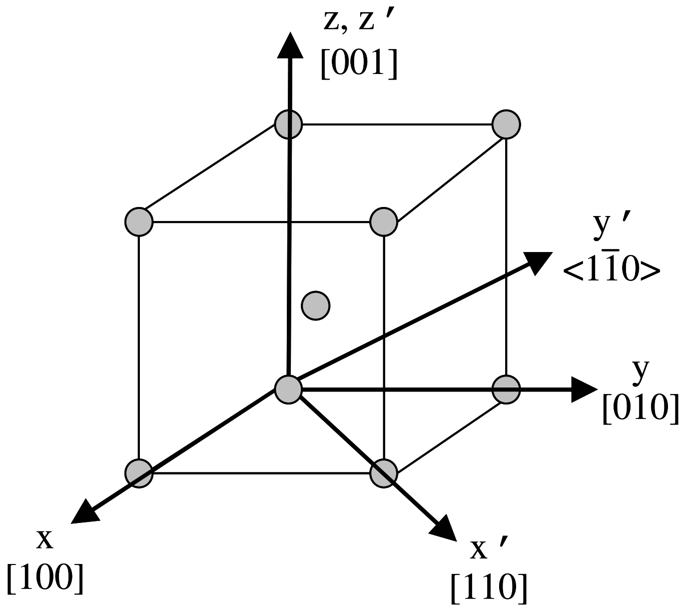

Figure 4.3: Axis definition for the derivation of $\nu[1\,\bar{1}0]$. The x′ axis is the [110] direction, and the y′ axis is the $<1\,\bar{1}0>$ direction.

To transform a stress P applied along the x′ axis into x-y-z coordinates, a transformation matrix α is applied [30]:

$$\sigma = \alpha^T \sigma' \alpha \tag{4.13}$$

$$\alpha = \begin{bmatrix} \cos 45° & \sin 45° & 0 \\ -\sin 45° & \cos 45° & 0 \\ 0 & 0 & 0 \end{bmatrix} \tag{4.14}$$

$$\sigma' = \begin{bmatrix} P & 0 & 0 \\ 0 & 0 & 0 \\ 0 & 0 & 0 \end{bmatrix} \tag{4.15}$$

Solving Equation 4.13 gives the new σ matrix in x-y-z coordinates:

$$\sigma = \begin{bmatrix} \tfrac{1}{2}P & \tfrac{1}{2}P & 0 \\ \tfrac{1}{2}P & \tfrac{1}{2}P & 0 \\ 0 & 0 & 0 \end{bmatrix} \tag{4.16}$$

Taking the σ matrix and plugging it into Equation 4.2 generates the vector of strains:

$$\begin{bmatrix} \varepsilon_x \\ \varepsilon_y \\ \varepsilon_z \\ \gamma_{yz} \\ \gamma_{xz} \\ \gamma_{xy} \end{bmatrix} = \begin{bmatrix} \varepsilon_x \\ \varepsilon_y \\ \varepsilon_z \\ 2\varepsilon_{yz} \\ 2\varepsilon_{xz} \\ 2\varepsilon_{xy} \end{bmatrix} = \begin{bmatrix} S_{11}\sigma_x + S_{12}\sigma_y \\ S_{12}\sigma_x + S_{11}\sigma_y \\ 0 \\ 0 \\ 0 \\ S_{44}\tau_{xy} \end{bmatrix} \tag{4.17}$$

Using Equation 4.16, the strain vector can be written in terms of the applied stress *P*:

$$\begin{bmatrix} \varepsilon_x \\ \varepsilon_y \\ \varepsilon_z \\ \varepsilon_{yz} \\ \varepsilon_{xz} \\ \varepsilon_{xy} \end{bmatrix} = \begin{bmatrix} 0.5P(S_{11}+S_{12}) \\ 0.5P(S_{11}+S_{12}) \\ 0 \\ 0 \\ 0 \\ 0.25P(S_{44}) \end{bmatrix} \tag{4.18}$$

In order to calculate $\nu_{[1\bar{1}0]}$, the strain vector must be transformed into the x′-y′-z′ coordinate system.

$$\nu_{[1\bar{1}0]} = \frac{-\varepsilon_{y'}}{\varepsilon_{x'}} \tag{4.19}$$

The transformation is accomplished through the following equation:

$$\varepsilon' = \alpha\varepsilon\alpha^T \tag{4.20}$$

where α is the same as in Equation 4.14.

From solving 4.20, $\nu_{[1\bar{1}0]}$ can be written in terms of the elastic compliances:

$$\nu_{[1\bar{1}0]} = \frac{-\varepsilon_{y'}}{\varepsilon_{x'}} = \frac{-0.5P*S_{11} - 0.5P*S_{12} + 0.25P*S_{44}}{0.5P*S_{11} + 0.5P*S_{12} + 0.25P*S_{44}} = \frac{-S_{11} - S_{12} + 0.5S_{44}}{S_{11} + S_{12} + 0.5S_{44}} \tag{4.21}$$

Using Equations 4.3 through 4.5, $\nu_{[1\bar{1}0]}$ can finally be written in terms of the elastic stiffnesses:

$$\nu_{[1\bar{1}0]} = \frac{c_{11} + c_{12}\left(1 - \frac{2c_{12}}{c_{11}}\right) - 2c_{44}}{c_{11} + c_{12}\left(1 - \frac{2c_{12}}{c_{11}}\right) + 2c_{44}} \tag{4.22}$$

The equations for $E_{[100]}$, $E_{[110]}$, $\nu_{[010]}$ and $\nu_{[1\bar{1}0]}$ will all be used in Section 4.2 to gain further information from the results of the RUS testing.

4.1.3 Elastic stiffnesses in terms of the engineering elastic properties

From the results of the previous two subsections, it is also possible to write the elastic stiffnesses in terms of the Young's moduli and Poisson's ratios.

$$c_{11} = \frac{(1-\nu_{[010]})E_{[100]}}{(1+\nu_{[010]})(1-2\nu_{[010]})} \tag{4.23}$$

$$c_{12} = \frac{\nu_{[010]}E_{[100]}}{(1+\nu_{[010]})(1-2\nu_{[010]})} \tag{4.24}$$

$$c_{44} = \frac{RE_{[110]}}{2(2R-E_{[110]})} \tag{4.25}$$

$$c_{44} = \frac{R\nu_{[1\bar{1}0]}-R}{-2-2\nu_{[1\bar{1}0]}} \tag{4.26}$$

In this study, these relations will be used to predict the anisotropy parameter of the samples studied using tensile testing. It is interesting to note that c_{44} can be calculated using either $E_{[110]}$ or $\nu_{[1\bar{1}0]}$, meaning it is not necessary to know both.

4.2 Comparison of Tensile Testing and RUS

4.2.1 Results

The elastic properties of three Galfenol samples were measured using two independent tests; tensile testing and resonant ultrasound spectroscopy. To investigate the two methods further, the results are compared here. Since one of the main goals of this thesis is to aid the engineering of new applications, the focus of this section is calculating the engineering elastic properties from the results of the RUS testing. The results are provided in Table 4.1. The conventional and low-load values from the tensile testing are both included in Table 4.1. The error values represent one standard deviation.

Table 4.1: The engineering elastic properties as predicted from RUS testing and as measured from tensile testing.

at % Ga	**property**	**RUS (calculated)**	**Tensile (measured)**	**Low-load tensile (measured)**
17.5	$E_{[100]}$	69.9 ± 6 GPa	60.5 ± 0.7 GPa	42.0 ± 1 GPa
	$\nu_{[010]}$	0.43 ± 0.01	0.42 ± 0.01	0.46 ± 0.02
	$E_{[110]}$	162 ± 8 GPa	161 ± 8 GPa	105 ± 11 GPa
	$\nu_{[1\bar{1}0]}$	-0.33 ± 0.03	-0.51 ± 0.10	-0.43 ± 0.16
20.4	$E_{[100]}$	54.0 ± 11 GPa	52.9 ± 0.7 GPa	44.1 ± 1 GPa
	$\nu_{[010]}$	0.44 ± 0.01	0.45 ± 0.01	0.33 ± 0.02
	$E_{[110]}$	138 ± 18 GPa	132 ± 8 GPa	116 ± 14 GPa
	$\nu_{[1\bar{1}0]}$	-0.43 ± 0.07	-0.48 ± 0.04	-0.62 ± 0.09
21.1	$E_{[100]}$	45.5 ± 8 GPa	39.5 ± 0.7 GPa	30.6 ± 1 GPa
	$\nu_{[010]}$	0.44 ± 0.01	0.51 ± 0.04	0.51 ± 0.07
	$E_{[110]}$	122 ± 14 GPa	112 ± 7 GPa	114 ± 15 GPa
	$\nu_{[1\bar{1}0]}$	-0.50 ± -0.06	-0.54 ± 0.01	-0.73 ± 0.03

The significant disagreement between the results of the RUS tests and the low-load tensile test analysis validate the assumption that a high magnetic field affects the elastic properties in the same manner as a high extensional tensile load. Consequently, the low-load results will be disregarded for the remainder of this chapter.

The results of RUS and the conventional tensile test analysis are plotted in Figures 4.4 through 4.7. There are calculated error bars for every data point, however, on some of the plots the size of the error bars is smaller than the size of the actual data point.

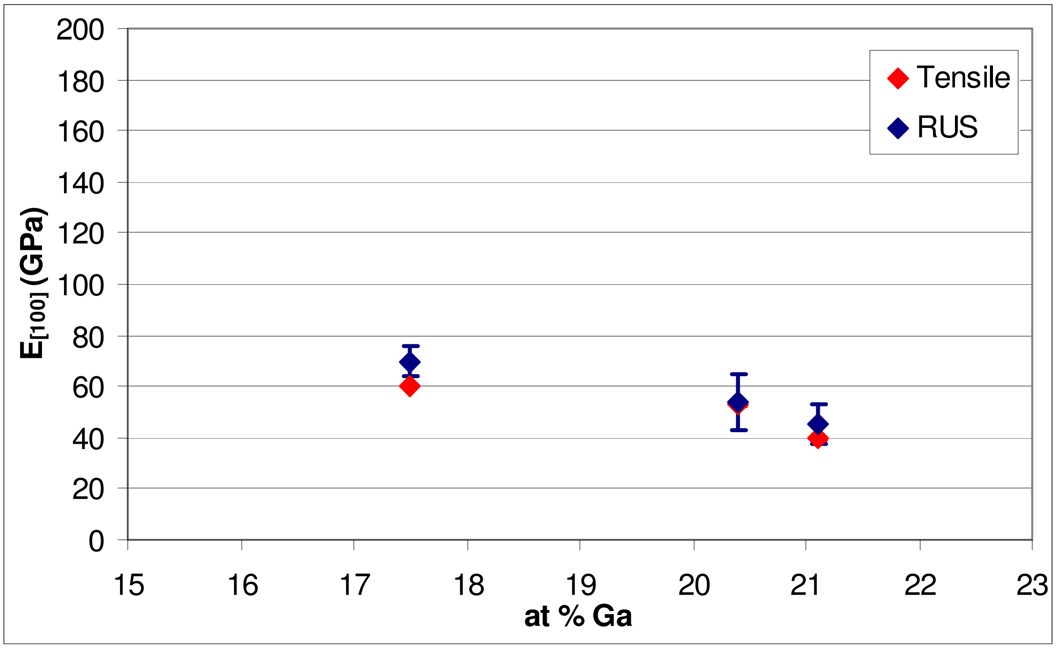

Figure 4.4: $E_{[100]}$ as predicted by RUS and measured through tensile testing.

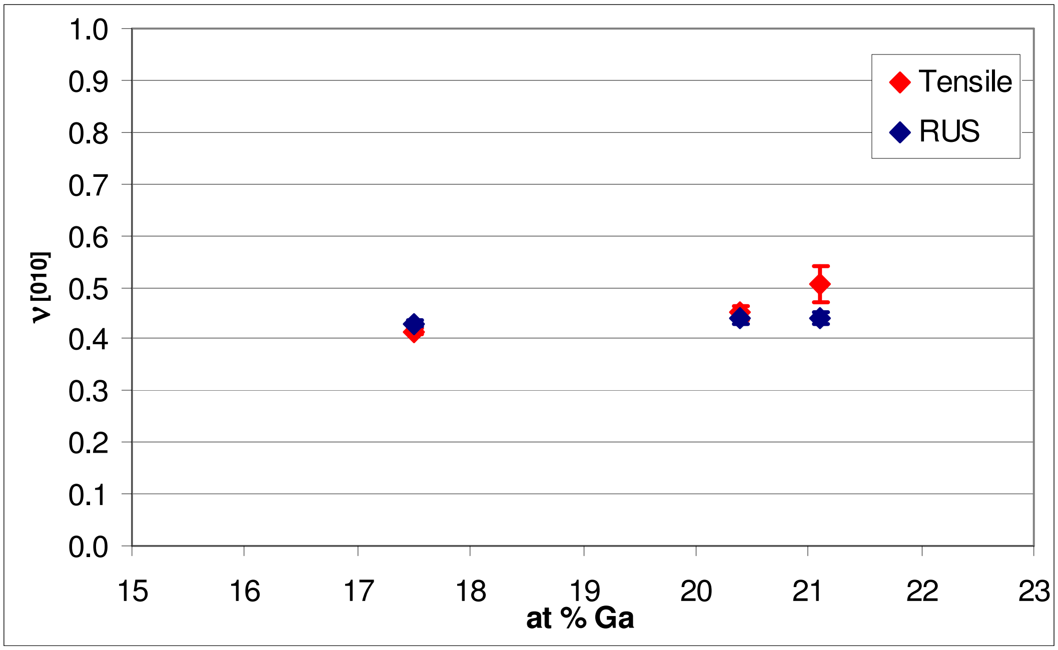

Figure 4.5: $\nu_{[010]}$ as predicted by RUS and measured through tensile testing.

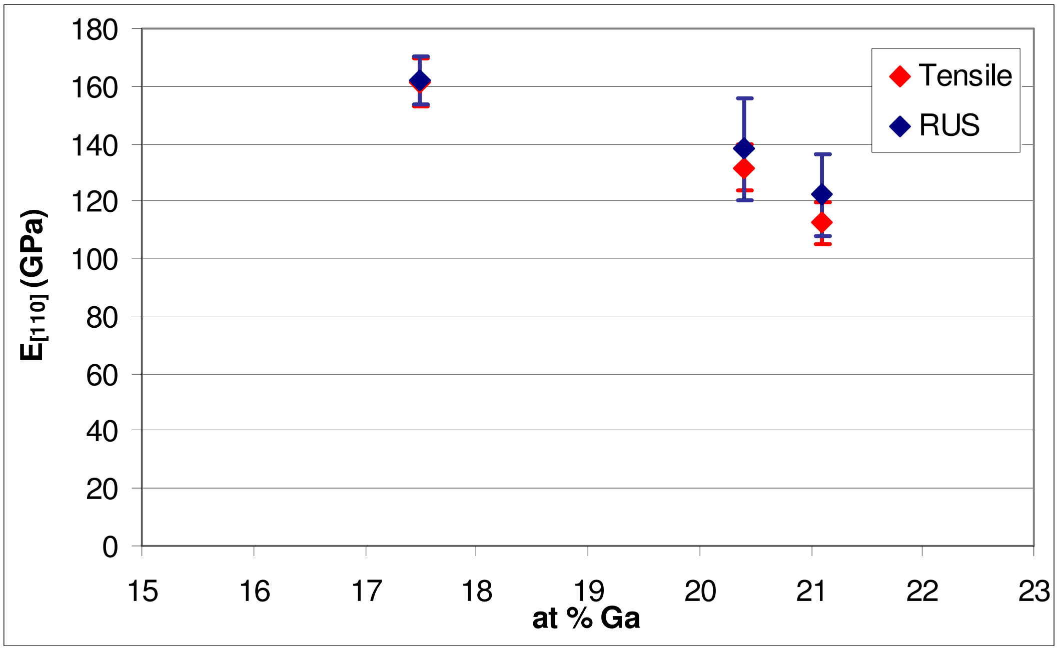

Figure 4.6: $E_{[110]}$ as predicted by RUS and measured through tensile testing.

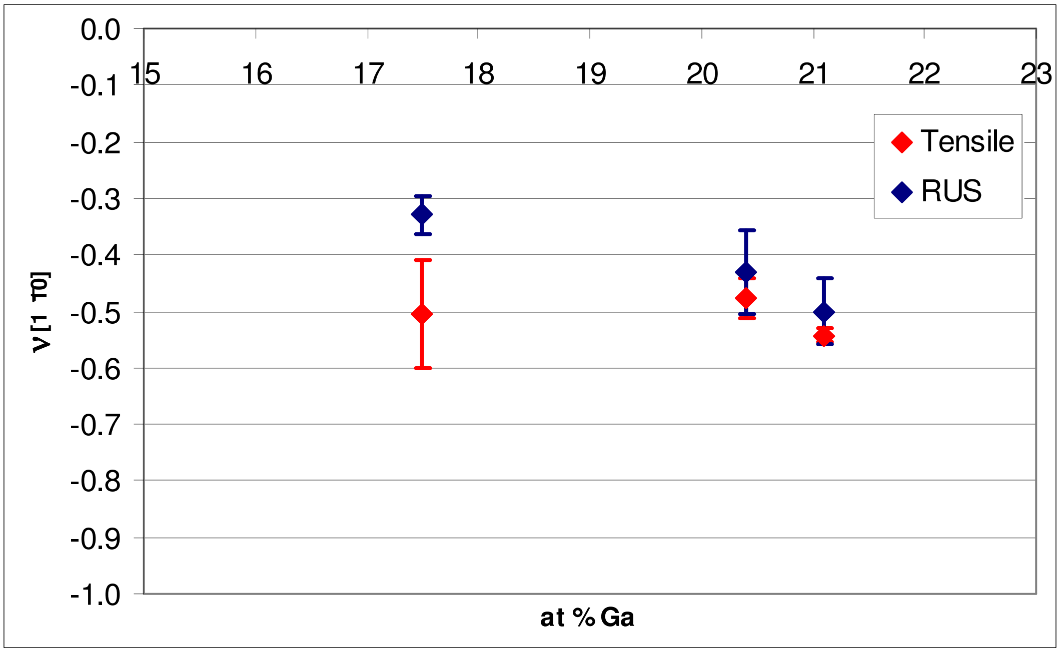

Figure 4.7: $\nu_{[1\ \bar{1}0]}$ as predicted by RUS and measured through tensile testing.

Overall there is very good agreement between the two sets of tests, with only two values that do not match within the error bars. Even the points with relatively small error bars generally show agreement. These results help to validate the effectiveness of both testing methods.

4.2.2 Error propagation

Due to the complicated relationship between the two sets of properties, any errors in the measured quantities can have a very large effect on the property being calculated. It is therefore important to know the errors in each measured quantity and to calculate how the errors will propagate. The RUS algorithm gives an estimated error for c_{11}, c_{12}, and c_{44}, and in general, the error in c_{11} was 2%, c_{12} was 2%, and c_{44} was 0.2% (see Table 3.2 for more details). The engineering elastic properties were therefore calculated by taking into account the entire range of possible values for c_{11}, c_{12} and c_{44}. This was used to determine the error in the RUS predictions of the elastic properties. As seen in Figures 4.4 through 4.7, these error sizes were reasonable, and were generally of the same magnitude as the errors in the tensile testing measurements.

Error propagation becomes more significant when calculating the elastic stiffness constants from the engineering elastic properties. For example, a deviation of 5% in the value of $\nu_{[010]}$ can propagate into a deviation of 41% for the value of c_{11}! Fortunately, the error propagation is only prohibitive when calculating c_{11} and c_{12}; c' and c_{44} can be calculated with reasonable accuracy. This is utilized for calculating the anisotropy parameter in Section 4.2.4.

4.2.3 Additional error analysis

It should be noted that the tensile tests can be assumed to be isothermal, while RUS measurements can be assumed to be adiabatic. A correction factor allows a conversion for the Young's modulus measured from an isothermal test to that measured from an adiabatic test [31]:

$$E_{adiabatic} = \frac{E_{isothermal}}{1 - \frac{E_{isothermal} T \alpha^2}{\rho C_p}} \tag{4.27}$$

where the E's are the Young's moduli, T is the temperature, α is the coefficient of volume thermal expansion, ρ is the density, and C_p is the heat capacity at constant pressure. Using values from the tensile study for the 17.5% Ga sample, $E_{isothermal}$ =

60.5 GPa, T = 298K, and ρ = 7840 kg/m^3, and the published values of α = 11.4 ppm/°C for $Fe_{82.5}Ga_{17.5}$ at room temperature [32] and C_p = 4.730 x 10^{-7}J/kg^2-K [33], the calculated value is $E_{adiabatic}$ = 60.50004 GPa. This is a change of 6x10^{-5} %, which is taken as negligible for this study. Since the heat capacity of Galfenol is unknown, the value for pure iron was used here. This approximation is justified because this heat capacity value would need to decrease by 99% before translating into a 0.1% change in Young's modulus.

4.2.4 Anisotropy

The anisotropy parameter, $A = c_{44}/c'$, is also of interest in this study, because it can be used to predict whether or not a material will have a negative Poisson's ratio. If a material has a value of A that is less than 2 it will not exhibit auxetic behavior, and a material with A greater than 3 will exhibit auxetic behavior. Materials with a value of A in between 2 and 3 could have a positive or negative Poisson's ratio, depending on the ratio of c_{12} to c_{11} [5]. Since its value is of interest and because it can be predicted with more precision than the individual elastic constants, it is presented here. Table 4.2 shows the calculated values of c', c_{44} and A from tensile testing and the measured values from RUS. Since there are two separate equations for calculating c_{44} (Equations 4.25 and 4.26), the c_{44} values presented here are the average of the values calculated using both equations.

Table 4.2: Comparison of anisotropy parameter of Fe-Ga as determined by RUS and tensile testing.

	c′ (GPa)		**c_{44} (GPa)**		**A**	
at.% Ga	**RUS**	**Tensile**	**RUS**	**Tensile**	**RUS**	**Tensile**
17.5	24.5	21.3	121.3	160.7	4.95	7.54
20.4	18.7	18.4	120.0	122.0	6.41	6.64
21.1	15.8	13.1	123.1	113.3	7.81	8.66

There is again good agreement between the RUS data and the tensile testing data. In general though, c′ is lower and the anisotropy parameter is higher for all the tensile testing data. In addition, the c_{44} value for the 17.5% sample is much larger than expected [3], suggesting some portion of the tensile testing data for the 17.5% sample may not be as accurate as it is for the other samples.

4.3 Comparison of Experimental Results with Theoretical Prediction

In addition to comparing the two sets of experimental data with each other, both sets can be compared to a theoretical model. The theoretical model used here was created by Zhang and Wu [16], and it is described in Section 1.6. Zhang and Wu modeled $Fe_{100-x}Ga_x$ (x = 0, 6.25, 12.5, 18.75 and 25) alloys at the atomic level. Using their model, they were able to predict the elastic stiffness constants. These were then used to predict the Young’s moduli and Poisson’s ratios.

The results of the tensile tests on the 12.0%, 18.1% and 25.4% were used as a direct comparison with the results of the model. A summary of the comparison is presented in Tables 4.3 and 4.4. The error bars for the tensile testing represent one standard deviation. There are no error bars available for the predicted data. In general, there is good agreement between the two approaches.

Table 4.3: Comparison of the tensile testing data and the theoretically predicted results, [100] direction.

	$E_{[100]}$ (GPa)		**$\nu_{[010]}$**	
at% Ga	Exp.	Calc.	Exp.	Calc.
11.9	80.0 ± 1.3		0.47 ± 0.02	
12.5		91.4		0.41
18.2	63.5 ± 2.1		0.43 ± 0.02	
18.75		64.7		0.44
25.4	24.4 ± 1.7		0.49 ±0.06	
25.0		22.2		0.48

Table 4.4: Comparison of the tensile testing data and the theoretically predicted results, [110] direction.

	$E_{[110]}$ (GPa)		**$\nu_{[1\bar{1}0]}$**	
at% Ga	Exp.	Calc.	Exp.	Calc.
12.0	167 ± 5		-0.27 ± 0.08	
12.5		185		-0.202
17.9	158 ± 7		-0.46 ± 0.10	
18.75		159		-0.379

25.3	90.5 ± 1.4		-0.66 ± 0.04	
25.0		73		-0.711

To further examine the findings of the model, all available results from the model, tensile testing and RUS can be plotted together for each engineering elastic property. These results are shown in Figures 4.8 through 4.11. The tensile testing data was taken from Chapter 2, the RUS data from Section 4.2, and the theoretical data from the published results [16]. A trend line has been added for the theoretical data.

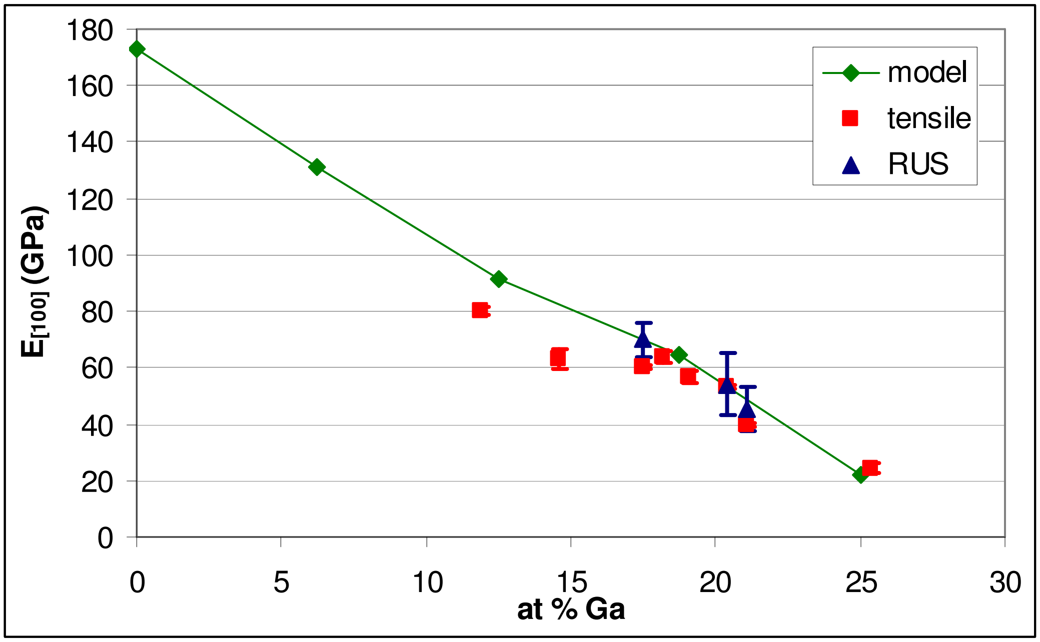

Figure 4.8: $E_{[100]}$ as measured through tensile testing, as calculated using RUS, and as predicted through the model.

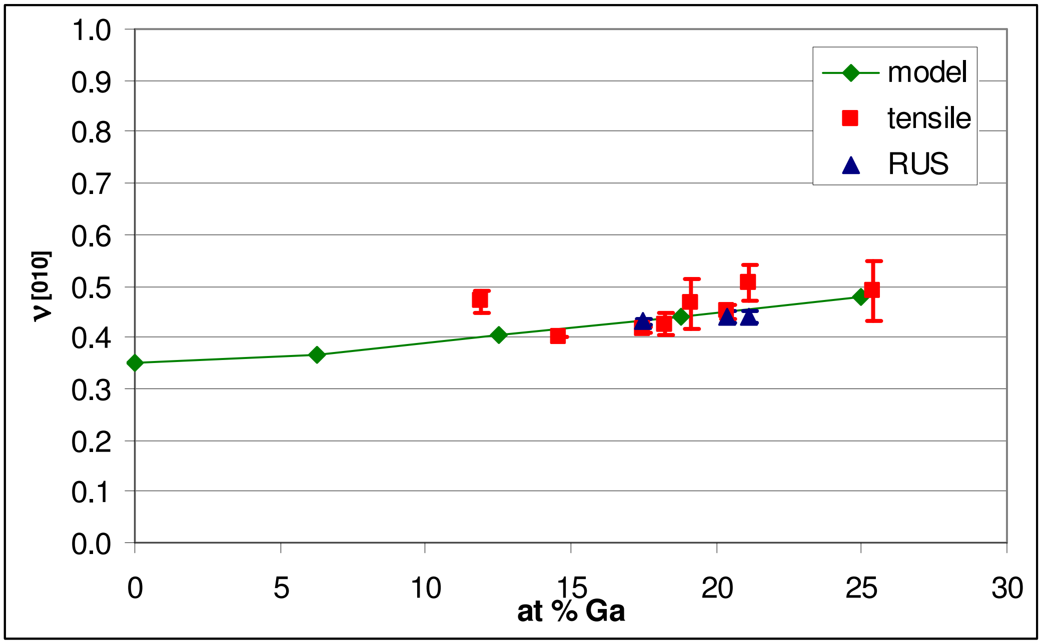

Figure 4.9: $\nu_{[010]}$ as measured through tensile testing, as calculated using RUS, and as predicted through the model.

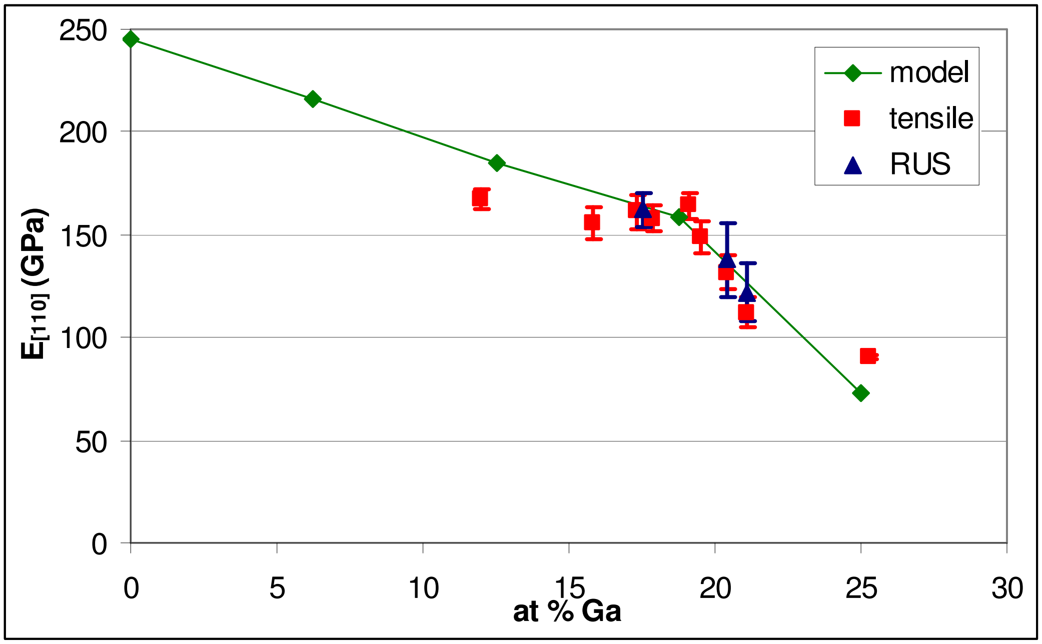

Figure 4.10: $E_{[110]}$ as measured through tensile testing, as calculated using RUS, and as predicted through the model.

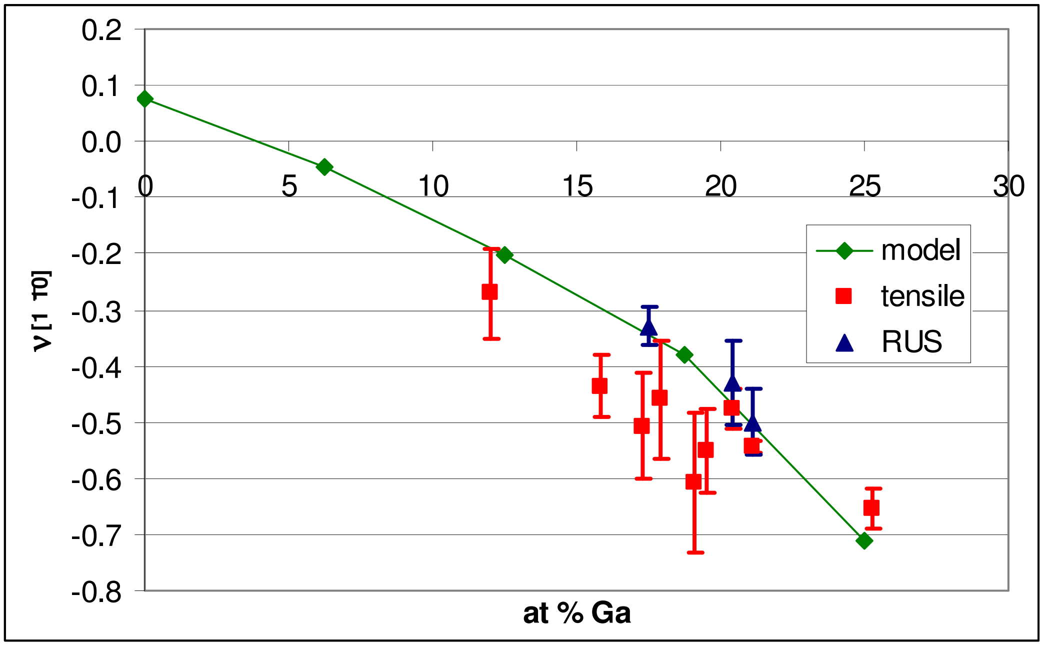

Figure 4.11: $\nu_{[1\,\bar{1}0]}$ as measured through tensile testing, as calculated using RUS, and as predicted through the model.

4.4 Conclusions

Through this chapter, the relationship between elastic stiffness constants and engineering elastic properties was developed. The comparison of the results from the tensile testing and the RUS experiments generally showed good agreement, validating both approaches. In addition, this comparison enabled a more thorough examination of the elastic behavior of each of the three compositions studied here. The comparison between the two sets of experimental data and the theoretical model also generally showed good agreement and added insight into the elastic behavior.

Chapter 5: Fe-Ga + Ternary Additions

RUS testing was also performed on samples consisting of iron and gallium with small amounts of a third element. Researchers have shown that additions of small elements such as carbon, nitrogen and boron can improve the magnetostriction [34,35]. It was therefore of interest to see how these interstitial additions would change the elastic properties, and specifically, if they would increase the anisotropy parameter and the auxetic behavior. This chapter provides the measured elastic stiffnesses from the RUS testing as well as the predicted engineering elastic properties. It also discusses the effects of the ternary additions on both sets of properties.

5.1 RUS Analysis

This section provides the background information for this set of RUS experiments. It describes the samples used, the experimental equipment and the testing procedure.

5.1.1 Fe-Ga-X samples

These samples were all made by Ames Laboratory specifically for use in RUS testing. Because of this, no further orientation analysis or refinishing was necessary. However, these samples were older than the Fe-Ga samples and had been used in previous experiments, and as a result of this, some of the edges and corners on the samples were slightly dulled. The effects of this will be discussed in Section 5.2.

The set of Fe-Ga-X samples consisted of three samples with small amounts of carbon, two with small amounts of boron and two with small amounts of nitrogen. All the samples had between 15 and 20% gallium. They were all single crystal samples that had been slow-cooled after being manufactured. As with the Fe-Ga samples, these were rectangular parallelepipeds, however the Fe-Ga-X samples had a total volume of around 15 mm^2, slightly larger than the Fe-Ga samples. The individual dimensions varied from sample to sample.

5.1.2 Experiment procedure and equipment

The Fe-Ga-X samples were tested using the same equipment and procedure as the Fe-Ga samples. They were tested in an electromagnet that applied magnetic fields ranging from 0 to 10 kOe, and at each field the first 30 resonance frequencies were measured. 10 kOe was high enough to saturate the samples. The samples were all tested three separate times, and were removed from the apparatus in between each test. Using the measured frequencies, the sample dimensions and the sample mass, the RUS algorithm calculated c_{11}, c_{12} and c_{44} at each field for each sample.

5.2 Results

The direct output of the RUS analysis was the elastic stiffness constants for each of the Fe-Ga-X samples. These are presented for a saturating magnetic field in Section 5.2.1. The next subsection describes the field dependence of the elastic stiffnesses. The section concludes with a discussion of the results.

5.2.1 Elastic stiffness constants

Table 5.1 shows the results from the RUS analysis. These results were all taken under a saturating magnetic field of 10 kOe. Each sample was tested three times; the values in Table 5.1 are the averages of the three tests. The typical error in c_{11} and c_{12} was around 2% and the error in c_{44} was below 1%. As before, a conservative estimate for the error in c′ and *A* is 1%. Table 5.2 provides the relative error for each measurement.

Table 5.1: Results of RUS testing on Fe-Ga + interstitial additions.

composition	**c_{11} (GPa)**	**c_{12} (GPa)**	**c′ (GPa)**	**c_{44} (GPa)**	**A**
$Fe_{83.72}$ $Ga_{16.2}$ $C_{0.08}$	198.5	143.7	27.4	122.3	4.5
$Fe_{82.33}$ $Ga_{17.6}$ $C_{0.07}$	174.4	130.0	22.2	121.3	5.5
$Fe_{81.23}$ $Ga_{18.6}$ $C_{0.17}$	190.3	145.3	22.5	124.7	5.6
$Fe_{85.38}$ $Ga_{14.6}$ $B_{0.02}$	198.4	140.2	29.1	124.1	4.3
$Fe_{81.72}$ $Ga_{18.2}$ $B_{0.08}$	215.0	171.8	21.6	123.1	5.7
$Fe_{84.59}$ $Ga_{15.4}$ $N_{0.01}$	198.6	144.3	27.2	121.7	4.5
$Fe_{80.49}$ $Ga_{19.5}$ $N_{0.01}$	173.4	137.7	17.8	125.7	7.0

Table 5.2: Relative error for each of the values in Table 5.1.

composition	**Overall RMS error**	**c_{11}**	**c_{12}**	**c′**	**c_{44}**	**A**
$Fe_{83.72}$ $Ga_{16.2}$ $C_{0.08}$	0.3401%	1.34%	1.89%	0.91%	0.18%	0.92%
$Fe_{82.33}$ $Ga_{17.6}$ $C_{0.07}$	0.3104%	1.32%	1.80%	0.94%	0.15%	0.95%

$Fe_{81.23}\,Ga_{18.6}\,C_{0.17}$	0.3638%	1.85%	2.45%	1.21%	0.19%	1.22%
$Fe_{85.38}\,Ga_{14.6}\,B_{0.02}$	0.3842%	1.44%	2.07%	0.97%	0.21%	0.99%
$Fe_{81.72}\,Ga_{18.2}\,B_{0.08}$	0.3494%	2.17%	2.74%	1.40%	0.20%	1.42%
$Fe_{84.59}\,Ga_{15.4}\,N_{0.01}$	0.3118%	1.68%	2.33%	0.74%	0.21%	0.77%
$Fe_{80.49}\,Ga_{19.5}\,N_{0.01}$	0.2826%	1.42%	1.81%	1.01%	0.15%	1.02%

The errors in the Fe-Ga-X samples are generally of the same magnitude as the Fe-Ga samples, however they were caused by different sources. The Fe-Ga samples had some variance in their orientations; while the Fe-Ga-X samples had imperfections in their geometry (some had slightly rounded edges or corners). Because the geometry errors caused the same magnitude of errors as was observed with the Fe-Ga samples, the extent of the geometry imperfections was considered acceptable for this study.

In addition to measuring the elastic stiffnesses, RUS analysis also provided the resonance frequencies. The first 30 resonance frequencies and the relevant supporting information for each of the Fe-Ga-X samples are provided in Appendix C.

5.2.2 Field dependence

As with the binary Fe-Ga samples, the elastic constants of the Fe-Ga-X samples also show a dependence on the applied magnetic field. Figures 5.1 through 5.5 show the dependence of each elastic constant on the field. Similarly to the Fe-Ga samples, c_{11} and c_{12} show the strongest dependence on the field.

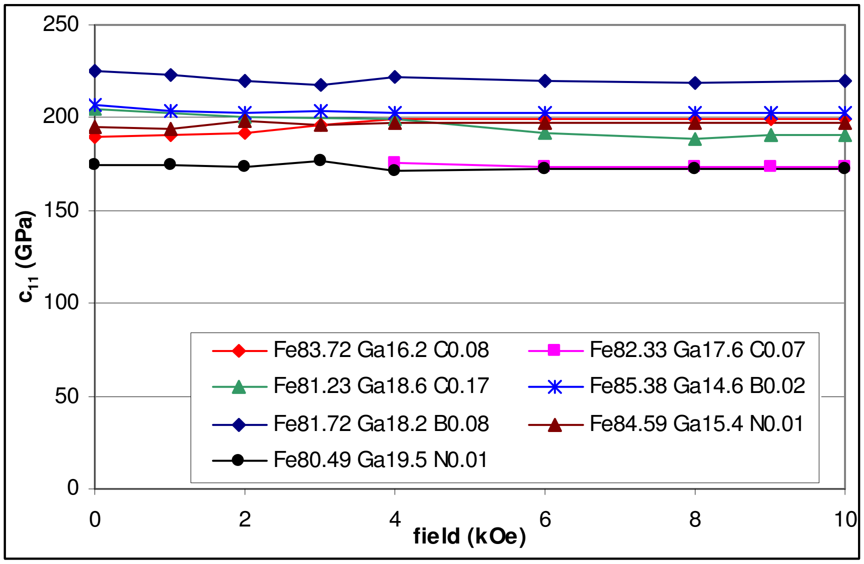

Figure 5.1: Dependence of c_{11} on applied magnetic field.

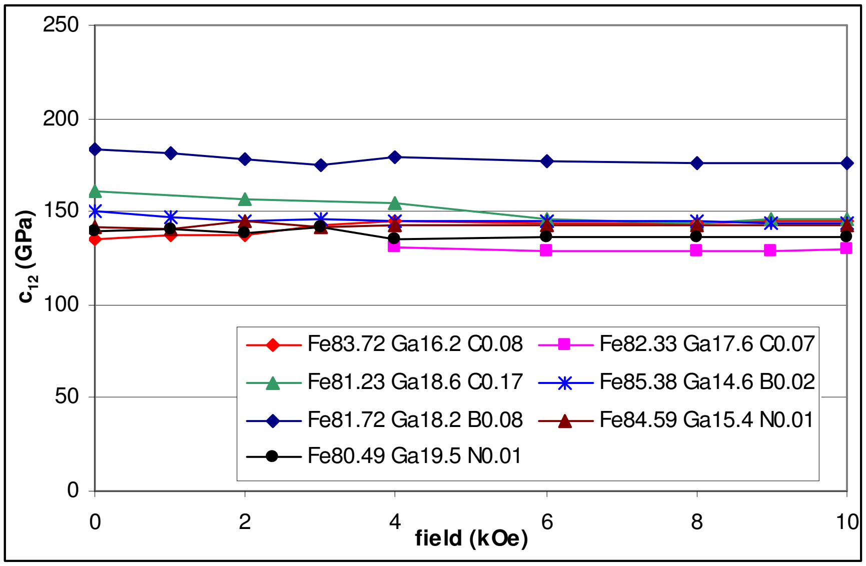

Figure 5.2: Dependence of c_{12} on applied magnetic field.

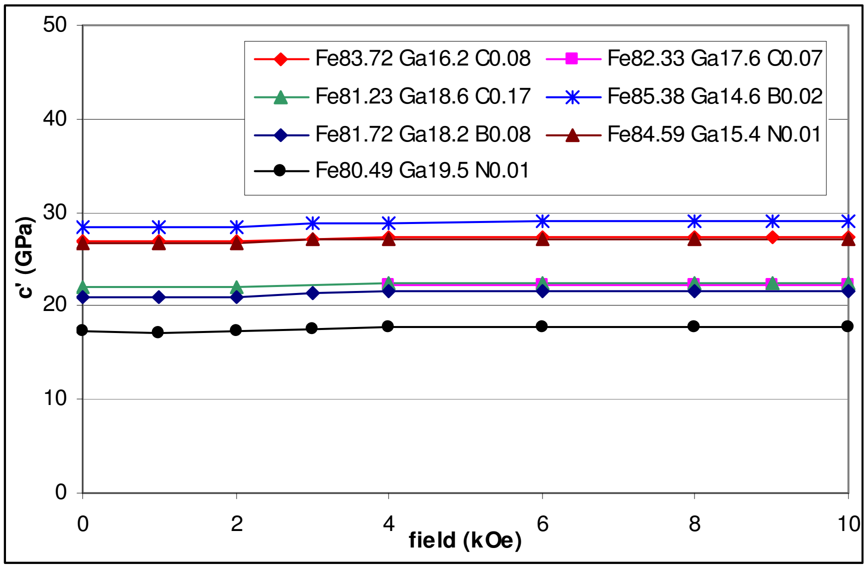

Figure 5.3: Dependence of c′ on applied magnetic field.

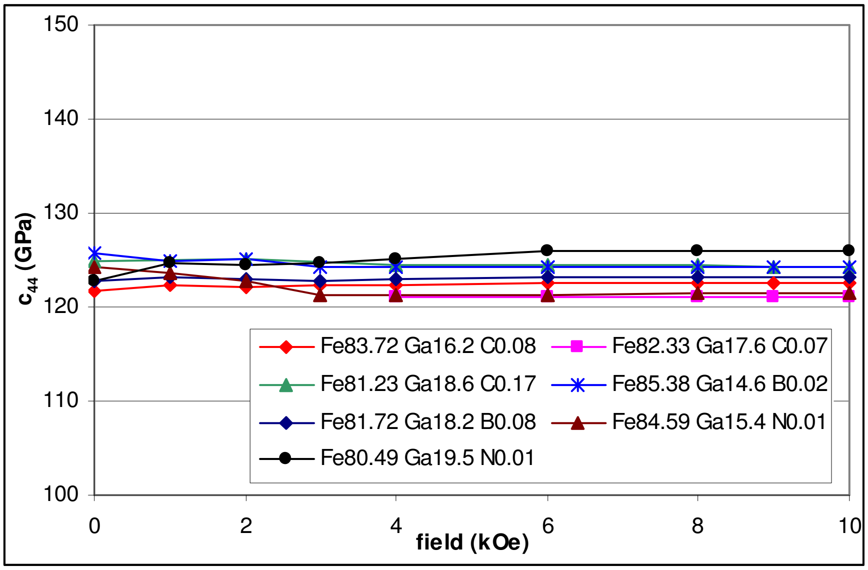

Figure 5.4: Dependence of c_{44} on applied magnetic field.

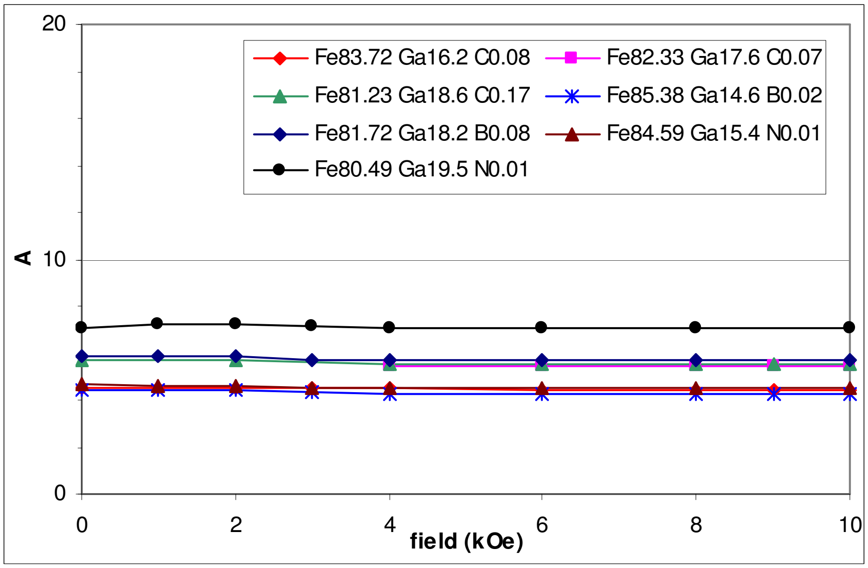

Figure 5.5: Dependence of A on applied magnetic field.

5.2.3 Discussion

By comparing these results to data for binary Fe-Ga alloys, the effects of interstitial additions on the elastic properties and auxetic behavior can be examined. The available relevant data is presented in Table 5.3.

Table 5.3: Relevant elastic constants of binary Fe-Ga alloys. The data for $Fe_{82.5}Ga_{17.5}$ and $Fe_{81.9}Ga_{18.1}$ are from Chapters 3 and 4, respectively.

composition	**c′ (GPa)**	**c_{44} (GPa)**	**A**
$Fe_{82.5}Ga_{17.5}$	24.5	121.3	5.0
$Fe_{81.9}Ga_{18.1}$	22.2	143.2	6.5
$Fe_{81}Ga_{19}$ [3]	16.6	123.9	7.5

The most direct comparison is between the $Fe_{82.33}Ga_{17.6}C_{0.07}$ and $Fe_{82.5}Ga_{17.5}$ samples. This shows that adding carbon to a 17.5% Ga sample increases the anisotropy parameter. This does not appear to be the case when comparing the other relevant samples, where the anisotropy parameter decreases. In Section 5.3, the engineering elastic properties are calculated from the results of the Fe-Ga-X RUS testing, and this analysis also suggests that, in general, the interstitial additions do not help increase the auxeticity.

Huang et al. [34] examined the effects of the addition of interstitial elements on the magnetostriction of Galfenol. They found it is most beneficial in samples with above 18% gallium, and they attribute this to the suppression of the formation of the $D0_3$ phase by the added interstitials. In general, the changes in magnetostriction trends in Galfenol are closely related to the presence of $D0_3$ [11,36]. The findings of this RUS study suggest that the elastic properties, however, are not as closely related to the phase at these compositions.

5.3 Fe-Ga-X Engineering Elastic Properties

The relations developed in Chapter 4 to convert the elastic stiffnesses to engineering elastic properties can also be used to further examine the Fe-Ga-X samples. Using these relations enables a closer examination of how the additions of small interstitials affect the elastic properties, and specifically how they affect the auxetic behavior.

5.3.1 Results

Using the data from Table 5.1 and the equations in Section 4.1, the Fe-Ga-X engineering elastic properties can be predicted. They are presented in Table 5.4. The error bars were again calculated by considering the full range of possible values for c_{11}, c_{12} and c_{44}.

Table 5.4: Fe-Ga-X engineering elastic properties as predicted from the data collected using RUS.

	$E_{[100]}$ (GPa)	$\nu_{[010]}$	$E_{[110]}$ (GPa)	$\nu_{[1\bar{1}0]}$
$Fe_{83.72}Ga_{16.2}C_{0.08}$	77.8 ± 9	0.42 ± 0.01	173 ± 11	-0.30 ± 0.05
$Fe_{82.33}Ga_{17.6}C_{0.07}$	63.4 ± 8	0.43 ± 0.01	152 ± 12	-0.38 ± 0.05
$Fe_{81.23}Ga_{18.6}C_{0.17}$	64.3 ± 12	0.44 ± 0.02	155 ± 17	-0.38 ± 0.07
$Fe_{85.38}Ga_{14.6}B_{0.02}$	82.1 ± 9	0.41 ± 0.01	179 ± 10	-0.28 ± 0.04
$Fe_{81.72}Ga_{18.2}B_{0.08}$	62.3 ± 14	0.45 ± 0.02	152 ± 21	-0.38 ± 0.09
$Fe_{84.59}Ga_{15.4}N_{0.01}$	77.1 ± 9	0.42 ± 0.01	172 ± 11	-0.30 ± 0.05
$Fe_{80.49}Ga_{19.5}N_{0.01}$	51.4 ± 9	0.44 ± 0.01	134 ± 15	-0.47 ± 0.06

In general, the error bars are larger for the engineering elastic properties of the Fe-Ga-X samples than they were for the Fe-Ga samples. This may have arisen because these samples were older than the Fe-Ga samples and some of the edges and corners had become dull from handling and use. Overall though, most of the error bars are reasonable.

5.3.2 Discussion

The engineering elastic properties of the Fe-Ga-X samples can be compared to the engineering elastic properties of binary Fe-Ga samples as measured using tensile testing (see Chapter 2). A summary of the most relevant data is presented in Table 5.5.

Table 5.5: Engineering elastic properties of binary Fe-Ga samples as measured using tensile testing.

	$E_{[100]}$ (GPa)	$\nu_{[010]}$	$E_{[110]}$ (GPa)	$\nu_{[1\bar{1}0]}$
$Fe_{85.4}Ga_{14.6}$	63.2 ± 3	0.40 ± 0.0	–	–
$Fe_{84.2}Ga_{15.8}$	–	–	156 ± 8	-0.44 ± 0.06
$Fe_{82.6}Ga_{17.4}$	60.5 ± 0.7	0.42 ± 0.01	161 ± 8	-0.51 ± 0.10
$Fe_{81.9}Ga_{18.1}$	63.5 ± 2	0.43 ± 0.02	158 ± 7	-0.46 ± 0.10
$Fe_{80.9}Ga_{19.1}$	56.5 ± 2	0.47 ± 0.05	164 ± 6	-0.61 ± 0.12
$Fe_{80.5}Ga_{19.5}$	–	–	149 ± 8	-0.55 ± 0.08

From examining the data in Tables 5.4 and 5.5, it is apparent that interstitial additions can have a significant effect on the elastic properties. This data is shown in Figures 5.6 through 5.9. There is again evidence that the interstitial additions do not improve the auxetic behavior. All of the direct comparisons available show that the additions cause a positive increase in the value of $\nu_{[1\bar{1}0]}$. One interesting change however, is that the $Fe_{80.49}Ga_{19.5}N_{0.01}$ sample has a lower $E_{[110]}$ than the $Fe_{80.5}Ga_{19.5}$ sample, while still demonstrating a significantly negative Poisson's ratio. An application utilizing auxetic behavior would benefit from a low negative Poisson's ratio combined with a low Young's modulus, suggesting that this material could potentially be more useful than a binary Fe-Ga sample.

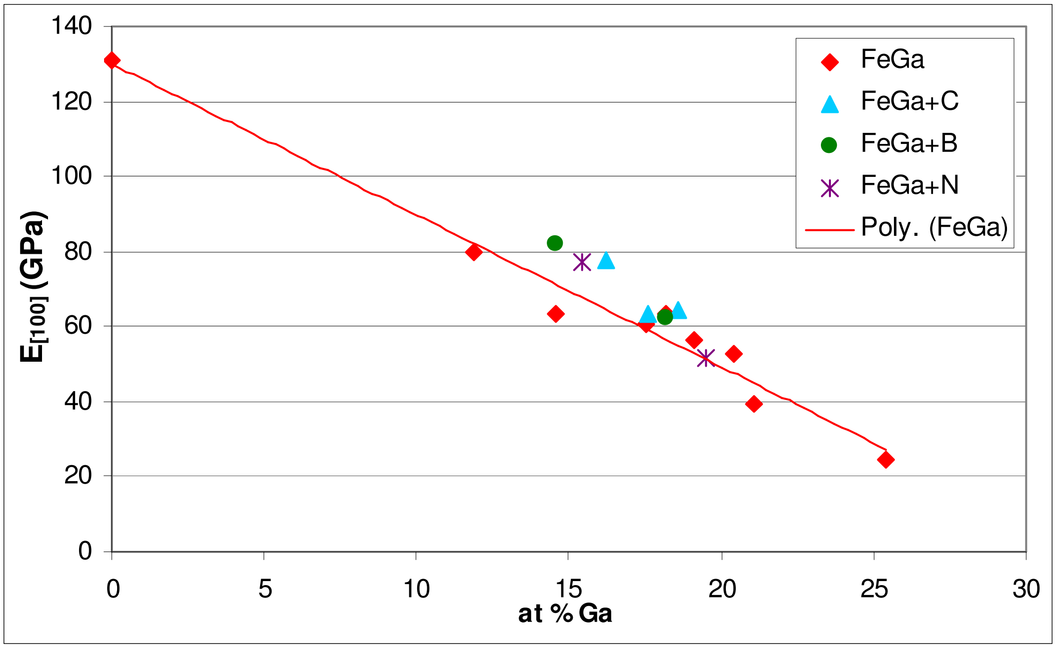

Figure 5.6: $E_{[100]}$ for binary FeGa, FeGa+C, FeGa+B and FeGa+N.

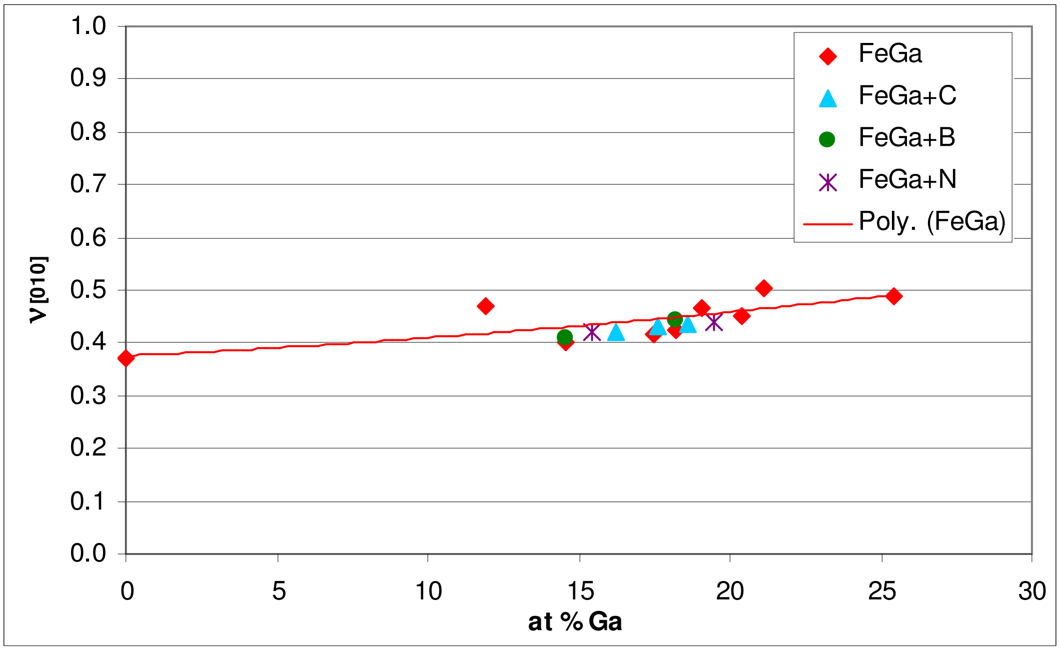

Figure 5.7: $\nu_{[010]}$ for binary FeGa, FeGa+C, FeGa+B and FeGa+N.

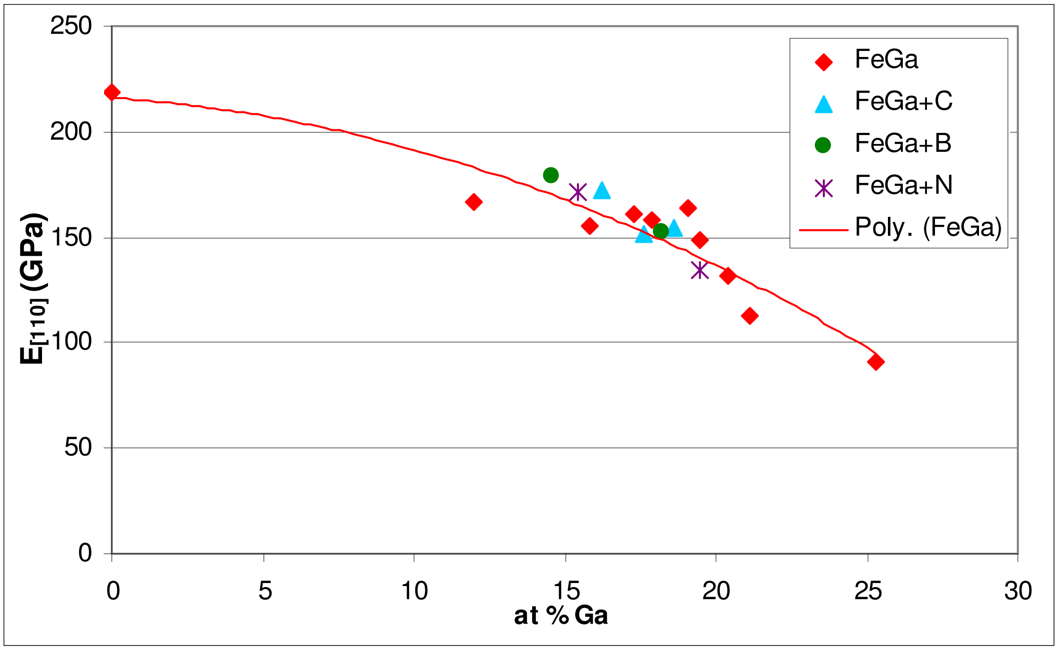

Figure 5.8: $E_{[110]}$ for binary FeGa, FeGa+C, FeGa+B and FeGa+N.

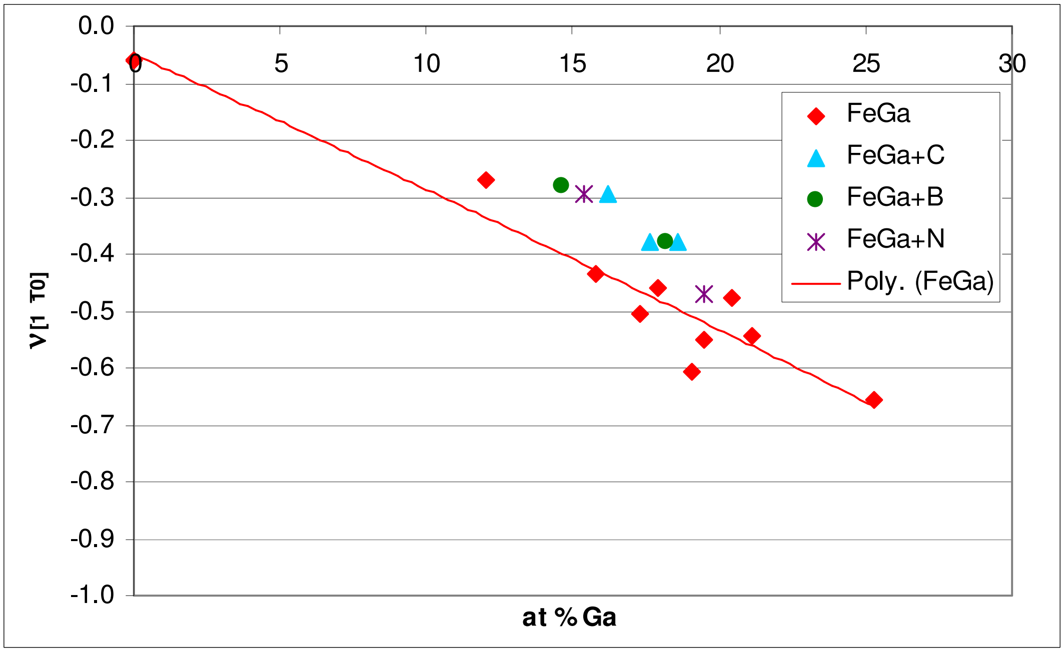

Figure 5.9: $\nu_{[1\ \bar{1}0]}$ for binary FeGa, FeGa+C, FeGa+B and FeGa+N.

5.4 Conclusions

The RUS analysis of Fe-Ga samples with small amounts of carbon, boron or nitrogen shows that these additions have a strong effect on the elastic behavior. Although none of the additions appeared to directly improve the auxetic behavior, it is still likely that one of these new alloys could be more useful for a specific application than a binary Fe-Ga alloy, especially since some have shown improved magnetostriction [34]. Future research on the development of applications can certainly benefit from this information about the elastic properties.

Chapter 6: Conclusions and Future Work

This chapter summarizes the major results and contributions of the work presented in this thesis. It concludes with suggestions for future research related to understanding and utilizing the mechanical behavior of Fe-Ga and Fe-Ga-X alloys.

6.1 Conclusions

The major contribution of this work was new information about the elastic behavior of Fe-Ga alloys. Through multiple experimental investigations, information was gained about the elastic stiffness constants and the engineering elastic properties for a variety of Fe-Ga based alloys. This information specifically helped further investigate the auxetic behavior of Galfenol.

From the tensile testing study, a method for measuring the engineering elastic properties of small single crystal samples was developed. Finite element analysis was used to verify the process and the equipment used in this study. In addition, a method for measuring the composition of Galfenol samples was implemented.

The main result of the tensile testing study however was a more complete database of the Young's moduli and Poisson's ratios. Samples ranging from 11.9% Ga to 25.4% Ga underwent tensile testing. The results of this showed that in general, the Young's modulus in both the [100] and [110] directions decreases linearly as the Ga content increases. The Poisson's ratio in the (100,010) direction increased towards 0.5 as the Ga content increased.

The auxetic behavior was also examined. In general, the Poisson's ratio in the (110, $1\bar{1}0$) direction became increasingly negative as the Ga content increased, with a minimum measured value of -0.66. Substantial auxetic behavior was observed for all the [110] oriented samples tested. The least negative value measured was for the 12.0% Ga sample, which had a value of $\nu_{[1\bar{1}0]}$ of -0.27. This is still much more auxetic than nearly all other metal alloys; certain iron-aluminum alloys being the only known exception [5,9].

The full set of results from the tensile testing was compared to additional, published values of the engineering elastic properties. These were experimentally obtained by multiple researchers [2,25,26]. This comparison allowed further examination of the trends in the different properties. These showed good agreement with the trends observed in the tensile testing data alone.

Resonant ultrasound spectroscopy (RUS) was also used to study the elastic behavior. For these tests, a method was implemented that enabled RUS analysis to be effectively performed on samples cut from tensile testing dogbone samples. After verifying the orientation and polishing and refinishing the samples, these samples were found to provide results with acceptably low error margins.

The RUS results showed that the shear modulus c' decreases as the Ga content increases, and the anisotropy parameter increases with Ga content. Since the anisotropy parameter is directly related to the extent of auxetic behavior, the results of the tensile testing suggested that the anisotropy parameter should behave this way. In addition, the RUS analysis showed that the individual elastic stiffness constants are dependent on the strength of the magnetic field applied, however c_{11} and c_{12} showed a higher degree of dependence than c', c_{44} or A.

In order to compare the two sets of elastic properties, a method was implemented for calculating the engineering elastic properties and their relative error values from the measured values of the elastic stiffness constants and their relative error values. This method was used to compare the elastic properties of three Galfenol samples that were studied using tensile testing and RUS. The analysis generally showed good agreement, with only two data points not matching within their error bars. The analysis also demonstrated that the engineering elastic properties could be calculated from RUS results and that each of the calculated values would have acceptably small error bars.

In addition to comparing the two sets of experimental data with each other, both sets were compared to a theoretical model developed by Zhang and Wu [16]. There were three compositions that were compared directly using results from the model and results from the tensile testing. The overall trends of the theoretical and experimental data sets were also examined. Good agreement was seen between the theory and both sets of experimental results.

RUS analysis was also performed on Fe-Ga samples that had small additions of a third element. Three samples with carbon were analyzed, two with nitrogen and two with boron. This analysis showed that these additions significantly affect the elastic behavior. The elastic stiffnesses were measured, and the engineering elastic properties were calculated. Both sets of information were compared to data for binary Fe-Ga alloys whose compositions most closely matched the compositions of the Fe-Ga-X samples.

It was observed that each of the additions inhibited the auxetic behavior. Although some of these additions have been shown to improve the magnetostriction of binary Fe-Ga alloys [34], the mechanism responsible for that improvement does not seem to be strongly related to the auxetic behavior. However, these alloys still show promise for a variety of applications.

6.2 Future Work

Galfenol has the potential to be utilized successfully in a variety of applications. In order to optimize the success of these applications however, there is still more information that is needed.

The first set of information that could be very useful is hardness measurements of various Galfenol and Galfenol-based alloys. It has been suggested that auxetic materials will be highly resistant to impacts [8]. Since Galfenol is generally harder than most other highly auxetic materials (i.e. foams and honeycomb structures), it is likely that it would show excellent impact resistance. In addition, Fe-Ga plus small amounts of carbon could also show promising results. Hardness testing would help to investigate these possibilities.

Another type of mechanical testing that would be beneficial is failure testing. The Galfenol samples tested in the tensile testing were always loaded elastically in order to preserve the sample for future testing. One composition has been tested to failure [25], however studying the plastic and failure behavior of additional compositions would be essential for any applications using Galfenol as a structural component.

It would also be interesting to measure the elastic stiffness constants under an applied compressive load. This cannot be done using RUS because RUS requires free boundary conditions on the sample, however it could be accomplished using an ultrasonic continuous wave method developed by Dai and Wuttig [37]. This would provide further information about how the elastic properties are related to the orientation of the internal magnetic moments.

It has been shown that the magnetostriction and phase composition of Galfenol are dependent on the heat treatment. In the region from around 18% to 21% Ga, samples that have been quenched show higher magnetostriction than samples that have been slow cooled [2]. This has been attributed to prevention of the formation of the $D0_3$ phase [11]. It would be interesting to see how heat treatment affects the elastic properties in that composition region. This would require two samples that have identical compositions and that were created from the same ingot, but one would be slow cooled and one would be quenched.

Similarly to Fe-Ga alloys, Fe-Al alloys also demonstrate both magnetostriction (up to 150 ppm [11]) and auxetic behavior (minimum of -0.45 [9]), however both are to a lesser degree than observed with Fe-Ga alloys. Their major benefit though is that they are less expensive than Fe-Ga alloys. Consequently, researchers have been studying Fe-Ga-Al alloys as a compromise [1,38]. Most of the research on these alloys however has been on quantifying the magnetostriction, not the elastic properties. It will be important to understand the elastic behavior of Fe-Ga-Al alloys before developing any applications.

Ideally, the culmination of studying the mechanical behavior of Galfenol will be a working device. Therefore, future researchers should work towards developing and building applications that utilize the auxetic behavior of Galfenol. A few possible applications were suggested in Chapter 1, however these are certainly not the only ways to take advantage of the unique mechanical behavior of Galfenol.

Appendix A: Stress-Strain Plots

This appendix contains stress-strain plots for each of the tensile specimens examined in this study. Since each tensile specimen was tested multiple times, multiple stress-strain plots were generated. Here however, only one stress-strain plot per sample is shown, representing the test that most closely matched the median elastic properties as reported in Chapter 2.

All the specimens were loaded elastically to around 150 MPa. The maximum stress for each sample varies because of differences in the dimensions of the cross-sections between the samples. In each plot, the black line represents the longitudinal strain and the green line represents the transverse strain. All of the [100] samples are plotted on the same scale to allow for comparison. The [110] samples are also all plotted on a consistent scale. The plots for the [100] samples are presented first, then the plots for the [110] samples.

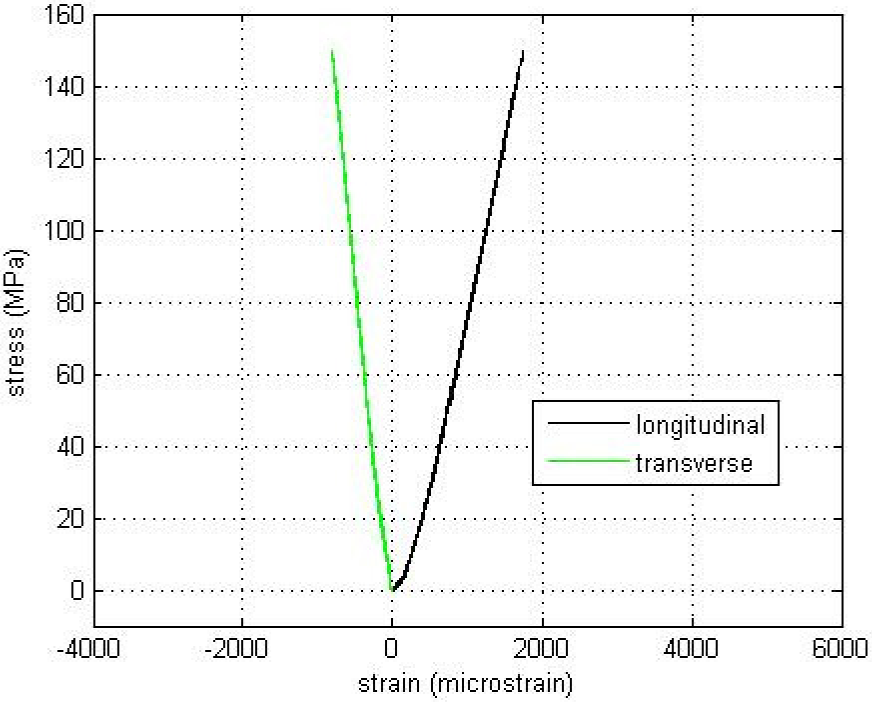

Figure A.1: Stress-strain plot for 11.9% [100] sample.

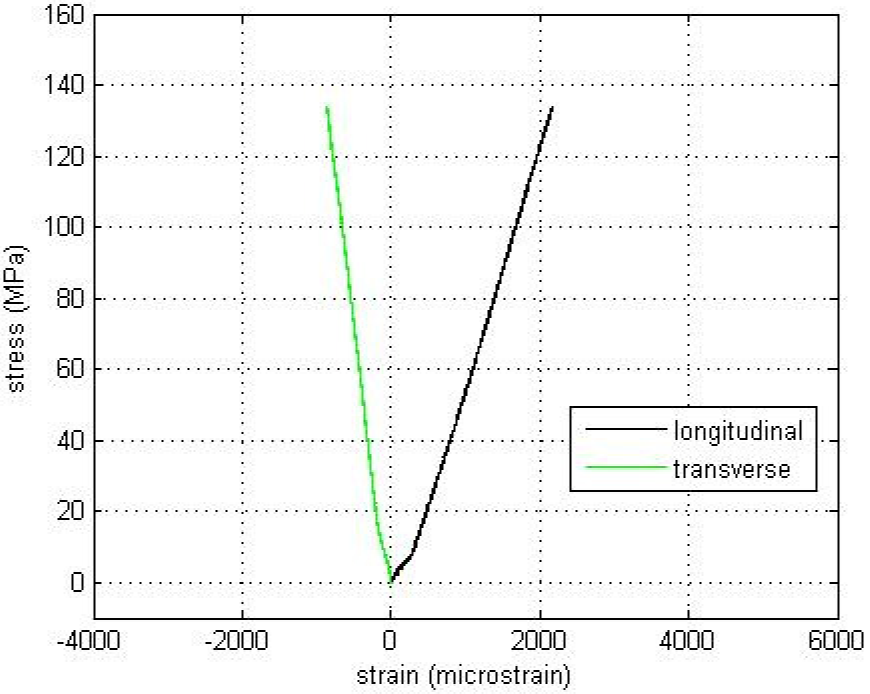

Figure A.2: Stress-strain plot for 14.6% [100] sample.

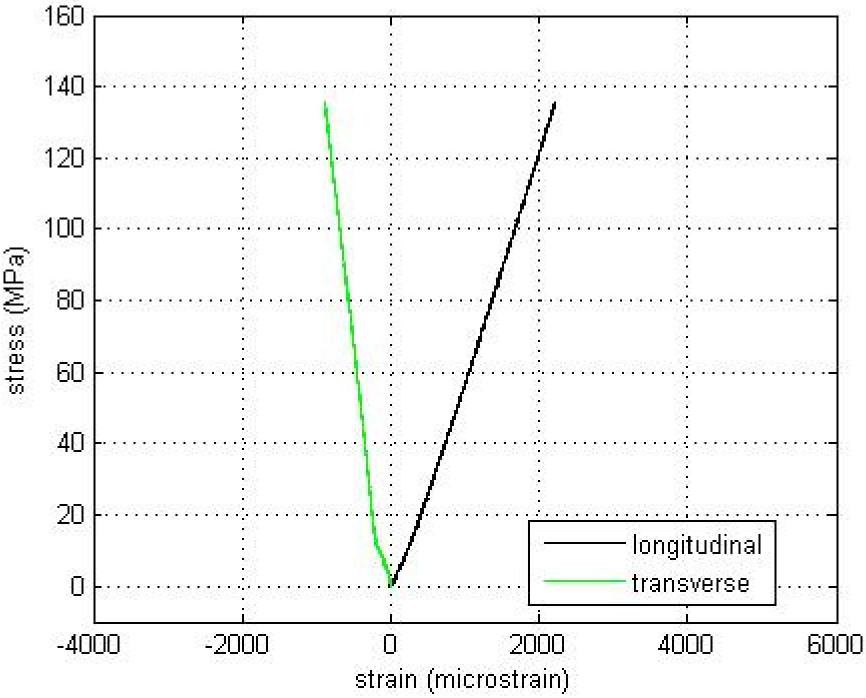

Figure A.3: Stress-strain plot for 17.5% [100] sample.

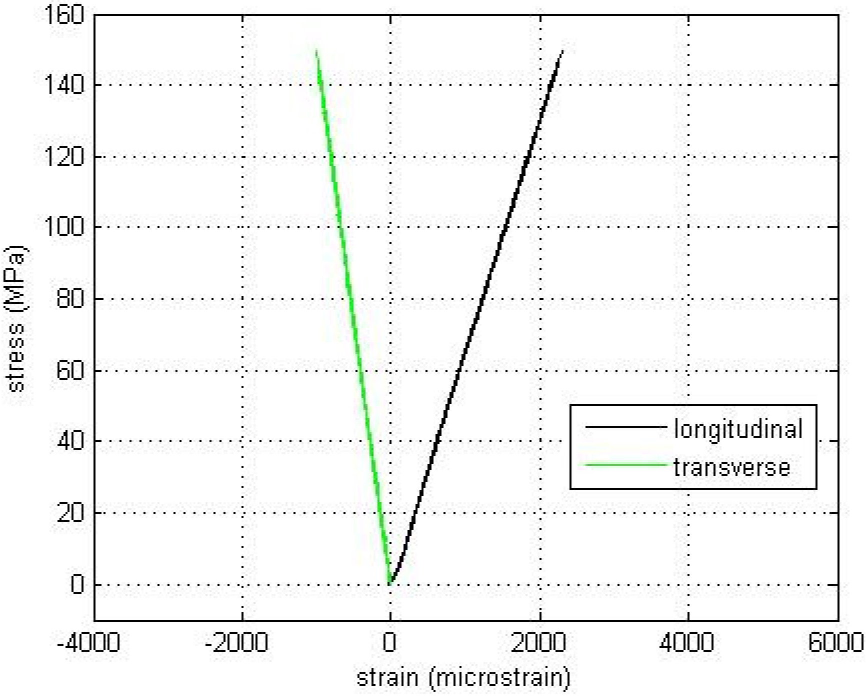

Figure A.4: Stress-strain plot for 18.2% [100] sample.

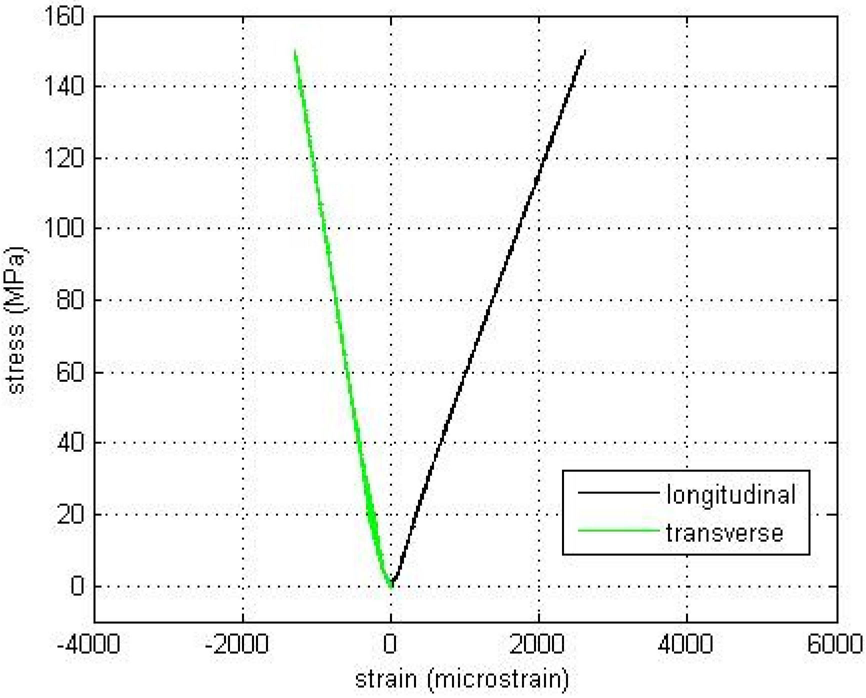

Figure A.5: Stress-strain plot for 19.1% [100] sample.

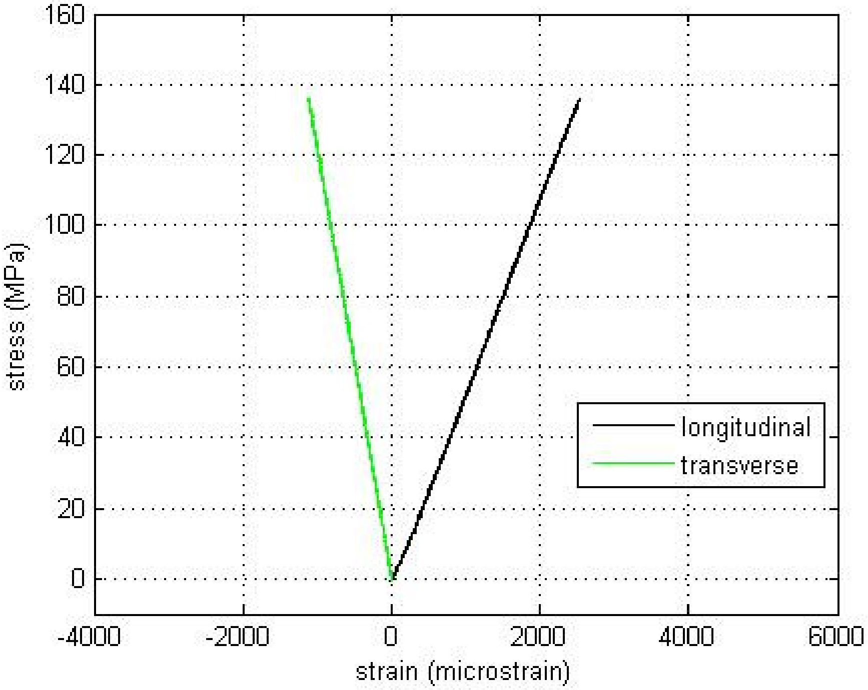

Figure A.6: Stress-strain plot for 20.4% [100] sample.

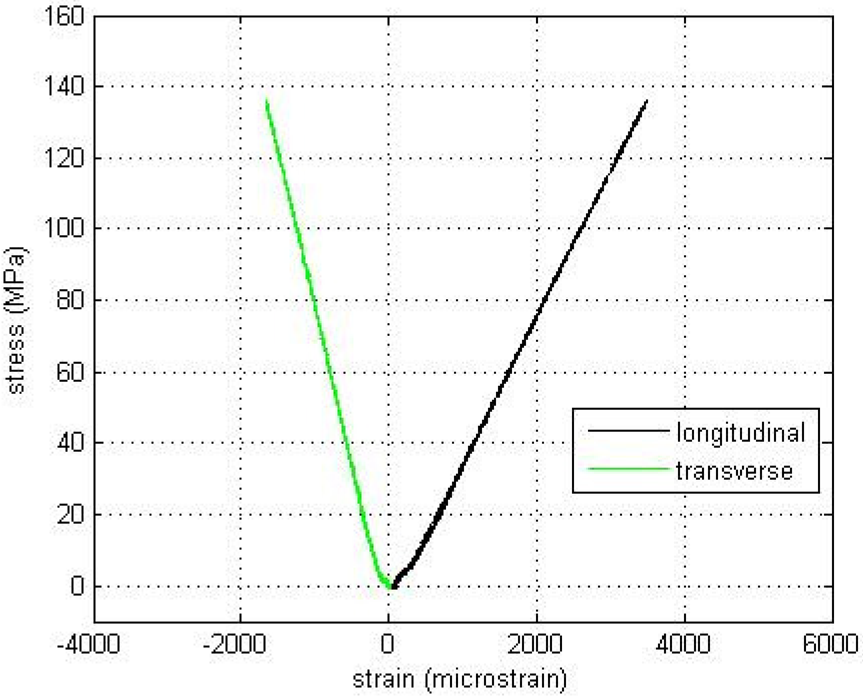

Figure A.7: Stress-strain plot for 21.1% [100] sample.

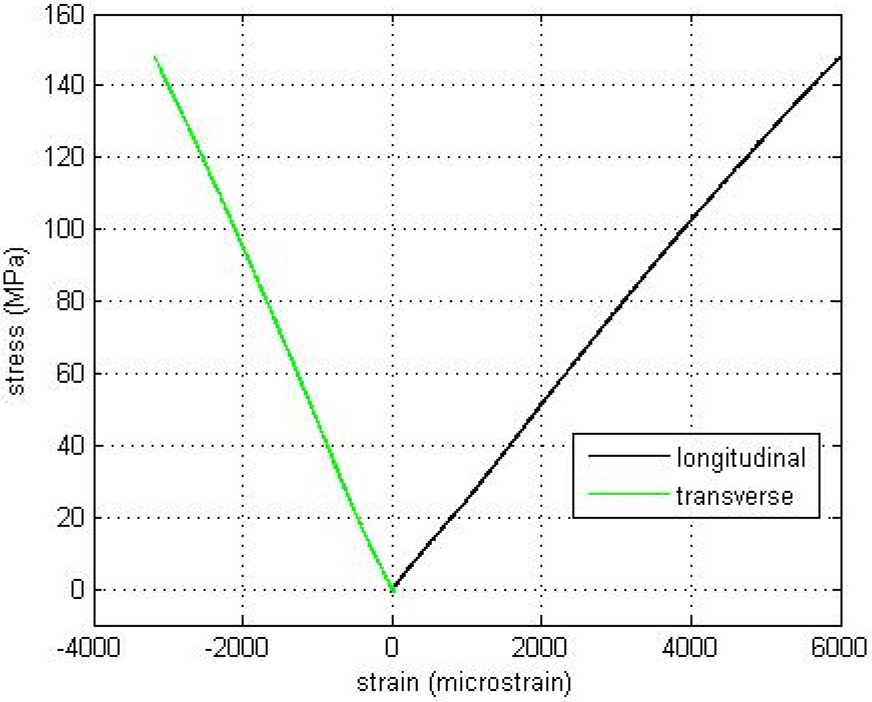

Figure A.8: Stress-strain plot for 25.4% [100] sample.

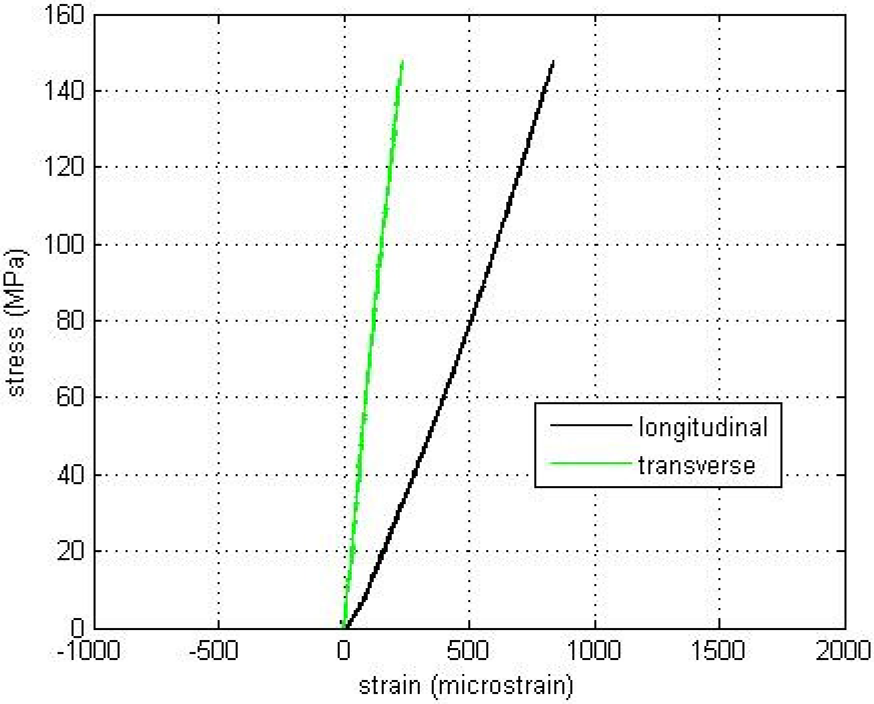

Figure A.9: Stress-strain plot for 12.0% [110] sample.

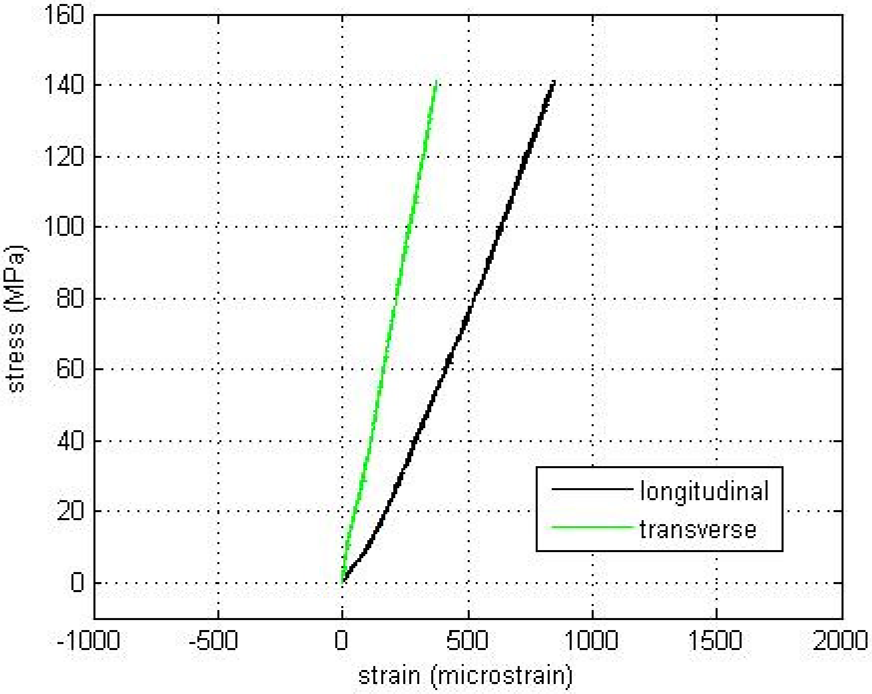

Figure A.10: Stress-strain plot for 15.8% [110] sample.

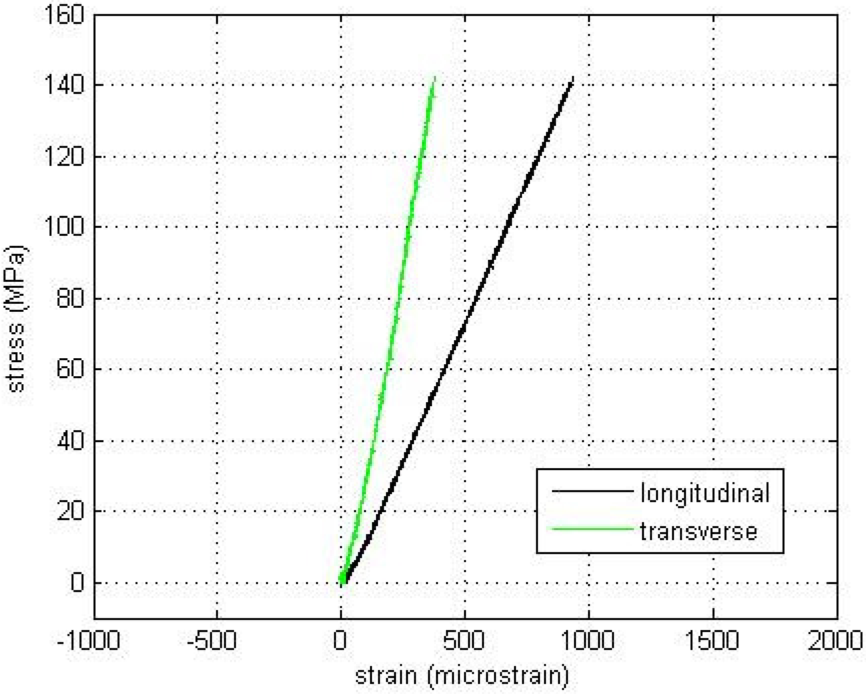

Figure A.11: Stress-strain plot for 17.3% [110] sample.

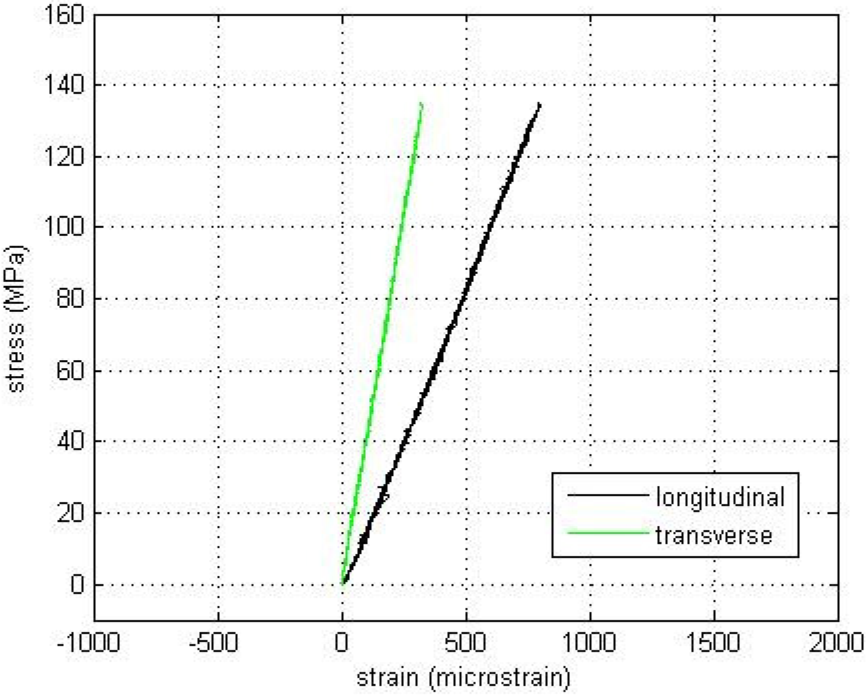

Figure A.12: Stress-strain plot for 17.9% [110] sample.

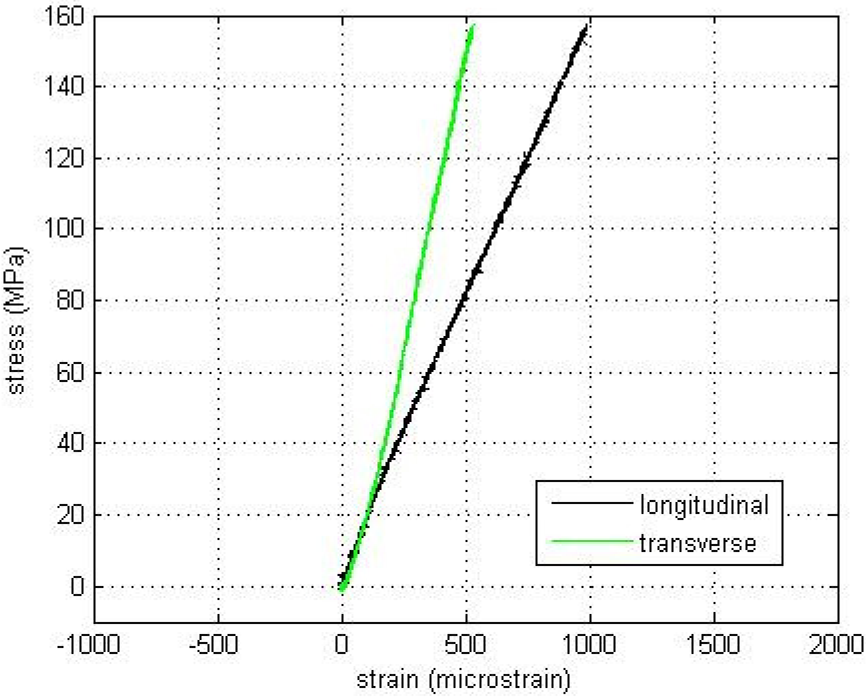

Figure A.13: Stress-strain plot for 19.1% [110] sample.

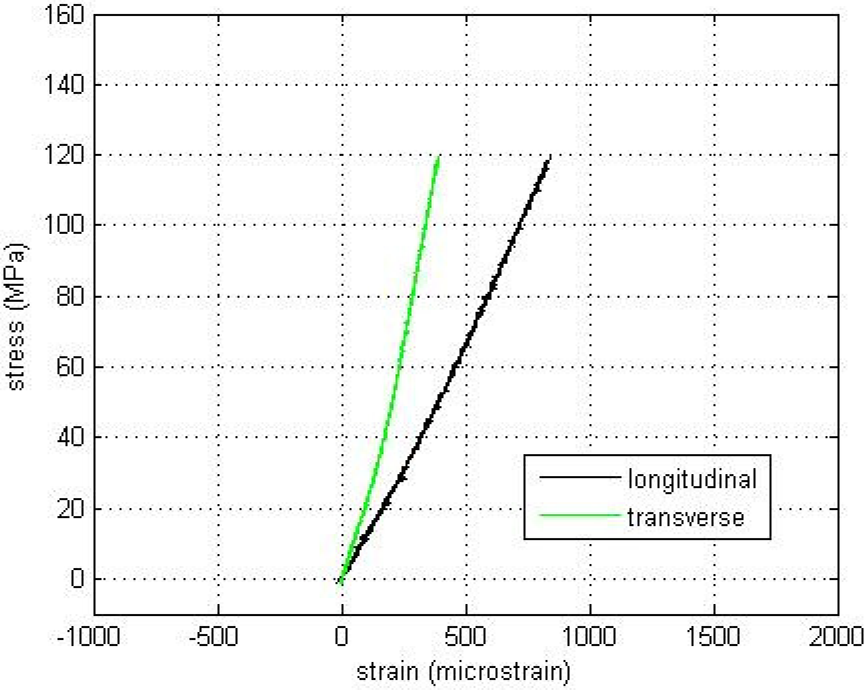

Figure A.14: Stress-strain plot for 19.5% [110] sample.

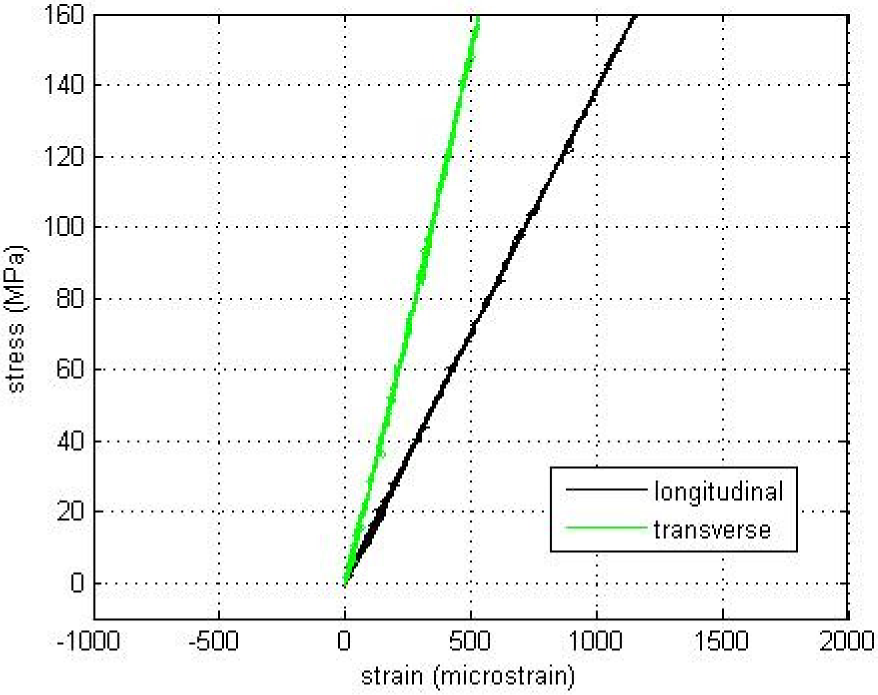

Figure A.15: Stress-strain plot for 20.4% [110] sample.

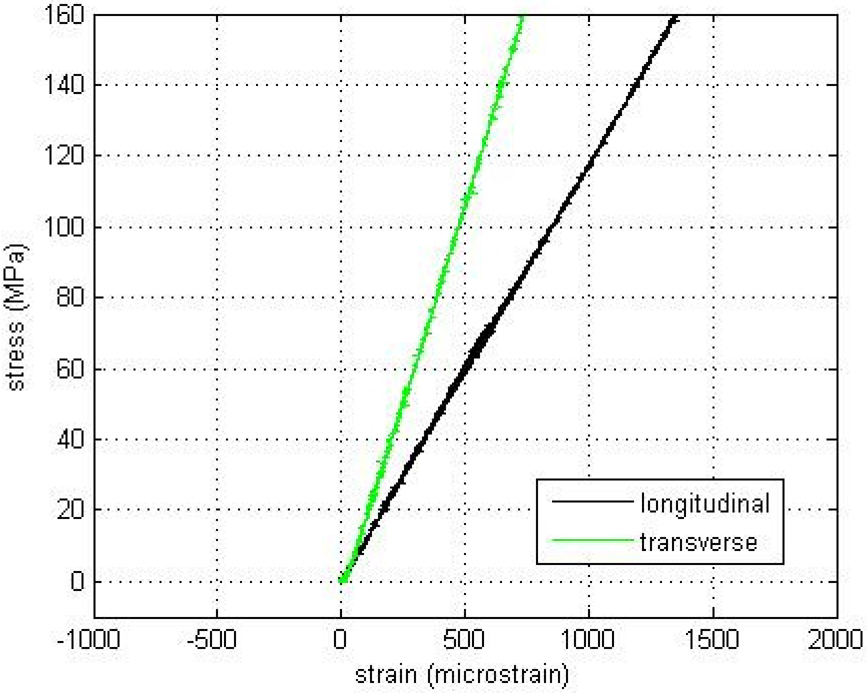

Figure A.16: Stress-strain plot for 21.1% [110] sample.

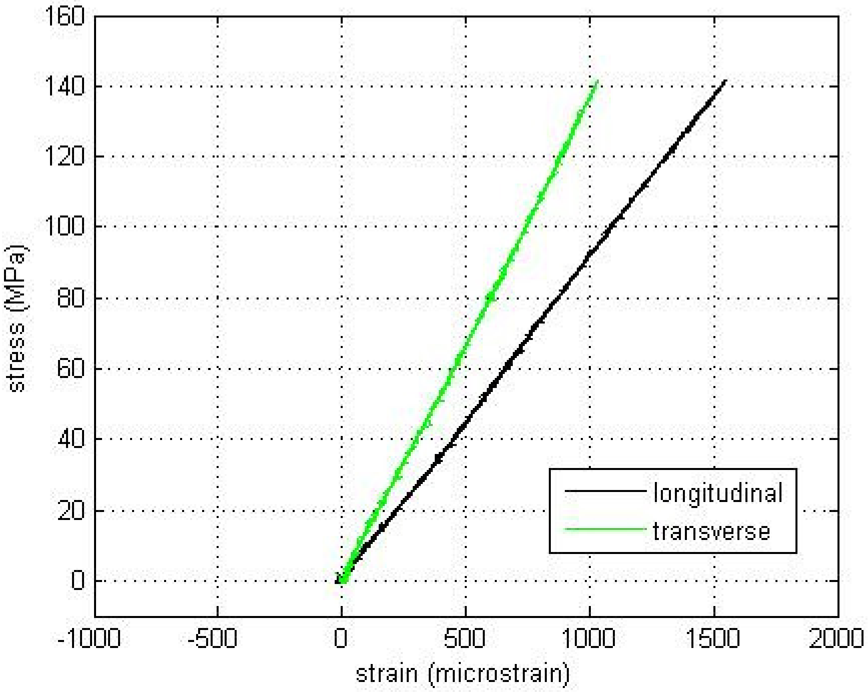

Figure A.17: Stress-strain plot for 25.4% [110] sample.

Appendix B: Resonance Frequencies of Fe-Ga

This appendix provides the measured resonance frequencies for the Fe-Ga samples studied using RUS in Chapter 3. This can be useful for a more thorough understanding of the fundamental properties of Galfenol. For each sample, the first 30 resonance frequencies are given. The resonance frequencies of each sample were measured multiple times, and the values provided here correspond to the set of frequencies that resulted in the lowest RMS error in the RUS algorithm.

Table B.1: Dimensions and masses of the Fe-Ga RUS samples.

Sample	Dimensions (mm)			Mass (g)
$Fe_{82.6}Ga_{17.4}$	3.1280	2.3650	1.4665	0.08553
$Fe_{79.6}Ga_{20.4}$	2.7280	2.0605	1.3375	0.05896
$Fe_{78.9}Ga_{21.1}$	2.7270	2.0700	1.3265	0.06100

Table B.2: Resonance frequencies of the Fe-Ga samples.

	$\mathbf{Fe_{82.6}Ga_{17.4}}$	$\mathbf{Fe_{79.6}Ga_{20.4}}$	$\mathbf{Fe_{78.9}Ga_{21.1}}$
Resonance	**Measured frequency (kHz)**		
1	321.6	333.8	299.9
2	391.0	397.0	363.1
3	438.7	440.8	398.7
4	497.5	558.2	505.7
5	551.0	570.6	514.2

6	554.7	573.4	516.8
7	566.0	578.0	575.9
8	635.7	634.3	582.8
9	668.1	707.9	662.1
10	713.5	725.0	665.0
11	727.9	753.7	699.7
12	802.3	802.5	732.5
13	817.6	884.9	828.7
14	827.5	894.4	833.6
15	910.2	907.3	854.0
16	927.0	928.9	862.2
17	935.0	944.6	879.7
18	937.7	963.1	881.4
19	956.0	966.0	897.9
20	964.9	980.4	913.7
21	972.5	994.7	923.2
22	1009.8	1000.5	941.8
23	1028.0	1063.7	971.3
24	1042.5	1102.8	1022.7
25	1046.3	1107.6	1025.1
26	1083.6	1116.5	1031.3
27	1099.9	1120.7	1039.0
28	1104.6	1132.1	1071.8

29	1117.9	1151.6	1104.6
30	1126.4	1173.8	1113.9

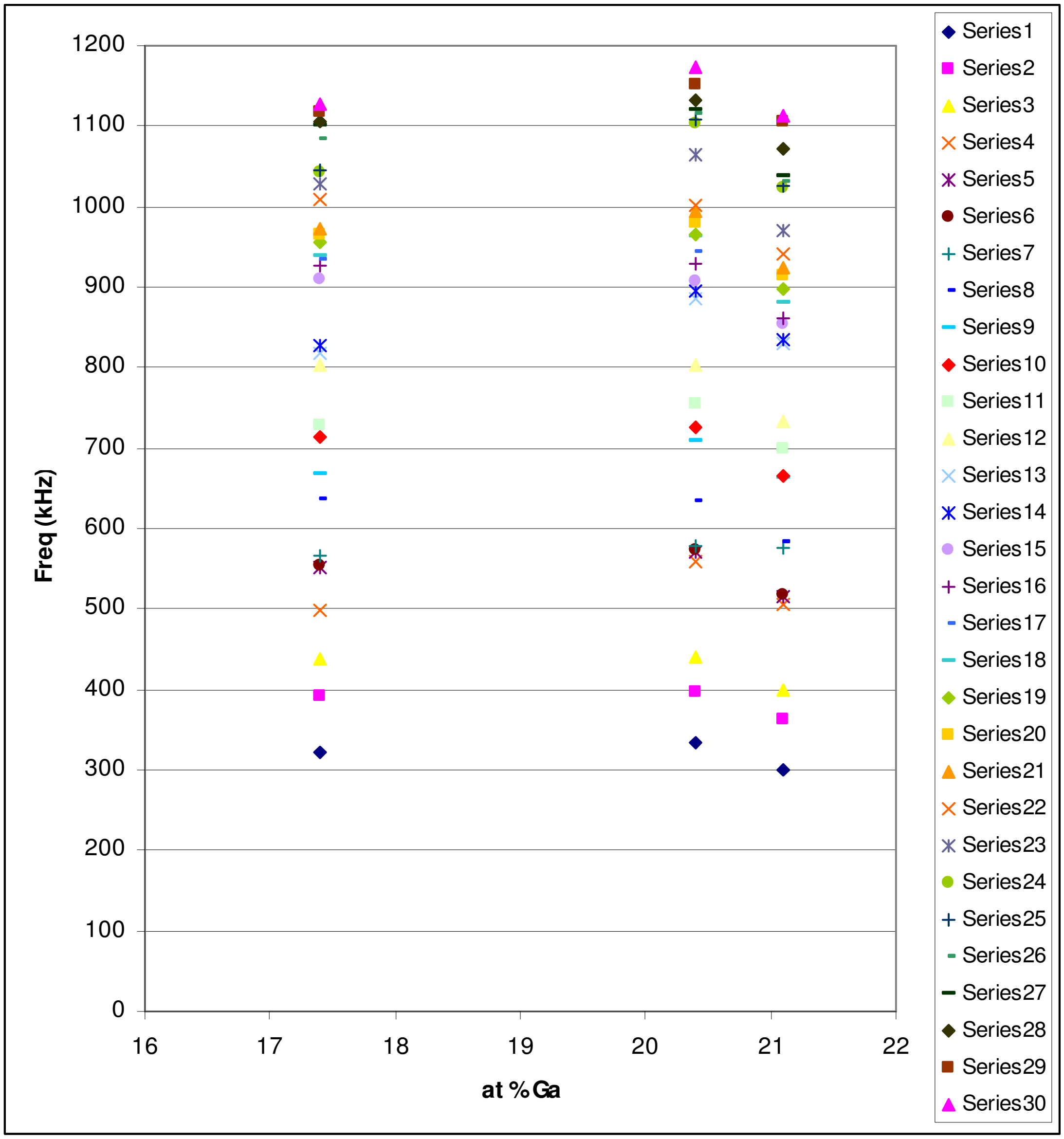

Figure B.1: Resonance frequencies of the Fe-Ga samples.

Appendix C: Resonance Frequencies of Fe-Ga-X

This appendix provides the measured resonance frequencies for the Fe-Ga-X samples studied using RUS in Chapter 5. This can be useful for a more thorough understanding of the fundamental properties of iron-gallium based alloys. For each sample, the first 30 resonance frequencies are given. The resonance frequencies of each sample were measured multiple times, and the values provided here correspond to the set of frequencies that resulted in the lowest RMS error in the RUS algorithm.

Table C.1: Dimensions and masses of the Fe-Ga-X RUS samples.

Sample	**Dimensions (mm)**			**Mass (g)**
$Fe_{83.72}\ Ga_{16.2}\ C_{0.08}$	3.0900	2.6545	1.5375	0.09695
$Fe_{82.33}\ Ga_{17.6}\ C_{0.07}$	3.2770	2.2665	1.9215	0.11200
$Fe_{81.23}\ Ga_{18.6}\ C_{0.17}$	3.0665	2.1260	1.6230	0.08185
$Fe_{85.38}\ Ga_{14.6}\ B_{0.02}$	2.6375	1.7805	1.2535	0.04580
$Fe_{81.72}\ Ga_{18.2}\ B_{0.08}$	2.7920	1.9620	1.3615	0.05840
$Fe_{84.59}\ Ga_{15.4}\ N_{0.01}$	2.7985	2.0630	0.9975	0.04490
$Fe_{80.49}\ Ga_{19.5}\ N_{0.01}$	2.6970	2.4240	1.7590	0.08965

Table C.2: Resonance frequencies of the Fe-Ga-C samples.

	$Fe_{83.72}Ga_{16.2}C_{0.08}$	**$Fe_{82.33}Ga_{17.6}C_{0.07}$**	**$Fe_{81.23}Ga_{18.6}C_{0.17}$**
Resonance	**Measured Frequency (kHz)**		
1	349.6	327.7	338.0
2	444.8	348.3	377.9
3	460.7	403.5	436.9
4	488.4	518.9	560.1
5	514.0	528.4	581.3
6	532.6	550.5	603.2
7	553.3	566.1	627.8
8	625.8	590.7	638.5
9	696.6	633.6	683.2
10	754.9	650.5	711.5
11	761.3	654.0	717.8
12	771.9	668.5	760.5
13	856.7	715.9	850.4
14	865.8	731.8	863.7
15	883.4	742.0	868.0
16	893.6	801.4	880.8
17	924.9	803.3	888.6
18	935.0	808.5	935.0
19	940.7	835.8	945.2
20	968.5	838.7	946.6

21	978.7	879.6	973.1
22	992.2	908.7	1035.4
23	1006.5	952.4	1038.9
24	1038.9	955.2	1071.5
25	1055.9	985.1	1075.3
26	1112.2	989.1	1083.3
27	1141.5	994.2	1086.8
28	1150.6	997.0	1104.0
29	1154.8	1013.8	1104.2
30	1170.9	1062.2	1149.1

Table C.3: Resonance frequencies of the Fe-Ga-B samples.

	$\mathbf{Fe_{85.38}Ga_{14.6}B_{0.02}}$	$\mathbf{Fe_{81.72}Ga_{18.2}B_{0.08}}$
Resonance	**Measured Frequency (kHz)**	
1	418.5	351.5
2	489.0	410.3
3	577.2	469.3
4	636.3	593.3
5	787.5	621.5
6	802.4	641.7
7	815.1	652.7
8	856.2	694.8
9	882.0	734.2

10	918.9	768.6
11	936.2	782.4
12	1055.3	845.5
13	1071.6	931.6
14	1083.9	955.3
15	1202.0	969.0
16	1204.8	977.9
17	1216.7	1001.4
18	1248.2	1035.3
19	1273.7	1043.9
20	1295.0	1053.5
21	1307.9	1063.7
22	1309.3	1104.5
23	1358.9	1151.7
24	1369.9	1164.8
25	1386.2	1169.9
26	1391.1	1173.6
27	1410.1	1201.6
28	1425.3	1202.8
29	1438.8	1210.6
30	1514.5	1225.0

Table C.4: Resonance frequencies of the Fe-Ga-N samples.

	$\mathbf{Fe_{84.59}Ga_{15.4}N_{0.01}}$	$\mathbf{Fe_{80.49}Ga_{19.5}N_{0.01}}$
Resonance	**Measured Frequency (kHz)**	
1	327.6	353.4
2	463.5	405.6
3	499.9	413.4
4	524.8	462.9
5	590.5	473.4
6	683.9	512.5
7	699.6	517.5
8	733.0	603.0
9	810.9	681.7
10	856.9	698.4
11	863.8	703.4
12	873.4	704.5
13	912.3	715.7
14	1081.4	718.8
15	1098.9	728.3
16	1141.8	766.4
17	1153.1	805.8
18	1177.4	827.5
19	1191.6	833.1
20	1239.9	835.1

21	1262.2	866.4
22	1297.2	876.2
23	1325.6	889.8
24	1356.8	947.5
25	1366.0	964.0
26	1371.4	981.9
27	1382.0	1001.3
28	1427.3	1056.9
29		1075.4
30		1094.1

For the $Fe_{84.59}Ga_{15.4}N_{0.01}$ sample, only the first 28 resonance frequencies were measured because the 29th through 32nd frequencies were so close together they were indistinguishable.

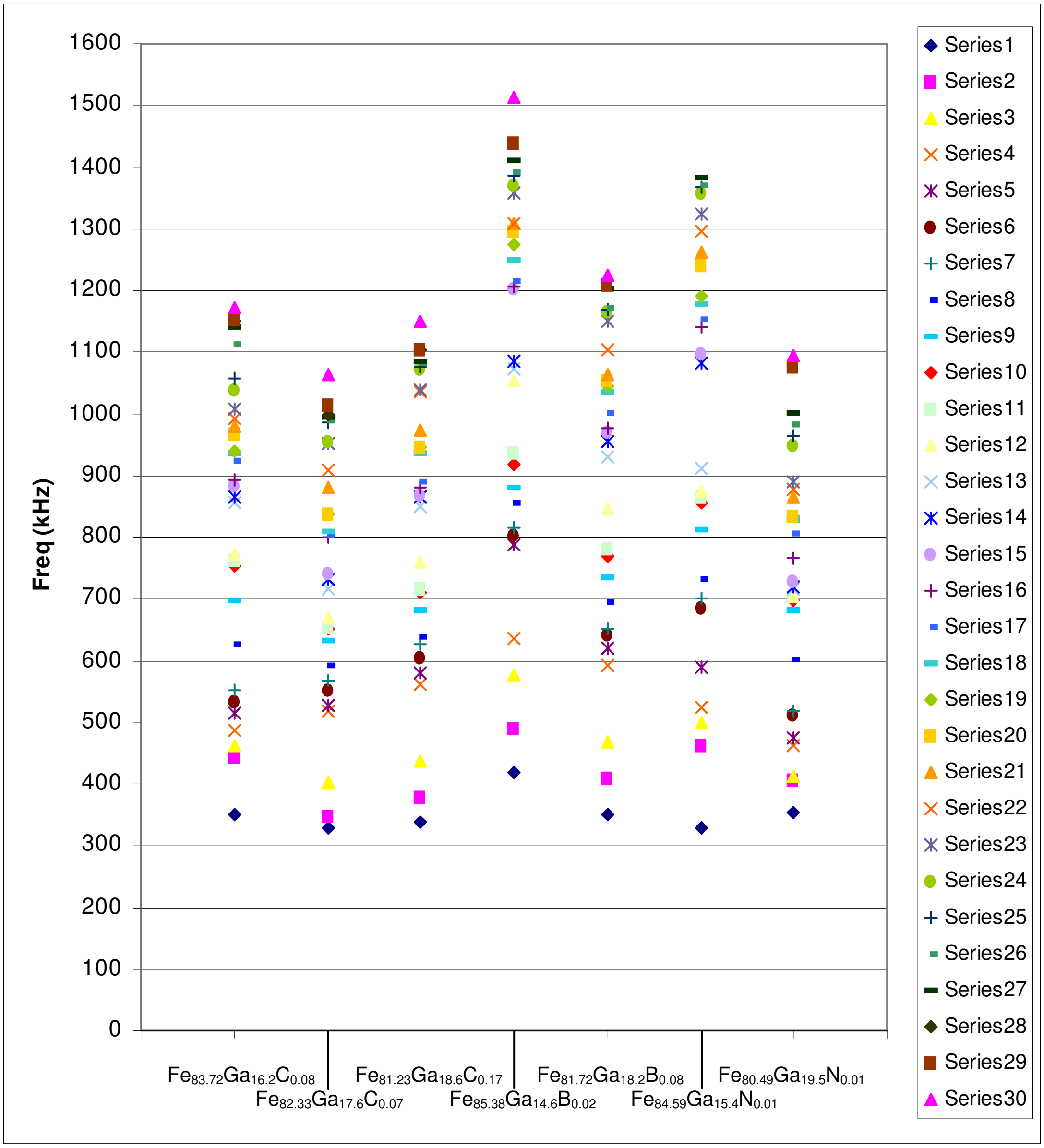

Figure C.1: Resonance frequencies of the Fe-Ga-X samples.

Bibliography

[1] Clark, A.E., Restorff, J.B., Wun-Fogle, M., Lograsso, T.A. and Schlagel, D.L., 2000, "Magnetostrictive Properties of Body-Centered Fe-Ga and Fe-Ga-Al Alloys," IEEE Transactions on Magnetics, 36(5), pp. 3238-3240.

[2] Clark, A.E., Hathaway, K.B., Wun-Fogle, M., Restorff, J.B., Lograsso, T.A., Keppens, V.M., Petculescu, G., and Taylor, R.A., 2003, "Extraordinary Magnetoelasticity and Lattice Softening in BCC Fe-Ga Alloys," Journal of Applied Physics, 93(10), pp. 8621-8623.

[3] Petculescu, G., Hathaway, K.B., Lograsso, T.A., Wun-Fogle, M., and Clark, A.E., 2005, "Magnetic Field Dependence of Galfenol Elastic Properties," Journal of Applied Physics, 97(10), pp. 10M315.

[4] Callister, W.D., 2005, Fundamentals of Materials Science and Engineering, John Wiley & Sons, Inc., Hoboken, NJ.

[5] Jain, M. and Verma, M. P., 1990, "Poisson's Ratios in Cubic Crystals Corresponding to (110) Loading," Indian Journal of Pure & Applied Physics, 28(4), pp. 178-182.

[6] Ting, T.C.T, and Chen, T., 2005, "Poisson's Ratio for Anisotropic Elastic Materials Can Have No Bounds," Quarterly Journal of Mechanics and Applied Mathematics, 58(1), pp. 73-82.

[7] Baughman, R. H., Shacklette, J. M., Zakhidov, A. A., and Stafstrom, S., 1998, "Negative Poisson's Ratios as a Common Feature of Cubic Metals," Nature, 392, pp. 362-365.

[8] Evans, K. E. and Alderson, A., 2000, "Auxetic Materials: Functional Materials and Structures from Lateral Thinking!", Advanced Materials, 12(9), pp. 617-628.

[9] Kellogg, R. A., 2003, Development and Modeling of Iron-Gallium Alloys, Ph.D. thesis, Iowa State University, Ames, Iowa.

[10] Atulasimha, J., 2006, Characterization and Modeling of the Magnetomechanical Behavior of Iron-Gallium alloys, Ph.D. thesis, University of Maryland, College Park, Maryland.

[11] Cullen, J.R., Clark, A.E., Wun-Fogle, M., Restorff, J.B., and Lograsso, T.A., 2001, "Magnetoelasticity of Fe-Ga and Fe-Al alloys," Journal of Magnetism and Magnetic Materials, 226-230(Part 1), pp. 948-949.

---

[12] Clark, A.E., “Structural Fe-based Alloys with High Magnetostriction”, Galfenol Workshop, January 29, 2004, University of Maryland, College Park, Maryland.

[13] Ikeda, O., Kainuma, R., Ohnuma, I., Fukamichi, K., and Ishida, K., 2002, “Phase Equilibria and Stability of Ordered b.c.c. Phases in the Fe-rich Portion of the Fe-Ga System,” Journal of Alloys and Compounds, 347(1-2), pp. 198-205.

[14]Meyers, A.M., Armstrong, R.W., and Kirchner, H.O., 1999, Mechanics and Materials: Fundamentals and Linkages, John Wiley & Sons, New York, pp. 76-77.

[15] Courtney, T.H., 2000, Mechanical Behavior of Materials, McGraw-Hill, Boston, pg. 59.

[16] Schurter, H.M., Zhang, Y., Wu, R., and Flatau, A.B., 2009, “Mechanical Behavior and Auxetic Properties of Galfenol,” Proceedings of SPIE 7289-68.

[17] Kresse G. and Furthmüller, J., 1996, “Efficiency of Ab-Initio Total Energy Calculations for Metals and Semiconductors Using a Plane-Wave Basis Set,” Computational Materials Science, 6(1), pp.15-50.

[18] Kresse, G. and Furthmüller, 1996, “Efficient Iterative Schemes for Ab Initio Total-Energy Calculations Using a Plane-Wave Basis Set,” Physical Review B, 54(16), pp. 11169-11186.

[19] Wang, S.Q. and Ye, H.Q., 2003, “Ab Initio Elastic Constants for the Lonsdaleite Phases of C, Si and Ge,” Journal of Physics - Condensed Matter, 15(30), pp. 5307-5314.

[20] Chen, K. and Cheng, L.M, 2007, “Ab Initio Study of Elastic, Thermal Physical Properties and Electronic Structure of Fe-Ga alloys,” Physica Status Solidi B, 244(10), pp. 3583-3592.

[21] Huntington, H. B., 1958, The Elastic Constants of Crystals, Academic Press, New York & London, pp. 93-98.

[22] Atulasimha, J., Flatau, A. B., and Kellogg, R. A., 2006, “Sensing Behavior of Varied Stoichiometry Single Crystal Fe-Ga,” Journal of Intelligent Material Systems and Structures, 17(2), pp. 97-105.

[23] McLean, K. O. and Smith, C.S., 1972, “Ultrasonic Parameters in Born Model of Lithium Halides”, Journal of Physics and Chemistry of Solids, 33(2), 279.

[24] Dally, J. W. and Bonenberger, R. J., 2003, Design Analysis of Structural Elements, College House Enterprises, LLC, Knoxville, TN, pg. 686.

[25] Kellogg, R.A., Russell, A.M., Lograsso, T.A., Flatau, A.B.,Clark, A.E., and Wun-Fogle, M., 2004, “Tensile Properties of Magnetostrictive Iron-Gallium Alloys,” Acta Materialia, 52(2004), pp. 5043-5050.

[26] Yoo, J. H., and Flatau, A. B., 2004, “Measured Iron-Gallium Alloy Tensile Properties Under Magnetic Fields,” Proc. SPIE 5387, pp. 476-486.

[27] Migliori, A., and Sarrao, J.L., 1997, Resonant Ultrasound Spectroscopy: Applications to Physics, Materials Measurements, and Nondestructive Evaluation, John Wiley & Sons, New York.

[28] Joseph, R.I., and Schlomann, E., 1965, “Demagnetizing Field in Nonellipsoidal Bodies,” Journal of Applied Physics, 36(5), pp. 1579-1593.

[29] Devore, J.L., 2008, Probability and Statistics for Engineering and the Sciences, 7th ed., Thomson Higher Education, Belmont, CA.

[30] Haslach Jr., H.W., and Armstrong, R.W., 2004, Deformable Bodies and their Material Behavior, John Wiley & Sons, Hoboken NJ.

[31] Dieter, G.E., 1976, Mechanical Metallurgy, McGraw-Hill, Boston, pg. 63.

[32] Datta, S., Huang, M., Raim, J., Lograsso, T.A., and Flatau, A.B., 2006, “Effect of Thermal History and Gallium Content on Magneto-Mechanical Properties of Iron Gallium Alloys,” Materials Science and Engineering A, 435-436, pp. 221-227.

[33] Sears, F.W., and Zemansky, M.W., 1952, College Physics, Addison-Wesley, Cambridge MA, pg. 281.

[34] Huang, M., Lograsso, T.A., Clark, A.E., Restorff, J.B., and Wun-Fogle, M., 2008, “Effect of Interstitial Additions on Magnetostriction in Fe-Ga Alloys,” Journal of Applied Physics, 103(07B314).

[35] Clark, A.E., Restorff, J.B., Wun-Fogle, M., Hathaway, K.B., Lograsso, T.A., Huang, M., and Summers, E., 2007, “Magnetostriction of Ternary Fe-Ga-X (X=C, V, Cr, Mn, Co, Rh) Alloys,” Journal of Applied Physics, 101 (09C507).

[36] Summers, E.M., Lograsso, T.A., and Wun-Fogle, M., 2007, “Magnetostriction of Binary and Ternary Fe-Ga alloys.” Journal of Materials Science, 42(23), pp. 9582-9594.

[37] Dai, L., 2004, “Elasticity in Ferromagnetic Shape Memory Alloys,” Ph.D. thesis, University of Maryland, College Park, MD.

---

[38] Mungsantisuk, P., Corson, R.P., and Guruswamy, S., 2005, “Influence of Be and Al on the Magnetostrictive Behavior of FeGa Alloys,” Journal of Applied Physics, 98(12).